A 3D full Stokes calving model for Store Glacier, West Greenland

Joseph Alan Todd

Jesus College

This dissertation is submitted on 24 Aug, 2016 for the degree of Doctor of Philosophy

Abstract

Iceberg calving is the mechanism whereby blocks of ice of various sizes break off the front of glacier terminating in water. The mechanism comprises processes of fracture which occur across a wide range of spatial and temporal scales. The diverse nature of calving, which is principally controlled by ice flow dynamics but also strongly influenced by links to external forcing by climate, makes it challenging to incorporate into models of glaciers and ice sheets. Consequently, calving of icebergs from the Greenland and Antarctic ice sheets represents one of the most significant uncertainties in predictions of future sea levels.

Two processes hypothesised to significantly influence calving are 1) the destabilisation of the calving ice front by undercutting caused by submarine melting and 2) the support of the front from a proglacial mélange consisting of calved icebergs and sea ice. The former process is expected to be particularly significant in summer, when melting of the calving ice front is accelerated by convective plumes of freshwater discharged subglacially into the salty fjord environment. The second process only occurs in winter when sea ice and icebergs form a rigid proglacial mélange in front of calving glaciers. With global warming amplified in the Arctic and causing longer and hotter summers as well as shorter and warmer winters, it has become essential to understand how calving glaciers respond to changes in both of these processes.

This study provides new theoretical understanding of calving through the development of a state-of-the art numerical calving model. The model is developed, tested and applied to Store Glacier, in 2D as well as 3D, and it solves the full-Stokes equations of ice flow using the Elmer/Ice finite element package. Store Glacier is the second largest outlet glacier in West Greenland in terms of flux, discharging 13.9 km^3 of ice into Uummannaq Fjord annually. The rate of iceberg calving has a strong seasonal trend, which makes the glacier an ideal case study for an investigation into the seasonally varying processes of iceberg calving and the external link to climate. The hypothesis that underpins this research is that a model capable of reproducing observed seasonal variations is also a model capable of reliably predicting decadal and longer change.

The calving model implements the crevasse depth criterion, which states that calving occurs when surface and basal crevasses penetrate the full thickness of the glacier. The model is forced with variable rates of submarine melting and ice mélange buttressing, to determine which of these processes influences the glacier the most. Sensitivity to changes in these frontal processes was investigated by forcing the model with a) increased submarine melt rates acting over longer periods of time and b) decreased mélange buttressing force acting over a reduced period.

The model outputs show that ice mélange is the primary driver of the observed seasonal advance of the terminus and the associated seasonal variation in calving rate. The 3D model also demonstrates a significant, albeit secondary, influence from submarine melting on calving rate, though the 2D model did not, suggesting that 1D and 2D flowline solutions may be unsuitable for modelling iceberg calving from glaciers with complex 3D geometry. The outputs also highlight the importance of topographic setting; Store Glacier terminates on a large bedrock sill, and this was found to exert a first-order control on calving rate, explaining Store Glacier's comparative stability during a period when many Greenland outlet glaciers underwent concurrent retreat. The sensitivity analysis shows that a total loss of ice mélange buttressing or a doubling of submarine melt rate could destabilise the current terminus position sufficiently to trigger sustained retreat across the deep trough which extends 30km from Store's current terminus position, causing ice flow acceleration and faster sea level rise.

Declaration

This dissertation is my own work and contains nothing which is the outcome of work done in collaboration with others, except where specified in the text. It is not substantially the same as any that I have submitted, or, is being concurrently submitted for a degree or diploma or other qualification at the University of Cambridge or any other University or similar institution except as declared in the Preface and specified in the text. I further state that no substantial part of my dissertation has already been submitted, or, is being concurrently submitted for any such degree, diploma or other qualification at the University of Cambridge or any other University of similar institution except as declared in the Preface and specified in the text. This dissertation does not exceed the prescribed limit of 275 pages.

Joseph Alan Todd
Aug, 2016

Acknowledgements

Over the course of the past 4 years, I have often had the almost physical sensation of having bitten off more than I could chew. But now, rather than lying asphyxiated on the floor, I find myself at the end, and I know that if it wasn't for the immense support of colleagues, friends and family, I would surely have choked. This project was not a lone undertaking, and I feel extremely lucky to be surrounded with the great minds and great friends who saw me to the light at the end of the tunnel.

First and foremost, I am extremely grateful to my supervisor, Poul Christoffersen, whose insight, guidance and encouragement made this project possible. In his position, I doubt I would have given myself this opportunity, so I am indebted to him for his support.

The glaciological model Elmer/Ice which forms the backbone of this study is a great, complex beast and a testament to the power of collaboration. I am grateful to Martin O'Leary for nudging me towards it five years ago, and Carlos Martin for sitting down with me and taking me through the basics. To Thomas Zwinger, I owe an unrepayable (sorry) debt of gratitude for his expertise, patience, and his generosity with his time; without his assistance, I would have given up on modelling almost immediately. Thanks are also due to Peter Råback for help with remeshing, to Olivier Gagliardini for pointing out the obviously easier path to 3D calving, and Fabien Gillet-Chaulet for useful discussions on inverse methods.

Working at the Scott Polar Research Institute has been a fantastic experience which brought me into contact with a great group of colleagues and friends. I owe a great deal of thanks to all the SPRI staff who make it such a great place to work. I am grateful to Craig Stewart for useful and occasionally heated discussions about stress, Mohr's *sphere* and basal crevassing. Thanks also to Nick Toberg for interesting chats about ice mélange and SfM software, and to Conrad Koziol for forcing me to confront the more fundamental mathematical aspects of

my work. To TJ Young, I am grateful for impromptu Mandarin lessons, excellent Asian cuisine, road trips, punting trips and pub trips.

The data which constrained the basal conditions of the 3D model, and which allowed us to compare our results to reality were kindly provided by Adrian Luckman, to whom I am very much obliged. Thanks to Donald Slater and Tom Cowton for informative discussions and useful MATLAB scripts relating to plume theory, and to the developers of Paraview and GMSH, among the most powerful tools I have had the pleasure to use.

I was lucky enough to escape the curse of the modeller and undertake two excellent field seasons in Uummannaq. For that opportunity, and for consistently heated arguments about basal crevasses and the philosophy of science, I am very grateful to Alun Hubbard. Thanks also to Johnny Ryan for letting me fly the drone, for being such a dab hand with balsa wood and glue, and for the most memorable day of DIY aeronautical engineering I've ever experienced. I am very grateful to Nolwenn Chauché, whose patience and mental fortitude produced a truly incredible dataset for submarine processes at Store Glacier, and who got me about as close to iceberg calving as I'm ever likely to be, or indeed wish to be.

To Doug Benn, I am very thankful for starting me down this icy path which now brings me back into his inspirational company.

For helping me keep a sensible work/life balance, I am extremely grateful to all my friends and family. Kate and Joe, having you guys just round the corner is, and always will be, one of my fondest memories. To James and Tina, Rob and Anke, Rajiv, Jordi, Milhan, Ambroise, Sophie, Irina, and Tom, thanks for helping me realise that wearing a bowtie doesn't mean you can't have fun! To Iain, Ben, Ross, Allan, Calum, and Alex, thanks for reminding me that I'd rather not wear a bowtie. To Mum and Dad, thanks for all your love and support and for putting me up and putting up with me over the past few months. To my sister, Hannah 'RK' Todd, thanks for coming to my aid in my time of need and for being a pal.

Finally, for her constant and unwavering belief in me, her patience and kindness, and for picking me up when I fall, I am, and always will be, truly indebted to my wife, Amanda. Siempre te amaré.

The traveller who winds his tortuous and sometimes perilous path among these crevasses, forgets, in the fatigue of his circumventions, in the wonder of his curiosity at their beauty and seemingly unfathomable depth, in the appalling steepness of their sides and the comparative insecurity of his own footing - he forgets, I say, in the midst of all these claims upon his attention, his curiosity, and his strength of mind, the comparatively large surfaces of unbroken ice over which he heedlessly walks, and the small, the very small depth at which most of the yawning crevasses which make such an impression on his imagination, dwindle into mere slits...

— James David Forbes

Illustrations of the Viscous Theory of Glacier Motion

Contents

Nomenclature

Acronyms

AIS	Antarctic Ice Sheet
BC	Boundary Condition
DEM	Digital Elevation Model
FEM	Finite Element Method
GIS	Geographical Information Systems (Software)
GL	Grounding Line
GrIS	Greenland Ice Sheet
LEFM	Linear Elastic Fracture Mechanics
ODE	Ordinary Differential Equation
PDE	Partial Differential Equation
PDF	Probability Density Function
PMP	Pressure Melting Point
SIA	Shallow Ice Approximation
SMB	Surface Mass Balance
SSA	Shallow Shelf Approximation
TSX	TerraSAR-X
UAV	Unmanned Aerial Vehicle
USF	(Elmer) User Function

Variables

A	Arrhenius Factor
a	Accumulation
A_0	Arrhenius Factor at $-10\,°\mathrm{C}$
β	Slip Coefficient
d	Depth
$\boldsymbol{d}$	Mesh Displacement (Vector)
$\dot{\boldsymbol{\epsilon}}$	Strain Rate Tensor
g	Gravity
$\boldsymbol{g}$	Gravity (vector)
h_c	Thickness of Calving Front

H_{intact}	Intact Proportion of Ice Thickness
h_w	Water Depth
K_I	Stress Intensity Factor (LEFM)
$\dot{m}$	Melt Rate
n	Glen's Flow Law Exponent
P_W	Water Pressure
P_{wb}	Basal Water Pressure
Q	Activation Energy for Creep
q_{bf}	Heat Flux from Basal Friction
q_{strain}	Heat Flux from Internal Deformation
R	Gas Constant
ρ	Density
ρ_{fw}	Density of Fresh Water
ρ_{sw}	Density of Sea Water
ρ_i	Density of Ice
ρ_w	Density of Water
$\boldsymbol{\sigma}$	Cauchy Stress Tensor
σ_1	First Principal Stress
$\sigma_\perp$	Normal Stress
$\sigma_\parallel$	Tangential Stress
σ_{net}	Net Stress Acting to Open Crevasses
$\sigma_{net_{surf}}$	Net Stress Acting to Open Surface Crevasses
$\sigma_{net_{basal}}$	Net Stress Acting to Open Basal Crevasses
T	Temperature
τ	Deviatoric Stress
$\boldsymbol{\tau}$	Deviatoric Stress Tensor
τ_1	First Principal Deviatoric Stress
τ_E	Effective Deviatoric Stress
τ_b	Basal Friction
τ_E	Effective Deviatoric Stress
T_h	Degrees Below Pressure Melting Point
$\boldsymbol{u}$	Velocity (vector)
U_c	Calving Rate
$u_\perp$	Normal Velocity
$u_\parallel$	Tangential Velocity
W	Half Width of Glacier
z	Elevation
z_b	Elevation of Glacier Base
z_{sl}	Sea Level

List of Figures

CHAPTER 1

INTRODUCTION

This thesis describes the development, implementation and testing of a 2D and a 3D model for iceberg calving from outlet glaciers, and investigates the seasonal dynamics of the calving front of Store Glacier. The model is developed in the finite element ice flow model Elmer/Ice (Section 2.3) and implemented for a case study of Store Glacier, a calving outlet glacier in the Uummannaq region of West Greenland. This chapter outlines the rationale behind this investigation, discusses the aims of the study, and describes Store Glacier. Chapter 2 reviews recent literature and presents the theory which underpins the model development in this study. Chapters 3 and 4 describe the methods and present results from the 2D model, respectively. The 2D model was developed as a stepping stone to the more complex 3D model, the methods of which are outlined in Chapter 5. Chapter 6 presents the results of the 3D calving model of Store Glacier, which represents the main outcome of this study. Finally, Chapter 7 draws together the findings of both the 2D and 3D models, discusses the wider implications of this study, and outlines priorities in future model development.

1.1 Rationale

This project addresses the problem of predicting mass loss due to iceberg calving from outlet glaciers. This 'dynamic' mass loss term represents a large, variable and *poorly constrained* component of the overall mass budget of the planet's ice sheets. Recent estimates suggest just under half of Antarctica's mass loss occurs via calving, with the other half dominated by submarine melting under ice shelves (Depoorter et al., 2013). In Greenland, between 32-67 % of mass loss

occurs through calving (Enderlin et al., 2014; Rignot and Kanagaratnam, 2006).

The significant contribution of iceberg calving to ice sheet mass loss means that predictions of sea level rise will depend critically on our ability to predict changes in this process in a changing climate.

1.1.1 Sea Level Rise

Predicting sea level rise into the coming century and beyond is of significant socio-economic importance. Earth's population is preferentially concentrated around coastal regions; around 10 % of the global population currently live within 10 m of current sea level (McGranahan et al., 2007). Rising sea level means a non-linear increase in the frequency of storm surges: 1 in 100 year events may become 1 in 10 year events, for example (Paasche and Støren, 2014). Coastal flooding of this kind causes severe and diverse disruption to human settlements, from transportation and utilities, to sewage disposal, agriculture and drinking water, not to mention the direct death toll of such events (Intergovernmental Panel on Climate Change, 2014).

The disruption of coastal communities is a global problem, but there are significant regional differences in adaptability. Storm surge barriers in the UK (e.g. the Thames Barrier) and the Netherlands mitigate the flooding risk in these areas. However, such mitigation strategies are prohibitively expensive in most of the developing economies which are at increasing risk from sea level rise.

If we further consider that, historically, it is economically more developed countries (EMDCs) which have contributed disproportionately to global carbon emissions, sea level rise highlights the issue of 'climate injustice', whereby those most responsible for climate change are also the least affected by it.

Mitigation of and adaptation to global sea level rise are already underway in many parts of the world. However, for these adaptations to be effective requires accurate *prediction* of the change to come. A flood defence may be designed and built at great cost to protect against 50 cm of sea level rise, but if the rise exceeds this threshold, such a defence would prove ineffective. Conversely, fortifying all of the world's coastal communities against 20 m of sea level rise would provide poor value for money if sea level rise never exceeded 1 m.

1.1.2 Predicting Calving

The non-dynamic mass loss components (i.e. surface and basal melting) are significant, but well constrained. Surface melt varies in response to changes in atmospheric temperature, wind speed, insolation and other factors. Overall, however, the processes involved are sufficiently simple and well studied that a good first-order prediction is obtained by simple 'degree day' models, which relate melting to some cumulative measure of positive temperatures over time (Hock, 2003).

Submarine melting is perhaps less well understood, due to the logistical difficulty of observing these processes, but recent advances in plume theory (Jenkins, 2011), ice-ocean interaction modelling (Cowton et al., 2015; Slater et al., 2015) and oceanographic survey (Rignot et al., 2010; Straneo et al., 2011) mean that these processes can be increasingly well constrained.

Of course, predictions from models of melt processes can only ever perform as well as their input data, but this is an issue of atmospheric, oceanographic, and perhaps even political science. Glaciologically, these processes are well understood.

Calving processes and their links to dynamics, on the other hand, are poorly constrained for various reasons. First and foremost, these processes are complex; calving is a fracture process operating at various timescales from instantaneous crack growth to the multi-year progression of rifts in Antarctic ice shelves (Bassis et al., 2008). Secondly, glacier dynamics are often largely controlled by conditions and processes at the bed, which is difficult to observe. Finally, calving modelling as a field of research is still in its relative infancy. Only recently has it been recognised that changes at calving termini can significantly affect upstream ice and that these changes can trigger non-linear feedback loops (Holland et al., 2008; Nick et al., 2009; Price et al., 2011)

For the reasons stated above, there is an urgent need for progress in the modelling of iceberg calving and its links to dynamics, in order to better predict the future of the Greenland and Antarctic ice sheets and their contribution to sea level rise.

1.2 Aims & Objectives

The primary aim of this project is to address the inability of ice sheet models to accurately capture calving processes. In addressing this broad aim, I hope also to improve understanding of the processes which link calving to climate. To achieve these aims, I set out the following objectives:

- Develop and test a 2D calving model in the glacier dynamic model Elmer/Ice.
- Develop and test a 3D calving model, based on the previously implemented 2D model.
- Test both models on a case study of Store Glacier.
- Compare the results of the 2D and 3D models, and compare both to observations.

1.3 Store Glacier

Store Glacier is a large, tidewater glacier in the Uummannaq region of West Greenland (Fig. 1.1), whose terminus is located at 70.37N, 50.57W. It discharges an estimated 14-18 $\mathrm{km^3\,a^{-1}}$ into its fjord, making it the second largest calving glacier in West Greenland, after Jakobshavn Isbræ (Weidick and Bennike, 2007). Velocity data from InSAR reveal velocities at the terminus of up to 16 $\mathrm{m\,day^{-1}}$.

Store Glacier exhibits a strong seasonal signal in its terminus position; the mean seasonal range of the front is 500 m (Howat et al., 2010), with a local maximum towards the south of up to 1 km. However, despite the strong seasonality, Store's calving terminus appears to be stable on interannual timescales, during a period when other glaciers in the Uummannaq region (Howat et al., 2010), and much of Greenland (Seale et al., 2011), underwent sustained retreat.

Store's seasonality strongly implies a seasonal climate forcing, affecting the balance between the rate of iceberg calving and the rate of ice delivery to the terminus. However, the interannual stability implies an uncharacteristically *stable* terminus position, insensitive to the climate forcing which caused other glaciers in the region to retreat. This makes Store an interesting candidate for a study of calving processes.

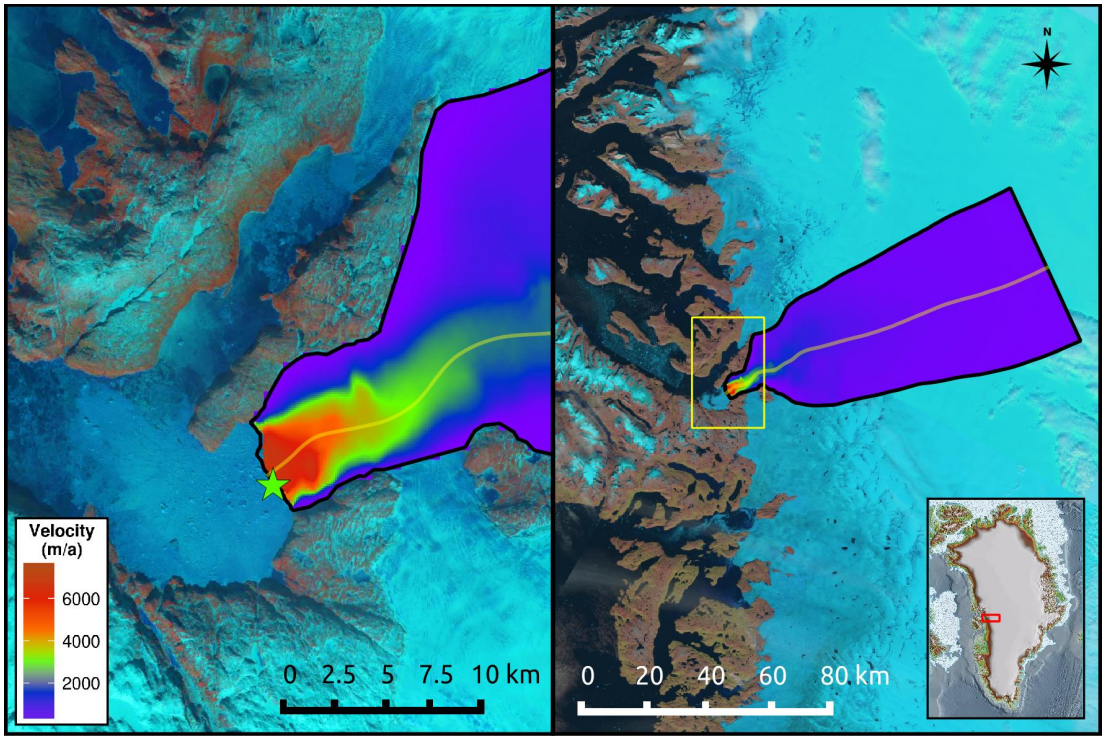

Figure 1.1: Site map showing Store Glacier, Uummannaq, West Greenland. Green star indicates location of most persistent proglacial plume. Yellow line represents flowline of 2D model.

Several potential seasonal drivers exist at Store which may influence calving rate and velocity at the terminus. Like many Greenland outlet glaciers, Store's pro-glacial fjord is occupied, during the winter months, by ice mélange, a rigid matrix of calved icebergs and sea ice (Section 2.2.4). At Store, the ice mélange typically forms in late January to early February and collapses around the end of May (Howat et al., 2010). Airborne survey by the IceBridge project (`https://espo.nasa.gov/missions/oib/`) measured a mélange thickness of 75 m in 2011, while more recent UAV survey (Section 1.3.2) found a thickness of 140 m in 2014.

Ice mélange has been suggested to exert a significant buttressing force on the termini of calving glaciers (Amundson et al., 2010), inhibiting crevasse opening and, as a consequence, reducing calving rate. Directly measuring the rheology of ice mélange to determine its strength is complicated for a number of reasons. As a granular material, it does not 'flow' in the conventional sense, and so bulk strain rates are difficult to determine. Furthermore, mélange is too dynamic to permit fieldwork to be carried out on its surface. However, estimates of the buttressing

force applied by the mélange on the terminus have been made, by observing the change in glacier velocity before and after its collapse. Walter et al., (2012) carried out such an investigation on Store Glacier, estimating from force balance that the mélange exerted a force of 30-60 kPa in 2008. The force balance method was also employed by N. Toberg on UAV data to estimate a buttressing force of 120 kPa for 2014. These estimates are not necessarily inconsistent in terms of estimating the mélange rheology: the total buttressing force depends on mélange thickness, which varies between years, as discussed above.

Store glacier is underlain by an active and seasonally variable subglacial hydrological system which discharges a large quantity of fresh meltwater at the base of the calving terminus, which in turn promotes force convective melting and may affect calving (Section 2.2.4). The meltwater which feeds this subglacial hydrological system can be partitioned into basal, englacial and surface melting. Basal and englacial melting occur year round, and are a product of friction, either strain heating in the case of englacial melting, or friction from basal deformation in the case of basal melting.

During the summer melt season, a large amount of surface melting occurs; this meltwater travels through moulins to the base of the ice sheet where it travels through the subglacial hydrological system to the terminus. The addition of this surface meltwater significantly increases the submarine melt rate driven by the forced convective plumes at the terminus. Oceanographic measurements suggest that the average submarine melt rate across the terminus varies from $2.2\,\mathrm{m\,d^{-1}}$ in winter to $4.5\,\mathrm{m\,d^{-1}}$ in summer (Chauché, 2016). Modelling work by Rignot et al., (2016) suggests values of $1.2\,\mathrm{m\,d^{-1}}$ and $2.8\,\mathrm{m\,d^{-1}}$, respectively.

Sidescan sonar and UAV imagery (Section 1.3.2) indicate that submarine melting is not evenly distributed across the terminus. Melt rates can be locally as high as $12\,\mathrm{m\,d^{-1}}$ in regions where concentrated subglacial discharge, which result in more vigorous forced convective plumes and more melting.

1.3.1 Geometry

Glacier geometry and topography has previously been suggested to explain observed differences in calving behaviour between glaciers exposed to the same climatic conditions (Vieli et al., 2001; Warren, 1991). Store glacier's catchment extends 280 km inland to the ice divide, reaching a maximum width of 50 km

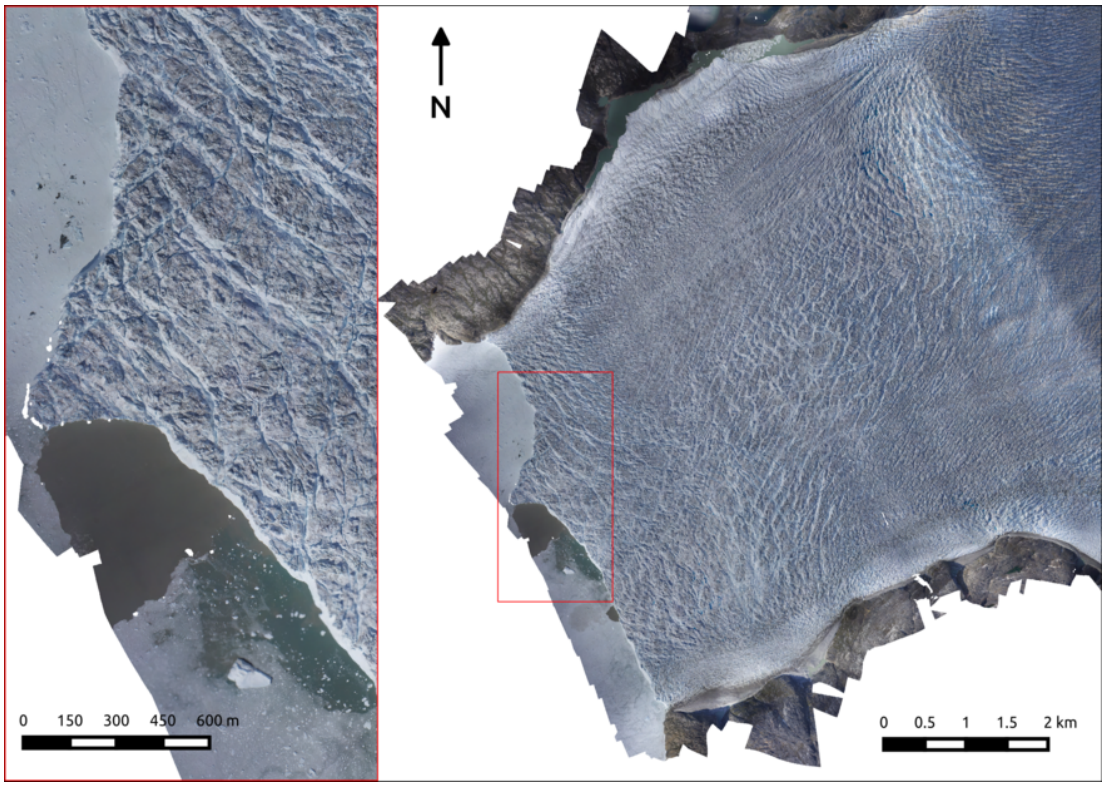

Figure 1.2: Orthophoto of Store Glacier's terminus from UAV imagery. Extensive crevassing of the terminus is clearly visible, with crevasses both parallel to and intersecting the front. The large patch of dark water in the inset figure indicates the presence of an active buoyant plume.

before narrowing to 5 km at the terminus. Basal topography is difficult to determine to sufficient resolution for dynamic modelling. Radar flight lines provide accurate data along the chosen flight path, but interpolation between these flight lines is challenging and problematic (Morlighem et al., 2011). To address this, part of this project involves the use of mass conservation techniques to determine the bed topography under Store Glacier to better serve the flow model. Details of the mass conservation method are discussed in Appendix A.2, and the resultant bed map is shown in Figure 1.3.

Figure 1.3 shows that the final 30 km of Store glacier flows through a significant overdeepening (up to 900 m below sea level) before flowing over a raised sill (470 m below sea level) which peaks at the terminus. At the terminus, concurrent with this raised bedrock sill, the glacier flows through a valley constriction, which is at its narrowest near the terminus. The potential for these characteristics of the glacier's geometry to influence calving rate is discussed in Section 2.2.3.

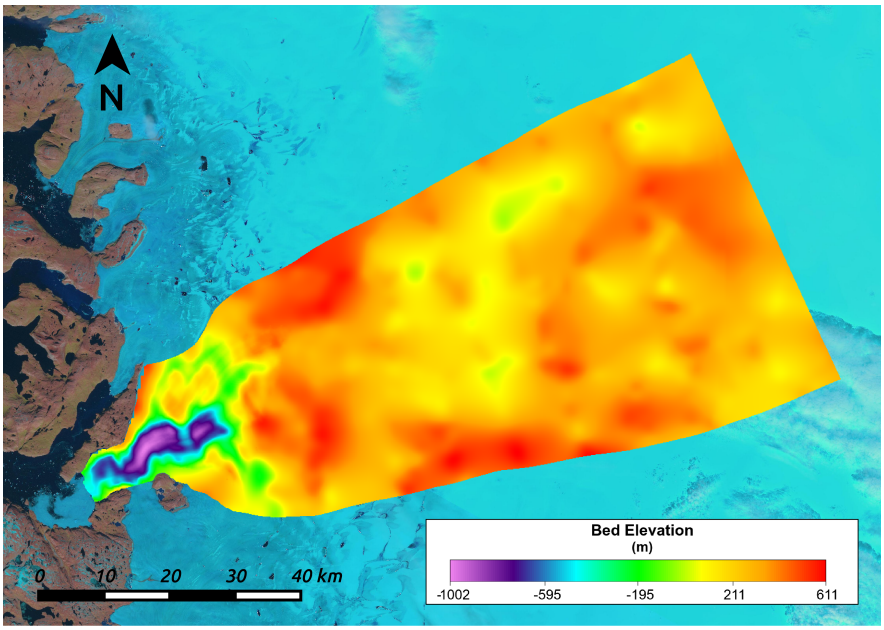

Figure 1.3: Map of Store Glacier's basal topography, derived from airborne radar data and mass conservation.

1.3.2 Field Campaign

The decision to use the model to investigate calving processes at Store Glacier was motivated in part by an ambitious field project carried out by researchers from the Scott Polar Research Institute (SPRI), in collaboration with Aberystwyth University. This field campaign began in 2014 and will continue until 2021 and is composed of multiple separate projects attempting to answer questions about the basal conditions, subglacial hydrology and processes at Store's calving terminus, the latter being the most relevant to the present study.

The calving component of the field campaign was led by researchers at Aberystwyth University, namely A. Hubbard, J. Ryan, N. Chauché and N. Snooke, as well N. Toberg and J. Todd from SPRI. Calving termini are notoriously difficult to study given the dangers inherent to approaching them by boat. Nonetheless, a large quantity of data was gathered by boat from near the terminus of Store, including CTD casts to gather oceanographic information and sidescan sonar, used to map the ice front's geometry.

The most novel part of this field campaign was the deployment of Unmanned Aerial Vehicles (UAVs) to survey the terminus of Store Glacier. These low-cost platforms were fitted with digital cameras, and they were used to carry out daily

surveys during the late spring to early summer of 2014. Photogrammetry was used to construct 3D models of the terminus from the collected imagery. The resulting geometric models carry a wealth of information about Store's terminus, including ice velocity, size and frequency of calving events, strength of ice mélange, and location and duration of buoyant plumes.

This UAV survey, alongside timelapse imagery, oceanographic and sonar survey, as well as drilling, radar and seismic survey on the inland ice, provide an unprecedented data density of a Greenland outlet glacier. This makes Store an ideal candidate for an investigation of calving processes: a large quantity of data exists to constrain the geometry and basal conditions of Store to drive the model, and high spatial and temporal resolution data from the terminus provides a benchmark against which to test the calving model's performance.

CHAPTER 2

Literature & Theory Review

This chapter combines a review of the literature relevant to this study, and an overview of the mathematical and scientific theory underpinning both the 2D and 3D models. Section 2.1 briefly outlines how the flow of ice is represented in numerical models. Section 2.2, which forms the bulk of this chapter, discusses iceberg calving, the processes which link it to climate, previous calving models, and outlines the theoretical basis of the crevasse depth model which is used in this study. Section 2.3 briefly describes Elmer/Ice, the finite element model used in this investigation.

2.1 Glacier Dynamics

The main objective of this project was the implementation of a model for iceberg calving; however, the core of the model, and the most computationally expensive component, is the solution of the equations which describe the flow of ice.

Ice is an incompressible, viscous fluid with a low Reynolds number; as such, its flow can be described and predicted using the incompressible Stokes equations:

$$\nabla \cdot \boldsymbol{\sigma} + \rho \boldsymbol{g} = 0 \tag{2.1}$$

$$\nabla \cdot \boldsymbol{u} = 0 \tag{2.2}$$

where $\nabla \cdot \boldsymbol{\sigma}$ is the divergence of the Cauchy stress tensor, ρ is the density of the material, $\boldsymbol{g}$ is acceleration due to gravity, and $\nabla \cdot \boldsymbol{u}$ is the divergence of the velocity field. Equation 2.1 describes the fact that ice deforms under its own

weight, while Equation 2.2 dictates that the flow into and out of any arbitrary volume of ice must be equal (incompressibility).

I assume ice to be isotropic, and thus its stress-strain relationship is described by the Nye-Glen flow law (Cuffey and Paterson, 2010):

$$\dot{\epsilon}_{jk} = A\tau_E^{n-1}\tau_{jk} \tag{2.3}$$

where $\dot{\epsilon}$ is the strain rate tensor, A is the Arrhenius factor (or rate factor), n is usually taken equal to 3, $\boldsymbol{\tau}$ is the deviatoric stress tensor, and τ_E refers to the effective stress, the second invariant of the deviatoric stress tensor. I use Einstein notation, such that use of the subscripts j and k signifies that Equation 2.3 holds true for every $\{j, k \in 1, 2, 3\}$.

The presence of the exponent $n > 1$ in Equation 2.3 indicates that ice obeys a nonlinear flow law, making it a non-Newtonian fluid. The Arrhenius factor, A, describes the 'softness' of the ice, and is primarily dependent on the temperature of the ice. The relationship between temperature and the Arrhenius factor (A) is described by the Arrhenius equation:

$$A = A_0 e^{-\frac{Q}{RT_h}} \tag{2.4}$$

where A_0 is the calibrated rate factor at a temperature of $-10\,°\mathrm{C}$, Q is the activation energy for creep and R is the gas constant. T_h signifies the temperature below freezing point; this is the actual temperature in Celcius (or Kelvin), minus the pressure dependent melting point (PMP). In other words, T_h is 'degrees below freezing'.

The behaviour of the relationship described by Equation 2.4 changes sharply at a temperature of $-10\,°\mathrm{C}$, and so different values of A_0 and Q are used above and below this temperature.

2.1.1 Lower Order Approximations

In the glacier modelling community, models which solve Equations 2.1 and 2.2 are referred to as full-Stokes models. However, the nature of these equations makes

them computationally expensive to solve, and in many situations, lower order approximations can produce very similar results, for significantly lower computational cost. These lower order approximations generally involve the dropping of certain components from the force balance (Eq. 2.1), justified by the fact that ice sheets are wide and shallow.

The Shallow Ice Approximation (SIA) (Hutter, 1983) forms the basis for most lower order approximations presently employed in the study of the flow of ice. The SIA neglects all stress terms except for horizontal plane shear stresses (τ_{xz},τ_{yz}) and so effectively assumes that driving stress is entirely balanced by basal drag. While the SIA provides a reasonable approximation in ice-sheet interiors where ice flow is dominated by internal deformation, its suitability decreases as basal sliding increases (Gudmundsson, 2003) and longitudinal stress gradients begin to play an important role in the force balance. In the case of a floating ice-shelf, resistance from basal drag is entirely replaced by lateral drag, and the Shallow Shelf Approximation (SSA) (Morland, 1987) provides a more suitable lower order approximation for this situation.

Various 'higher-order' approximations have arisen from the SIA and SSA, but all involve neglecting stress components to improve efficiency. Iceberg calving is, fundamentally, a process of fracture in response to stress, and so an accurate stress field, and in particular an accurate representation of *vertical variations in stress*, is essential. The complex geometry of calving outlet glaciers, the transition from deformation-dominated to sliding-dominated flow, as well as specific stress effects such as ice cliff force imbalance (Section 2.2.3) and buoyant bending forces (Section 2.2.3) motivated the decision to opt for full-Stokes modelling in this study.

2.2 Calving

Calving from outlet glaciers accounts for over half of mass loss from the Antarctic Ice Sheet (Depoorter et al., 2013), and around half of that from the Greenland Ice Sheet (Enderlin et al., 2014; Rignot and Kanagaratnam, 2006). Thus, changes in these systems, driven by climate or internal dynamics, can effect a significant shift in the mass budget of these ice sheets. This in turn can have a significant effect on sea level. This motivates an urgent need to understand and predict

these systems, and their response to projected changes in the climate and ocean systems.

Calving glaciers are diverse in their geometry, dynamics and environmental setting. Furthermore, for any given calving glacier, icebergs may detach through a variety of mechanisms, and the processes linking these mechanisms to climate are often poorly understood. This complexity, combined with the difficulty of collecting data from these often remote and dangerous settings, makes dynamic mass loss from calving glaciers one of the most poorly constrained contributors to sea level rise in the 21st century and beyond (Vaughan and Arthern, 2007).

2.2.1 Previous Calving Models

Early attempts to model calving focused on developing empirical relationships between calving rate, or terminus position, and other measurable quantities. The rate of calving at Columbia Glacier, for example, has been observed to correlate with the depth of water at the terminus (Brown et al., 1982), prompting the authors to propose a calving law of the form:

$$U_c = ch_w \tag{2.5}$$

where U_c is the rate of calving, h_w is water depth at the terminus, and c is a tuned parameter fitted to the dataset. Equation 2.5 provided a good predictor for annually averaged calving rates from 13 Alaskan calving glaciers studied by Brown et al., (1982), with $c = 27\ \mathrm{a}^{-1}$. Unfortunately, Haresign, (2004) showed that the appropriate value of c varied from region to region. Furthermore, while the water depth model may provide valuable insight into the expected behaviour of a calving glacier following its initial retreat into deeper or shallower water, it can provide no trigger for this initial change. This limits its value as a prognostic tool.

An alternative relationship was proposed by Van der Veen, (1996), also based on the record from Columbia Glacier. This was motivated by the observation that the glacier terminus always seemed to maintain a certain height above buoyancy. The thickness at which glaciers begin to float is determined by the depth of water into which they flow, and the ratio of the density of ice and water. Van der Veen, (1996) observed that Columbia Glacier tended to remain 50 m above this

thickness:

$$h_c = \frac{\rho_w}{\rho_i} h_w + 50 \tag{2.6}$$

where h_c is the thickness of the calving front. Van der Veen, (1996) noted that if the terminus thickness dropped below this critical thickness, the glacier would retreat until the condition was once again satisfied.

The physical basis for the flotation criterion (Eq. 2.6) is based on basal water pressure and slip. As a glacier terminus approaches flotation due to thinning, the effective pressure, or apparent 'weight' of the ice approaches zero. This leads to a significant reduction in basal drag, as the ice begins to lose contact with the bed, and this acceleration and stretching can promote calving by deepening crevasses. The fact that stretching, induced by low effective pressure, leads to increased calving and instability of the terminus suggests that a glacier terminus has a minimum effective pressure required for stability. When effective pressure drops below this minimum, increased calving leads to retreat until the minimum is exceeded once again. Conversely, when the effective pressure is above the minimum, calving rate is reduced, and advance may occur.

Vieli et al., (2001) used a slightly modified version of Equation 2.6 in a time-evolving 2D Finite Element model of a synthetic glacier geometry, and investigated retreat and advance scenarios, driven by changes in mass balance. Basal topography was found to exert a strong control on calving rate; although changes in mass balance provided the *trigger* for change, the response of the glacier was highly modulated by basal topography. The calving terminus was found to advance and retreat rapidly over retrograde (reverse) bed slopes, while moving more slowly over normal bed slopes. Using the same model, Vieli et al., (2002) were able to reproduce the rapid retreat in 1990 of Hansbreen, Svalbard, lending support to the flotation criterion proposed by Van der Veen, (1996).

A key challenge for calving modelling is the diverse range of glaciological settings in which calving occurs. In an analysis of calving rate from Antarctic ice shelves, Alley et al., (2008) showed that over 95% of the variance in calving rate from those ice shelves could be explained by the relationship:

$$U_c = 0.039 \left(\dot{\epsilon} W\right)^{1.9} \tag{2.7}$$

where W is the half width of the ice shelf, and $\dot{\epsilon}$ is the 'spreading rate', or the horizontal strain rate. However, the study was limited to ice shelves which were in steady state, and so the capacity of this relation to predict future change seems limited. Furthermore, because Alley et al., (2008) only investigated steady state ice shelves where, by definition, calving rate is equal to terminus velocity, Equation 2.7 may only be a predictor of terminus velocity (Hindmarsh, 2012).

There is a fundamental difference between the approach to predicting calving represented by Equations 2.5 and 2.7, and that of Equation 2.6. The water depth model and the strain relation of Alley et al., (2008) attempt to predict the rate at which calving events occurs, while the height above buoyancy model attempts to predict the location of the calving front. This difference delineates two different ways of thinking about calving (Benn et al., 2007b). One approach suggests that calving rate is directly controlled by environmental factors, and that the terminus position is a passive quantity, the difference between the calving rate (U_c) and the velocity at the terminus (U_t). Alternatively, one considers that the environment drives changes in terminus position and that calving rate is simply controlled by the rate at which ice is delivered to the terminus U_t. In fact, the following analysis of calving processes and their links to climate will suggest that this may be a false dichotomy; internal and external processes can both affect calving rate directly, but many glaciers are observed to occupy preferentially stable terminus positions.

2.2.2 The Crevasse Depth Model

The calving relations presented in the previous section are all, in some sense, empirical. The flotation criterion has a firm theoretical basis, but the 'height above flotation' must still be chosen to fit observations. These empirical models are useful because the correlations that they represent hint at the underlying physical processes which control calving. The height above buoyancy criterion, for example, suggests that basal friction may inhibit calving. As glaciers approach flotation, they begin to lose contact with their bed and, as a result, lose friction. The observation that terminus height must remain some quantity above flotation (Eq. 2.6) suggests that the loss of this friction promotes calving.

However, while empirical calving laws can be useful diagnostic tools, they are of limited use prognostically. Instead, a universally applicable calving law should

describe and predict the *physical processes* involved in calving. The crevasse depth model proposed by Benn et al., (2007b), based in part on the work of Van der Veen, (1998a,b), and further developed by Nick et al., (2010) and Otero et al., (2010), is an attempt to model calving in such a physically based manner.

Underpinning the crevasse depth model is the observation that calving occurs when crevasses penetrate the full thickness of the glacier. This somewhat tautological statement, in itself, tells us nothing new about the calving process. It does, however, provide a physical starting point for a model of calving. If crevasse penetration could be predicted in a numerical model, then so too could the timing and size of calving events.

Crevasses on glaciers, like any kind of material fracture, open in response to stress. Fracture mechanics identifies three modes of fracture opening (Fig. 2.1). In the lateral shear margins of a glacier, Mode II shear fracturing can occur, but at the termini of calving glaciers, crevasses are primarily opened directly via tension (i.e. Mode I).

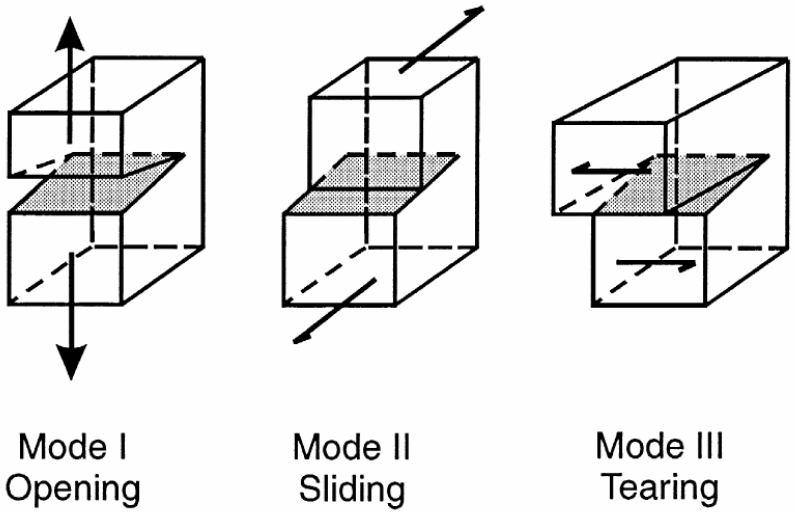

Figure 2.1: The 3 modes of fracture opening under stress. Source: Van der Veen, (1998b)

Mode I fracturing dominates at calving termini due to the overall stress regime which typifies these parts of a glacier. As the glacier flows, usually downhill, into its pro-glacial water body, it approaches flotation, basal drag is diminished and the ice accelerates. Thus, the stress field is dominated by high longitudinal (along flow) extensional strain rates.

Linear Elastic Fracture Mechanics

A single, isolated Mode I fracture in ice results in a stress concentration at the crevasse tip. The opening and evolution of such a crevasse is examined using the Linear Elastic Fracture Mechanics (LEFM) approach by Van der Veen, (1998a,b), for surface and basal crevasses respectively.

The concentration of stress around the crevasse tip is described by the *stress intensity factor* (K_I):

$$K_I = \beta\sigma\sqrt{\pi d} \tag{2.8}$$

where d is the depth of the crevasse, and the parameter β depends on the geometry of the crevasse. This, in turn, is used to describe the stress field in the region around the crevasse:

$$\sigma_{ij} = \frac{K_I}{\sqrt{2\pi r}} f_{ij}(\theta) + \text{ other terms} \tag{2.9}$$

where r is the distance from the crevasse tip, and $f_{ij}(\theta)$ is a function of the angle from the crevasse tip. The 'other terms' essentially refer to the broader scale state of stress in the ice; as the distance from the crevasse tip (r) increases, the first term on the right of Equation 2.9 tends to zero, and σ_{ij} approaches a 'background' value determined by the bulk dynamics of the glacier in that region. Conversely, as r approaches zero, Equation 2.9 predicts that stresses will approach infinity but, in reality, plastic deformation prevents this (Van der Veen, 1998b).

LEFM further states that fractures will grow when the stress intensity factor exceeds a critical value (K_{Ic}), called the fracture toughness, whose value has been estimated experimentally to lie within the range 0.1-0.4 $\mathrm{MPa}^{1/2}$ (Van der Veen, 1998b).

The parameter β in Equation 2.8 depends on geometrical factors such as the ratio of crevasse depth to glacier thickness, and the spacing of crevasses. As crevasse spacing decreases, β decreases substantially, reducing the value of K_I. This describes the phenomemon of crevasse 'shielding', whereby closely spaced crevasses inhibit the build up of stress concentrations at crevasse tips (Sassolas et al., 1996) to such an extent that the stress intensity factor becomes negligible (Cuffey and Paterson, 2010).

The Nye Approach

In a model for calving from an outlet glacier, I am interested in the evolution of a very closely spaced field of crevasses near the terminus. As such, the stress intensity factor can be neglected, and it can be said that crevasses will exist wherever there is tensile stress (Nye, 1957). Given this, Nye, (1957) states that surface crevasses on glaciers will exist to a depth (d) where:

$$\rho g d = 2\tau_{xx} \tag{2.10}$$

This equation represents the balance of two forces: on the left, ice overburden pressure acting to close the crevasse, and on the right, the horizontal deviatoric stress acting to open it. Rearranging Equation 2.10 and using Glen's Flow Law (Eq. 2.3) to replace stress with strain, I arrive at the formulation of Benn et al., (2007b) for the prediction of surface crevasse depth:

$$d = \frac{2}{\rho g}\left(\frac{\dot{\epsilon}_{xx}}{A}\right)^{1/n} \tag{2.11}$$

under the assumption that ice is flowing in the x direction.

In fact, Equations 2.10 and 2.11 are simply decompositions of the statement "crevasses exist where there is tensile stress", formulated in such a way as to be calculable from surface measurements; by assuming that τ_{xx} (or $\dot{\epsilon}_{xx}$) is constant through depth, and that the overburden pressure increases at ρg [$\mathrm{Pa\,m^{-1}}$] through depth, crevasse depth can be predicted from the surface.

Hydrofracturing

It has been established that the opening of a crevasse in a glacier is controlled by the balance between extensional stresses in the ice opening and ice creep closing forces. However, water can provide an additional opening force, if present. The deepening of crevasses through the opening force of water is known as *hydrofracturing*. Hydrofracturing provides a potential link between calving and climate; more or less surface meltwater in crevasses will affect their depth.

The effect of hydrofracturing on surface crevasses can be accounted for by

adding a term to Equation 2.10:

$$\rho g d = 2\tau_{xx} + \rho_w g d_w \tag{2.12}$$

where ρ_w and d_w are the density and depth of the water in the crevasse, respectively.

The process of hydrofracturing also underpins the crevasse depth calving model as presented by Benn et al., (2007a,b), who hypothesise that a surface crevasse which reaches sea level near the calving terminus will begin to fill with water from its proglacial water body (sea or lake). As water is added to this crevasse, it will extend deeper, permitting more water to enter, and so on, until the crevasse reaches the base, and a calving event occurs.

There is an important assumption underlying the above; the terminus must be sufficiently crevassed to permit water to flow from the proglacial water body into the crevasse in question. The aerial orthophoto of the terminus of Store Glacier (Fig. 1.2) reveals extensive crevassing, with crevasses both parallel to and intersecting the front, suggesting that this assumption is valid.

Thus, the crevasse depth model (Benn et al., 2007a,b) can be summarised as follows:

1. The depth of surface crevasses is predicted by Equation 2.11

2. Calving occurs when surface crevasses reach sea level.

Basal Crevasses

In addition to the observable surface crevasses on calving glaciers, basal crevasses have been detected underneath glaciers (Christoffersen et al., 2005; Harper et al., 2010) and ice shelves (Jezek et al., 1979; Swithinbank, 1977), and are predicted to occur in settings where basal water pressure is high and extensional stress exists (Van der Veen, 1998a). James et al., (2014) suggest that these basal crevasses may play an important role in calving from Helheim Glacier in East Greenland.

Nick et al., (2010) proposed a modification to the crevasse depth model of Benn et al., (2007a,b) to account for basal crevasses. The force balance which dictates basal crevasse growth is the same as that for a surface crevasse containing water (Eq. 2.12), except the water pressure term is controlled by the basal

hydrological system:

$$\rho g d = 2\tau_{xx} + P_w \tag{2.13}$$

where P_w is water pressure.

The crevasse depth model of Nick et al., (2010) is then:

1. Depth of surface crevasses is predicted by Equation 2.11
2. Height of basal crevasses is predicted by Equation 2.13
3. Calving occurs where surface and basal crevasses meet.

Both the surface and basal crevasse models have been implemented by various authors into ice dynamic models of varying degrees of complexity. Cook et al., (2012) tested the sensitivity of the surface crevasse model in a 2D full-Stokes model of Columbia Glacier. They found that the model was very sensitive to the depth of water in surface crevasses; an increase of a few metres switched the simulated Columbia Glacier from advance to retreat.

Vieli and Nick, (2011) applied the basal crevasse depth calving criterion in a 1D flowline model of Jakobshavn Isbræ, and found that the inland glacier dynamics were strongly coupled to changes at the terminus, suggesting that the loss of the floating tongue is the likely cause for its rapid retreat and acceleration. They also found that stability was very sensitive to small changes in water depth in surface crevasses.

The model's sensitivity to water depth is a significant issue, because the depth of water in surface crevasses is difficult to ascertain. There is no way to measure it using remote sensing of any kind, and although it could be directly measured, the heavy crevassing near the terminus makes their survey on foot a practical impossibility. Furthermore, while it is certainly possible to model the *production* of meltwater at the surface, the actual depth in the crevasse depends greatly on the crevasse geometry and whether the water can drain.

Finally, Otero et al., (2010) implemented the surface crevasse model into a non-time evolving 3D model for Johnsons Glacier, Antarctica. They proposed a modified version of Equation 2.11 which includes the second invariant of the strain tensor ('effective strain'), and lacks the factor of 2. Using their modified criterion, their model produced a reasonable match to the observed terminus position.

2.2.3 Processes Affecting Calving

The previous section highlighted the importance of stress in controlling calving. Tensile stress within glaciers causes crevasses to open, and the penetration of these crevasses leads to calving events. Thus, in seeking to understand the internal and external processes related to calving, it is expected that processes which enhance tensile stress near the terminus may induce calving, while those which reduce tensile stress may inhibit calving. Based on this idea, Benn et al., (2007b) proposed a hierarchy of processes which control or influence calving rate. On the broadest scale, a glacier's stress regime is largely controlled by its geometry and topography (Section 2.2.3), and so these form the first-order control on calving rate. Local stress regime can be greatly influenced by processes such as melt undercutting (Section 2.2.4), ice cliff force imbalance (Section 2.2.3) and buoyant forces (Section 2.2.3), and so these can be considered to be second-order processes.

Glacier Dynamics & Geometry

As discussed in Section 2.2.2, calving glaciers typically accelerate as they approach the terminus, due to diminishing basal drag associated with higher water pressure. Along flow acceleration leads to positive longitudinal strain rate (stretching) and crevasse formation. This persistent longitudinal stretching which arises as a glacier approaches flotation probably explains the good performance of the height above buoyancy calving model (Section 2.2.1).

At the broadest scale, the flow of ice downhill into a water body makes longitudinal stretching and crevassing almost inevitable; however, at smaller scales, glacier geometry and topography can exert a significant influence on this broad scale pattern. Longitudinal strain rate can be locally affected by changes in the resistive stress provided by the bed and sidewalls. Bedrock bumps, referred to in the context of calving as *pinning points*, may locally inhibit calving by reducing longitudinal tensile stress. As the ice flows over the stoss-side of the pinning point, the backstress from the obstacle generates compression (Fig. 2.4). Conversely, on the lee-side of the obstacle, basal drag is rapidly lost, leading to acceleration, crevassing and promoting calving. Local valley constrictions can have an analogous effect via the gain and loss of lateral drag.

In the case of Store Glacier, the terminus rests on both a large basal pinning point and at a valley constriction, which may explain its stability during a period

when other glaciers in the region underwent concurrent retreat (Howat et al., 2010). However, behind this stable pinning point, Store flows through a deep 30km long trough; the potential consequences of such large scale topographic features on long term calving glacier stability are discussed in Section 2.2.5.

Ice Cliff Force Imbalance

Superimposed on the broader pattern of longitudinal stretching is the local effect of the terminus 'ice cliff'. Due to the density difference between ice and water, calving glaciers always terminate with some degree of sub-aerial ice cliff, even when floating. The more grounded the terminus, the greater the height of this ice cliff compared to the submarine portion.

Figure 2.2 demonstrates that the forces at the ice cliff are always out of balance (Reeh, 1968). Descending from the upper ice surface, overburden pressure increases the outward force at a rate of $\rho_i g$ Pa m^{-1}. This outward force is essentially unopposed by atmospheric pressure, until the waterline is reached. Below the waterline, the back force from the proglacial water body increases at $\rho_w g$ Pa m^{-1}. Given that $\rho_w > \rho_i$, the back force from the water body increases more rapidly with depth than the outward force from the ice. For a glacier at or beyond the point of flotation, the net force will reach zero at the base of the glacier.

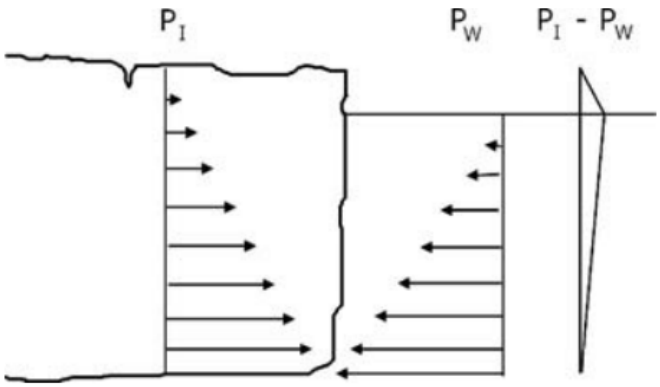

Figure 2.2: The permanent ice cliff force imbalance, which results in a top-first rotational torque. Source: Benn et al., (2007b)

The overall effect of this force imbalance is equivalent to a rotational torque (Fig. 2.2) acting to pull the top of the terminus forward. This will act to open surface crevasses around one ice thickness from the terminus (Benn et al., 2007b),

but may also close basal crevasses. The effect of this rotation torque on calving will depend on how grounded the terminus is. If the glacier is well grounded, the magnitude of the force imbalance will be greater, but the height of the maximum outward force will be closer to the centre of the glacier. Thus, although the overall magnitude will be greater, this may diminish the rotational nature of the force. At a floating terminus, basal crevasses are believed to be important for calving, and so this force imbalance may act to inhibit calving.

Buoyant Forces

For calving glaciers whose termini reach flotation, buoyant forces can be an important modulator of calving. A glacier's floating tongue is akin to a lever, pivoting on the grounding line, and changes in the buoyant forces at the terminus can result in increased stresses near the grounding line. Sources of perturbation to buoyant forces can come from tidal forcing (MacAyeal et al., 2006; Reeh et al., 2003), preferential surface melting (Boyce et al., 2007; Warren et al., 2001), or from the flow of the ice near the grounding line (James et al., 2014).

The tide's ability to induce buoyant bending is clear: as sea level increases or decreases, the pressure exerted on the base of the floating tongue changes, resulting in bending forces. Melting at the surface can induce bending forces by bringing the tongue out of buoyant equilibrium. As mass is lost from the surface, the tongue finds itself below the height of flotation (superbuoyancy) and will bend upwards as a result. The opposite may occur via basal melting.

Dynamics may be capable of inducing bending forces (James et al., 2014; Reeh et al., 2003), depending on the topographic setting of the terminus. If, as is often the case, the glacier flows down into the proglacial water body, the ice behind the terminus will be forcing the front to flow out and down. This may result in local superbuoyancy, resulting in an upward bend as the terminus returns to neutral buoyancy. The extent to which this process amplifies the tensile stress at the grounding line depends on the rate at which ice is forced into superbuoyancy; a terminus flowing very slowly downward will have longer to adjust upwards than one flowing quickly.

Resolving Stresses Near the Terminus

This section has discussed calving processes, highlighting the fundamental importance of *stress* within ice as a driver of calving. Furthermore, it has been shown that, in addition to the large scale stress regime resulting from ice flow, local scale processes such as buoyancy and ice cliff force imbalance can have a significant effect on the near-terminus stress regime. Therefore, in seeking to accurately model calving, it is useful to be able to resolve the full stress regime of the glacier (Hindmarsh, 2012), particularly near the terminus where the ice breaks off to form bergs. In order to achieve this, I choose to solve the Stokes equations (Eqs. 2.1,2.2) fully, as opposed to one of the lower order approximations discussed in Section 2.1.1.

2.2.4 Linking Calving to Climate

There is a large body of evidence suggesting that calving glaciers are highly sensitive to changes in climate, both oceanic and atmospheric. This section first presents the empirical evidence for this sensitivity, with a focus on Greenland, before discussing various mechanisms hypothesised to link calving glaciers to climate.

Empirical Evidence

Recent interest in the stability of calving glaciers began with the onset of retreat of Jakobshavn Isbræ, Greenland's largest outlet glacier, in the late 1990s. This retreat, which began with the collapse of the floating tongue, resulted in sustained acceleration and thinning through the 2000s (Joughin et al., 2008). Jakobshavn's retreat, while alarming, might not be in itself necessarily indicative of a link to climate. However, observations of a seasonal signal in velocity (Luckman and Murray, 2005), and terminus position (Sohn et al., 1998) prior to this retreat strongly suggest a link to climate.

Further evidence linking calving to climate comes from the concurrent retreat of many of Greenland's outlet glaciers between 2001 and 2005. Seale et al., (2011) studied margin positions from satellite imagery, and found a marked north-south divide in behaviour; glaciers south of 69° retreated, while those further north remained stable, despite the similar seasonal patterns of all the glaciers studied.

The authors hypothesised that a perturbation in ocean circulation exposed the retreating glaciers to enhanced submarine melting, promoting calving and retreat.

Mass balance estimates from gravimetric survey (Khan et al., 2010) confirm the mass loss associated with the retreat observed by Seale et al., (2011). Figure 2.3 illustrates progressive mass loss concentrated around the margin. The mass loss appears to begin in the south east, between 2003-2007, and advance around the west coast between 2007-2009.

Howat et al., (2010) showed that oceanographic and atmospheric climate forcings are likely responsible for seasonal changes in the terminus position of many outlet glaciers in the Uummannaq region in West Greenland, including Store Glacier. Their results also indicated that some of the glacier termini in the Uummannaq region underwent concurrent retreat between 2000-2010, consistent with the findings of Seale et al., (2011), while others, including Store, maintained stable terminus position.

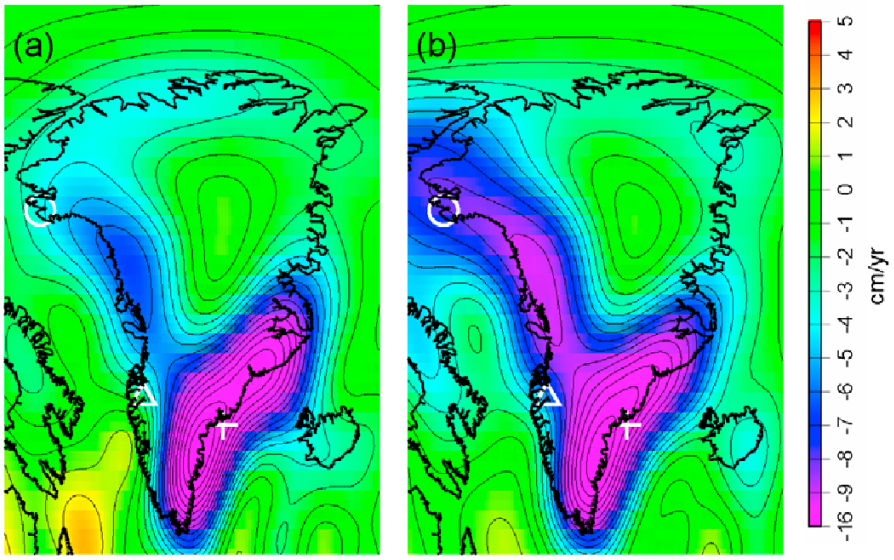

Figure 2.3: Mass loss (cm a^{-1} water equivalent) between (a) 2003-2007 and (b) 2003-2009, from gravimetric survey by GRACE satellites. Note that the intrinsically low resolution of gravimetric survey makes the mass loss appear more diffuse than reality. Source: Khan et al., (2010)

Submarine Melting

Various mechanisms have been proposed to explain the apparent sensitivity of calving glacier to changes in climate (Fig. 2.4). In recent years, the process which

has received the most interest has been submarine melting. The work of Seale et al., (2011) and Khan et al., (2010) strongly points towards an oceanic source for recent changes, and enhanced melting seems like an obvious explanation.

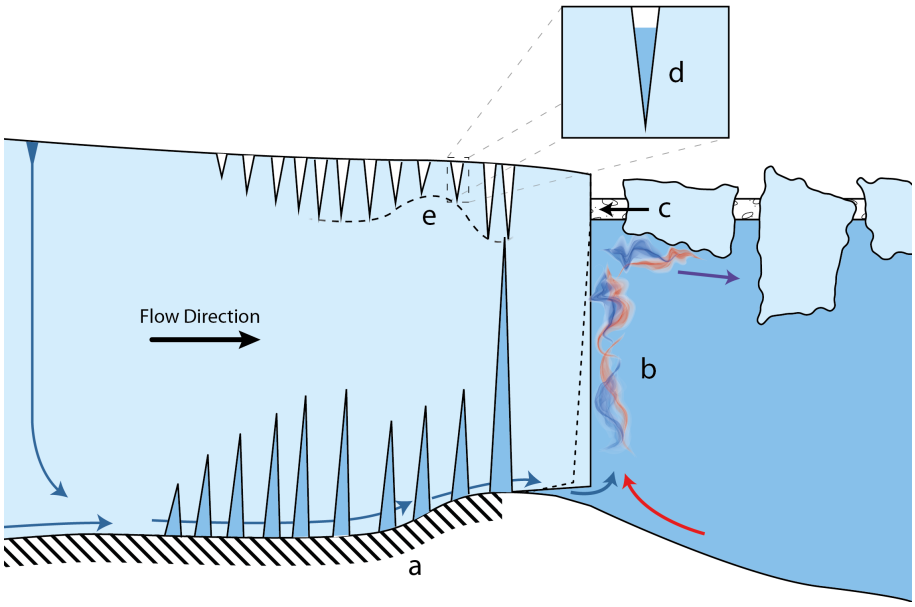

Figure 2.4: Schematic showing processes hypothesised to affect calving. (a) Changes in basal friction affect stresses near the terminus. (b) Increasing ocean water temperatures or surface meltwater supply increases submarine melt rates, undercutting the terminus. (c) Ice mélange forms in winter and buttresses the terminus, inhibiting calving. (d) Water in surface crevasses promotes crevasse growth through hydrofracturing. (e) Geometry influences sources of resistive stress, both at the bed and the lateral margins, promoting or inhibiting crevasse growth.

Holland et al., (2008) presented hydrographic measurements from near Jakobshavn Isbræ, indicating the arrival of warm subsurface waters coincident with the onset of retreat. Motyka et al., (2011) estimated from the observed increased in fjord temperature, a 25% increase in basal melting of the floating tongue after 1997. Increasing submarine melting of Jakobshavn's floating tongue would both directly promote calving by thinning, and also reduce the buttressing effect on the upstream ice, potentially triggering further dynamic changes. Measurements of fjord circulation from several Greenland outlet glaciers (Straneo et al., 2010, 2012; Sutherland and Straneo, 2012) confirm that warm waters arriving at Greenland's continental shelf are able to circulate up towards glacier termini, providing an efficient heat exchange mechanism. Straneo et al., (2012) also showed that the distribution of glaciers which underwent rapid retreat was consistent with

patterns of fjord heat exchange.

Submarine melting can also act to promote calving at vertical calving fronts, by progressively undercutting the terminus (Fig. 2.4b). This effect is significantly amplified by forced convection, driven by the ejection from the base of the terminus of cold, fresh meltwater (Jenkins, 2011; Slater et al., 2015; Xu et al., 2013). This meltwater, produced either at the surface or the bed, and then routed through the subglacial hydrological system to the snout, rises rapidly through the denser seawater. Through turbulent mixing, this rapidly rising plume entrains warm seawater, forming a buoyant plume in contact with the front, and carrying significant energy for melting.

The effect of these proglacial plumes at Store Glacier has received significant attention. Direct observations carried out by Chauché, (2016) reveal in-plume melt rates up to $12\,\mathrm{m\,d^{-1}}$. Several previous studies have modelled these plumes (Cowton et al., 2015; Slater et al., 2015; Xu et al., 2012, 2013) using general circulation models of varying complexity. Model results indicate that both thermal forcing (changes in fjord water temperature) and rate of meltwater discharge can have a significant impact on melt rate. The implication of this is that both oceanic *and* atmospheric perturbations could affect melt rates.

Undercutting of a calving terminus by submarine melting may have a significant impact on the stress regime. Thus far, analysis of this process has been limited to steady-state analysis of idealised geometries (O'Leary and Christoffersen, 2013). Results suggest that undercutting may significantly amplify the size of calving events. However, without analysing this effect in a time-evolving calving model, theoretical understanding of the overall effect of undercutting is limited.

Ice Mélange Buttressing

In winter, the proglacial fjords of many of Greenland's outlet glaciers fill with ice mélange, a mixture of calved icebergs and sea ice (Howat et al., 2010; Walter et al., 2012). Studies on the rheology of ice mélange indicate that it may be able to provide significant buttressing force on the terminus of the calving glacier (Fig. 2.4c)(Amundson et al., 2010; Walter et al., 2012). Amundson et al., (2010) found that the ice mélange in Jakobshavn fjord is strong enough in winter to prevent the calving of full-thickness icebergs, resulting in advance. At Store Glacier, analysis

of force balance before and after the summer collapse of the mélange suggests that it provides a buttressing force of 45 kPa on the terminus, when present (Walter et al., 2012).

Section 2.2.3 demonstrated that the permanent force imbalance at the terminus means that there is a constant rotational torque, with a maximum outward force at the waterline (Fig. 2.2). Thus, ice mélange applies a buttressing force precisely at the location where it is best able to prevent calving, akin to stabilising a toppling bookcase by supporting it at the top. Previous modelling studies investigating the effect of ice mélange on calving have generally found that the buttressing effect of ice mélange was capable of suppressing calving sufficiently to promote terminus advance (Cook et al., 2014; Vieli and Nick, 2011), though Cook et al., (2014) suggested that the required buttressing force was unphysically high.

The formation and collapse of ice mélange is clearly linked to climate (Amundson et al., 2010; Howat et al., 2010; Walter et al., 2012), however the actual driver is unclear. It seems likely that change in ocean temperature is responsible for collapse, by submarine melting from below, but it is equally possible that increasing surface melt from warmer air temperatures weakens the mélange from above via hydrofracturing. Amundson et al., (2010) found that mélange velocity in front of Jakobshavn Isbræ increased significantly following large calving events, and so there may be nuanced feedback loops involved in the relationship between ice mélange strength and calving rate, such that a single environmental driver for seasonal mélange collapse does not exist.

Other Processes

Increasing subglacial water pressure towards the terminus of calving glaciers is responsible for the large scale longitudinal stretching which acts to open crevasses and promote calving (Section 2.2.2). It stands to reason, then, that changes in the hydrological system could result in changes to the near terminus stress regime and, thus, calving. However, while subglacial hydrological changes have been shown to affect the flow of ice in the interior of the Greenland Ice Sheet (Zwally et al., 2002) and, indeed, near the terminus of Store Glacier (Ahlstrøm et al., 2013), the impact of such changes on calving is unclear. Given that *longitudinal stretching* in the region near the terminus is responsible for opening crevasses and calving,

changes to subglacial hydrology will only promote calving if they increase this stretching. In other words, only a preferential acceleration in the lower reaches of the glacier would be expected to promote calving; if, on the other hand, the upstream region accelerated more than the near-terminus ice, the effect may be to *reduce* longitudinal stretching, and thus inhibit calving.

An additional hydrological effect arises from melting of the surface of the glacier. Meltwater entering surface crevasses can promote crevasse growth through hydrofracturing (Fig. 2.4). The force exerted by the water on the walls of the crevasse (Eq. 2.12) opposes the creep closure force, resulting in a net tensile stress to greater depths than for a dry crevasse. Hydrofracturing is believed to have triggered the 2002 collapse of the Larsen B Ice Shelf (Scambos et al., 2003), and the 2008 collapse of the Wilkins Ice Shelf (Scambos et al., 2009). Modelling studies using the crevasse depth calving law (Section 2.2.2) highlight the sensitivity of calving termini to changes in water depth (Cook et al., 2012; Nick et al., 2010; Vieli and Nick, 2011); however, the crevasse depth criterion explicitly includes water depth (Eq. 2.12), so this result may not be robust. Furthermore, it is extremely difficult to either measure or predict the depth of water in surface crevasses; the water depth depends not only on the supply of water from melting, but also the individual crevasse geometry, and the ability of water to drain either downward toward the bed or laterally off the glacier. It is, thus, currently impossible to constrain water depth in crevasses to even an order of magnitude.

2.2.5 Dynamic Response to Environmental Forcing

The previous section reviewed climate processes which may affect calving rate. Understanding these processes is important, as changes in these processes in a warming climate may trigger long term change at calving glaciers. However, predicting the long term response of calving glaciers to external environmental forcing requires an understanding of internal dynamic response to these triggers.

Observations from outlet glaciers in Greenland and Antarctica demonstrate that an initial retreat of the calving terminus often results in significant changes in ice flow far upstream. The rapid retreat of the 15km floating tongue of Jakobshavn Isbræ, West Greenland, was concurrent with the onset of acceleration and thinning which propagated upstream into the glacier's trunk (Joughin et al., 2008; Thomas et al., 2009). Modelling work suggests that the loss of the floating

tongue was responsible for a doubling of Jakobshavn's velocity near the terminus and consequent thinning (Vieli and Nick, 2011). Similarly, Nick et al., (2009) suggest that observed upstream changes at Helheim Glacier, East Greenland, were triggered at the terminus.

The propagation of acceleration and thinning upstream is attributed to the importance of longitudinal stress gradients in glacier force balance. In the case of Jakobshavn Isbræ, it has been suggested that the long floating tongue provided significant resistance to upstream flow, essentially buttressing the upstream ice (Joughin et al., 2014). The removal of this buttressing support following the retreat of the floating tongue therefore propagates a force imbalance upstream, in response to which the glacier accelerates and undergoes dynamic thinning. This mechanism is also proposed by Scambos et al., (2004) to explain the up to six-fold increase in velocity of glaciers flowing into the Larsen B Ice Shelf following its collapse in 2002.

Evidently, changes at the termini of calving glaciers can have a significant influence on the upstream dynamics, and initial climate perturbations are capable of triggering large, irreversible responses in these systems. However, observations over the past few decades have shown that calving glaciers within the same region do not necessarily respond consistently to the same external forcing (Howat et al., 2010). This observation suggests that *internal* characteristics may regulate the response of calving glaciers to external forcing, and thus their long-term stability.

Section 2.2.3 discussed the potential for small scale changes in glacier geometry to locally affect the stability of a calving terminus by influencing the stress regime. On larger spatial scales, topography and glacier geometry may also influence the stability of calving glaciers in response to changing climate (Schoof, 2007; Vieli et al., 2001). Vieli et al., (2001) used a full-Stokes flowline calving model to demonstrate that basal topography exerted a first-order control on calving rate; the model was found to retreat rapidly over retrograde bed slopes (i.e. ice flowing uphill), but was comparatively stable on normal down-sloping regions of the bed. This model result is supported by more recent mathematical analysis by Schoof, (2007), who proposed that a glacier grounding line cannot maintain a stable position on a retograde bed slope, a theory referred to as the Marine Ice Sheet Instability hypothesis (MISI). In Antarctica, Pine Island Glacier's grounding line is currently undergoing sustained retreat over a retrograde bed slope, and Favier et al., (2014) used several 3D models to infer that MISI is responsible. However,

the theoretical work of Schoof, (2007) considered a glacier flowline only, and Gudmundsson et al., (2012) suggest that changes in glacier or ice-stream width can mitigate MISI, suggesting that stable grounding line positions on retrograde bed slopes may be possible.

More generally, a glacier which retreats into an overdeepening of its trough will almost always increase its ice discharge into the sea; the loss of buttressing support from the downstream ice is analogous to the loss of Jakobshavn's floating tongue, or the collapse of the Larsen B Ice Shelf. The deeper calving front is exposed to the ice cliff force imbalance effect (Section 2.2.3) which increases extensional stress and causes acceleration at the terminus.

The observational and theoretical evidence outlined above suggests that glacier geometry and, particularly, basal topography exert an important control on the stability of calving glaciers. This is particularly significant given the recent discovery of a 750 km long 'mega-canyon' underneath much of the northern Greenland Ice Sheet, terminating under Petermann Gletscher (Bamber et al., 2013), as well as similar deeply incised features under many other Greenland outlet glaciers (Morlighem et al., 2014). The basal topography dataset produced as part of this study (Appendix A.2) reveals that Store Glacier flows through a 30km long trough overdeepening which reaches up to 900 m below sea level; this suggests that, were an initial retreat of the calving front to be triggered, it may undergo a sustained retreat through this trough.

2.3 Elmer/Ice

The 2D and 3D calving models presented in this study were developed using the Elmer/Ice glaciological model (`http://elmerice.elmerfem.org/`). Elmer/Ice encompasses a series of glaciological modules built into the open-source multi-physics package Elmer FEM, which is capable of solving a diverse range of partial differential equations (PDEs) using the Finite Element Method (FEM). The capabilities of Elmer/Ice include:

- Solution of full-Stokes flow and lower order approximations (SIA, SSA)
- Multiple flow laws: Glen's, Anisotropic, Firn Compaction
- Ice temperature including basal friction, strain heating and enthalpy

- Inverse methods (adjoint & Robin) for basal slip and ice viscosity
- Parallel PDE solvers and preconditioners
- Grounding line migration
- Ice damage advection
- Subglacial hydrology

The finite element method is one of many frameworks for the discretisation and solution of PDEs over complex domains. A key advantage of the finite element method is its flexibility with regards to the spatial scales on which the problems are solved. In contrast to finite difference schemes, which require a fixed resolution, FEM allows for variable spatial resolution and arbitrary element shapes. An explanation of the mathematics underlying FEM is far beyond the scope of this thesis; a thorough and accessible treatment can be found in Johnson, (1987).

The Finite Element Method (FEM), along with most methods for solving partial differential equations (PDE) in a continuum, requires that the domain of interest be discretised. This allows complex geometries to be approximated by a series of simple geometric 'elements', over which the PDE of interest can be more easily solved. The resulting spatial discretisation is called a mesh. For simple, idealised geometries, the process of 'meshing' is straight forward. A square or cube domain can be very easily split into equal sized elements of the required size. However, real world problems rarely take such simple shapes, and so meshing algorithms are required to produce meshes with desired characteristics for the given domain. In this study, the meshing software 'GMSH' (`http://gmsh.info/`) is used to generate meshes via Delaunay triangulation.

Due to the difficulty of measuring or observing the bed underneath glaciers and ice sheets, we are rarely able to accurately constrain basal boundary conditions when attempting to solve for the flow of ice. Such is the case for Store Glacier, and so this study makes extensive use of inverse methods to estimate basal conditions. Inverse methods allow us to use numerical models to 'work backwards' from observed surface velocity to an estimate for the slip parameter (β) at the bed. As mentioned above, Elmer/Ice includes modules for both the adjoint (MacAyeal, 1993; Morlighem et al., 2010) and the Robin (Arthern and Gudmundsson, 2010)

methods, both implemented in Elmer by Gillet-Chaulet et al., (2012). In this study, I use the adjoint method to constrain basal slip underneath the 2D (Section 3.5) and 3D models (Section 5.7).

CHAPTER 3

The 2D Model: Methods

This chapter and the next present the 2D calving model which was developed as a precursor to the significantly more complex 3D model. This work was published (Todd and Christoffersen, 2014) and the majority of the text from the next two chapters is taken directly from this publication. This chapter, which presents the methods of the 2D model, has been expanded and adapted somewhat from the publication, to take advantage of the less restrictive thesis format to delve deeper into some of the specifics of the methods. Chapter 4, which presents and discusses the results of the 2D model, is largely unmodified from the publication. The paper was written by J. Todd with guidance from P. Christoffersen. Bathymetric data used to constrain the subglacial topography near the terminus was provided by A. Hubbard.

The computational cost of 3D simulations means that it is often desirable to model physical systems in a reduced dimensional form. In particular, systems which have a particular dimension in which processes are either close to symmetric, or otherwise negligible, make good candidates for reduced dimension models. Whether outlet glaciers are such a system remains open for debate (Passalacqua et al., 2016). However, for this project, modelling calving in 2D represents a useful and manageable stepping stone to a full 3D model. Furthermore, modelling the same outlet glacier in 2D and 3D permits an assessment the suitability of reduced dimensional modelling for calving glaciers.

3.1 Model Domain & Mesh

In the case of an outlet glacier, the least important dimension is the transverse, or lateral, direction. For convenience, it is typical to define a cartesian coordinate system where x is the direction of flow, z the vertical, and y the neglected transverse direction. In the case of a perfectly straight glacier, these coordinate directions would be constant in real space. However, real glaciers twist and turn as their flow is directed by their underlying topography, and so instead a central 'flowline' must be identified. This flowline then defines the x coordinate at every point along the flow.

Figure 1.1 (p.9) shows the central flowline for Store Glacier, as determined from velocity maps from InSAR satellite data. I choose to follow this flowline 113km inland to the $100\,\mathrm{m\,a^{-1}}$ velocity contour. Figure 3.1a shows the surface and elevation profiles along this flowline, as calculated using the mass conservation method outlined in Appendix A.2.

I define four boundaries on the model domain. The inflow boundary (Γ_{inflow}), which is the upstream limit of the flowline, the calving terminus (Γ_{term}), the upper surface of the ice (Γ_{surf}), and the base of the ice (Γ_{base}) which is synonymous with the bed, except when flotation occurs.

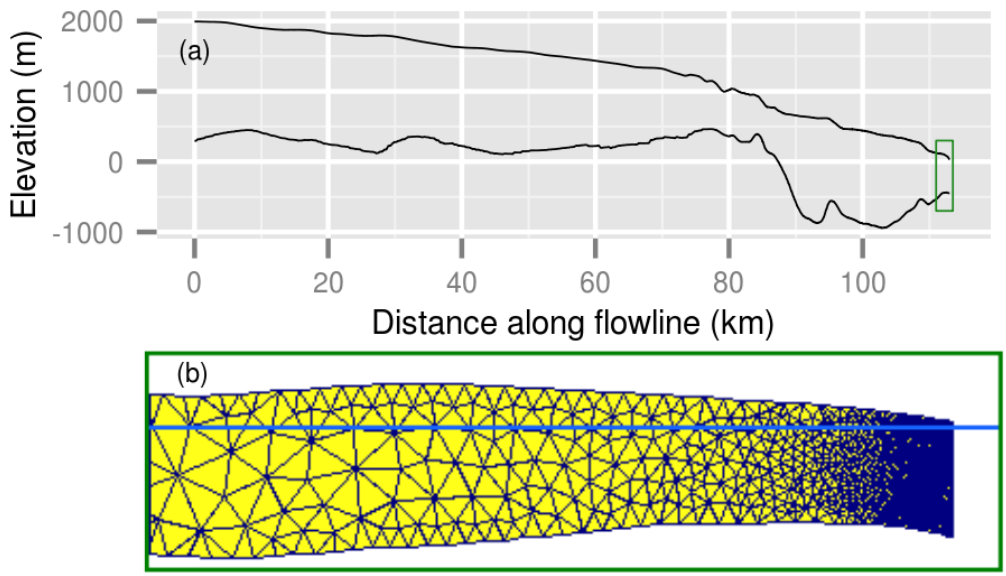

Figure 3.1: (a) Store Glacier central flowline surface and bed elevation. Green box indicates extent of (b). (b) Flowline model mesh, showing increasing resolution towards terminus.

3.2 Ice Dynamics

At each timestep of the 2D calving simulation, the flow solution is solved using the Elmer/Ice solver `FlowSolve`. The flow field (velocity and pressure) is the solution to the Stokes equations (Eqs. 2.1, 2.2), subject to the following boundary conditions.

The upper ice surface is stress free:

$$\boldsymbol{\sigma}_{\perp} = \mathbf{0} \qquad \text{on } \Gamma_{surf} \tag{3.1}$$

where $\boldsymbol{\sigma}_{\perp} = \boldsymbol{\sigma} \cdot \boldsymbol{n}$ is the stress vector normal to the surface. The bottom surface of the ice is, for the most part, in contact with bedrock (i.e. grounded), and so there can be no velocity normal to this surface (Eq. 3.2). However, when the ice is floating, I instead apply external pressure from basal water pressure (Eq. 3.3).

Basal water pressure is, in reality, dictated by the glacier's hydrological system, both the supply of water (supraglacial hydrology) and its routing and storage

(subglacial hydrology). However, attempting to couple these hydrological models to ice flow is beyond the scope of this study. Furthermore, in 2D it is theoretically unjustifiable to attempt to model subglacial hydrology, given that the basal boundary condition is a line, rather than a surface.

In the absence of a hydrology model, it is difficult to predict the basal water pressure. However, note that this external pressure condition is only important where ice may approach flotation, and this is only likely to occur near the terminus. I further note that, given that subglacial water flows *out* towards the fjord, sea level dictates a lower bound on the water pressure in this region. Assuming that the hydrological system near the terminus allows a free and easy connection to the fjord, then it is a reasonable approximation to say that the water pressure here is equal to that exerted by sea level. Thus, I have:

$$u_\perp = 0 \qquad \text{on } \Gamma_{base} \text{ if grounded} \tag{3.2}$$

$$\sigma_\perp = \rho_w g(z - z_{sl}) \qquad \text{on } \Gamma_{base} \text{ if floating} \tag{3.3}$$

where $z_{sl} = 0$ is sea level, $u_\perp = \boldsymbol{u} \cdot \boldsymbol{n}$ is normal velocity, and $\sigma_\perp = ||\boldsymbol{\sigma}_\perp||$ is the norm of the normal stress vector.

I also require a condition for basal friction which controls the rate of sliding. As discussed in Section 3.5, I use inverse methods to constrain the properties of the bed. The result of these inverse simulations is a slip coefficient (β), such that:

$$\sigma_\parallel = \begin{cases} -u_\parallel \beta & \text{if grounded} \\ 0 & \text{if floating} \end{cases} \qquad \text{on } \Gamma_{base} \tag{3.4}$$

where $\sigma_\parallel = ||\boldsymbol{\sigma} \cdot \boldsymbol{n} - \sigma_\perp \boldsymbol{n}||$ is the norm of tangential stress, and $u_\parallel = ||\boldsymbol{u}_\perp \boldsymbol{n}||$ is the tangential velocity. Basal friction disappears when the ice reaches flotation. As discussed in Section 3.5, I invert for β using both summer and winter observed velocity, giving a separate β profile for each. I vary the value of β sinusoidally between these two values through the year, in order to simulate seasonal dynamics.

At the terminus, I apply external pressure from the sea, where the ice is below sea-level. Above sea-level, no stress is applied. This can be expressed concisely

as:

$$\sigma_\perp = \min(-\rho_w g(z - z_{sl}), 0) \qquad \text{on } \Gamma_{term} \tag{3.5}$$

Finally, on the inflow boundary, instead of prescribing a fixed velocity profile, I apply an external pressure, tuned to match observed surface inflow velocity (100 mpy). I do this as opposed to imposing a fixed velocity because the latter leads to instability in the free surface solver. The inflow boundary condition is:

$$\sigma_\perp = -0.965\rho_i g d \qquad \text{on } \Gamma_{inflow} \tag{3.6}$$

$$\tag{3.7}$$

where d is depth.

The Arrhenius factor of Glen's flow law (Eq. 2.3, p.16) is highly temperature dependent. However, solving for the velocity and temperature together is computationally expensive; because the equations are coupled, solving them requires iterating the two solvers at each timestep until convergence is reached. Furthermore, an investigation by Passalacqua et al., (2016) into the applicability of 2D flowline models to represent 3D glacier domains with significant changes in width found that large errors arose when variable temperature was imposed. For these reasons, in the 2D simulations, I consider the glacier to be isothermal at $-10\,°\text{C}$.

3.3 Accounting for Lateral Variability

Modelling a calving glacier in two dimensions has obvious advantages: the computing power required to solve the various partial differential equations is orders of magnitude less, and implementing a calving criterion is significantly less difficult. However, glaciers are three dimensional systems, and variability in their third dimension often results in behaviour which cannot be ignored if the system is to be modelled with any accuracy.

In the context of a 2D flowline model, the neglected third dimension is transverse to flow. There are primarily two processes which act in this transverse direction which must be accounted for. These are lateral drag, the resistive force from the sides of the glacier, and flow convergence, the 'addition' of ice into the flowline when the glacier converges downstream. Figure 1.1 shows the width of

Store Glacier's catchment, which reduces from 40 km at the inflow boundary to 5 km at the terminus.

3.3.1 Lateral Drag

Elmer/Ice includes a function (`USF_LateralFriction`) to account for varying lateral drag, developed by Gagliardini et al., (2010). It works by adding an additional force vector ($\boldsymbol{f}$) to the Stokes equation for momentum balance (Eq. 2.1):

$$\nabla \cdot \boldsymbol{\sigma} + \rho \boldsymbol{g} + \boldsymbol{f} = 0 \tag{3.8}$$

defined by:

$$\boldsymbol{f} = -K|\boldsymbol{u}|^{m_{lr}-1}\boldsymbol{u} \tag{3.9}$$

$$K = \frac{(n+1)^{1/n}}{W^{\frac{n+1}{n}}(2A)^{1/n}} \tag{3.10}$$

where A is the Arrhenius factor (or "rate factor"), W is the glacier half-width, n is as in Glen's flow law (Eq. 2.3), and $m_{lr} = 1/n$. The derivation of this lateral drag term, $\boldsymbol{f}$, is presented in the supplementary material of Gagliardini et al., (2010).

3.3.2 Flow Convergence

In addition to affecting lateral drag, the convergence of flow from Store's accumulation zone towards its terminus results in a large amount of additional mass which must be accounted for. Previous flowline modelling studies have attempted to account for lateral convergence by adding a surface mass balance term (Cook et al., 2014; Gladstone et al., 2012). However, this approach is unable to account for the direct effect on the velocity field which out-of-plane ice convergence has on flowline velocities. For this reason, I implement a new scheme to directly modify the Stokes equations.

Recalling the Stokes equation for mass conservation in an incompressible fluid

(Eq. 2.2):

$$\nabla \cdot \boldsymbol{u} = 0 \tag{3.11}$$

I note that the mass of any arbitrary fixed volume (or area, in 2D) of the model must remain constant. This is analogous to the concept of 'flux gates' on a glacier; in the absence of accumulation/melting, the flux through two vertical gates along the flowline model must be equal. However, when flow is converging or diverging in the missing transverse dimension, this is no longer the case, and Equation 3.11 no longer holds. Instead, an artificial flux term appears, and Equation 3.11 becomes:

$$\nabla \cdot \boldsymbol{u} = -\frac{dW}{dx} W^{-1} u_x A_{elem} \tag{3.12}$$

where W is the half-width of the glacier, and A_{elem} is the area of the mesh element in question.

By directly modifying the Stokes equations as outlined, I ensure that the addition of mass by convergence, and its effect on the velocity field, are properly taken into account. The width of Store's catchment varies from around 40 km at the inflow boundary of the flowline, to around 5 km at the terminus. Thus, neglecting to account for flow convergence would result in almost 90% of the mass at the terminus being neglected. A more thorough investigation of this method, presented in Passalacqua et al., (2016), shows that the Stokes equation for momentum balance should also be modified, but testing revealed that the difference in results was small.

3.4 Surface Evolution & Mass Balance

In a time-evolving simulation, glacier geometry evolves as a result of imposed changes to ice flow boundary conditions and changes at the calving front (Section 3.6). As such, changes in surface and basal elevation must be solved for at each time step. Changes in the height (h) of a surface of a body undergoing flow and

accumulation are described by the free surface equation:

$$\frac{\partial h}{\partial t} = u_z + \left[1 + \left(\frac{\partial h}{\partial x}\right)^2\right]^{1/2} a_\perp - u_x \frac{\partial h}{\partial x} \tag{3.13}$$

where $a_\perp$ is the normal accumulation, representing surface mass balance on the surface, and melt on the base.

The first term on the right of Equation 3.13 is the vertical velocity. The second is the accumulation term, accounting for the fact that the surface is not likely to be perfectly horizontal. The third term represents the advection of surface features downstream as the glacier flows.

The free surface equation is implemented in Elmer through the `FreeSurface` solver. In the case of the basal ice surface, the free surface equation is limited; ice is unable to fall below the bedrock elevation. `FreeSurface` takes care of this limit by reading the bedrock elevation from the model description, and applying the appropriate Dirichlet boundary condition.

To account for surface mass balance (SMB), I use data from the RACMO 2.0 climate model (Lenderink et al., 2003). Monthly SMB maps for Store's domain for the period 1985 to 2008 were reduced to a representative mean annual map, and a profile for the central flowline was then extracted to provide the accumulation term in Equation 3.13.

At each time step, I must also account for the fact that the calving front advances into the fjord. I impose that the terminus advances at the velocity of the slowest node. Thus, if no frontal melting is imposed, the front remains vertical. The implementation of submarine melting of the terminus is described in Section 3.7.1.

3.4.1 Mesh Evolution

The free surface implementation described above predicts the change in height of the upper and lower ice surfaces. In order to implement this evolution, it is also necessary to predict the deviation of the mesh's internal nodes. This is an elasticity problem, and is implemented in Elmer using the `MeshUpdate` solver.

The solution of the free surface equation and the implementation of terminus advance provide the boundary conditions for the mesh evolution problem. Thus, the boundary conditions on the mesh displacement ($\boldsymbol{d}$) are:

$$d_z = z + \frac{dh}{dt}dt \qquad \text{on } \Gamma_{base}, \Gamma_{surf} \tag{3.14}$$

$$d_x = x + U_{x_{min}}dt + \text{melt} \qquad \text{on } \Gamma_{term} \tag{3.15}$$

$$\boldsymbol{d} = 0 \qquad \text{on } \Gamma_{inflow} \tag{3.16}$$

where $\frac{dh}{dt}$ is the change in the upper or lower ice surface height as computed by `FreeSurface` (Section 3.4), and $U_{x_{min}}$ is the minimum horizontal velocity at the calving front.

3.5 Inversion & Spin-Up

Basal friction exerts a first-order control on the velocity of outlet glaciers. Lack of detailed knowledge about basal conditions under Store Glacier, or indeed, most of the Greenland Ice Sheet, mean that it is practical to use inverse methods to constrain changes in basal slip from observed variations in surface velocity. I use the adjoint method (MacAyeal, 1993; Morlighem et al., 2010), implemented in Elmer/Ice by Gillet-Chaulet et al., (2012), to generate estimates of summer and winter basal slip coefficient, β. Velocity profiles from June and November 2009 (Fig. 3.2) were obtained from the MEaSUREs velocity dataset (Joughin et al., 2011), and these profiles were used to estimate summer and winter β profiles. I impose seasonally variable velocity by varying β sinusoidally between the summer and velocity end-member profiles. This allows us to investigate the effect of seasonal changes in velocity on calving rate.

Due to inaccuracies in surface and bed DEMs, boundary conditions and material parameters, the start of any time-evolving glacier dynamic simulation is usually characterised by rapid surface adjustment and changes in ice flow dynamics. In essence, the model's initial conditions are not in a steady state, and so the model immediately adjusts towards this steady state. For this reason, it is necessary to 'spin up' the model before attempting to investigate the effect of imposed perturbations.

After running the inverse simulations for both observed summer and winter velocity, I spin up the model by running it forward in time, varying β sinusoidally between the summer and winter β profiles. I run this spin up for 200 years

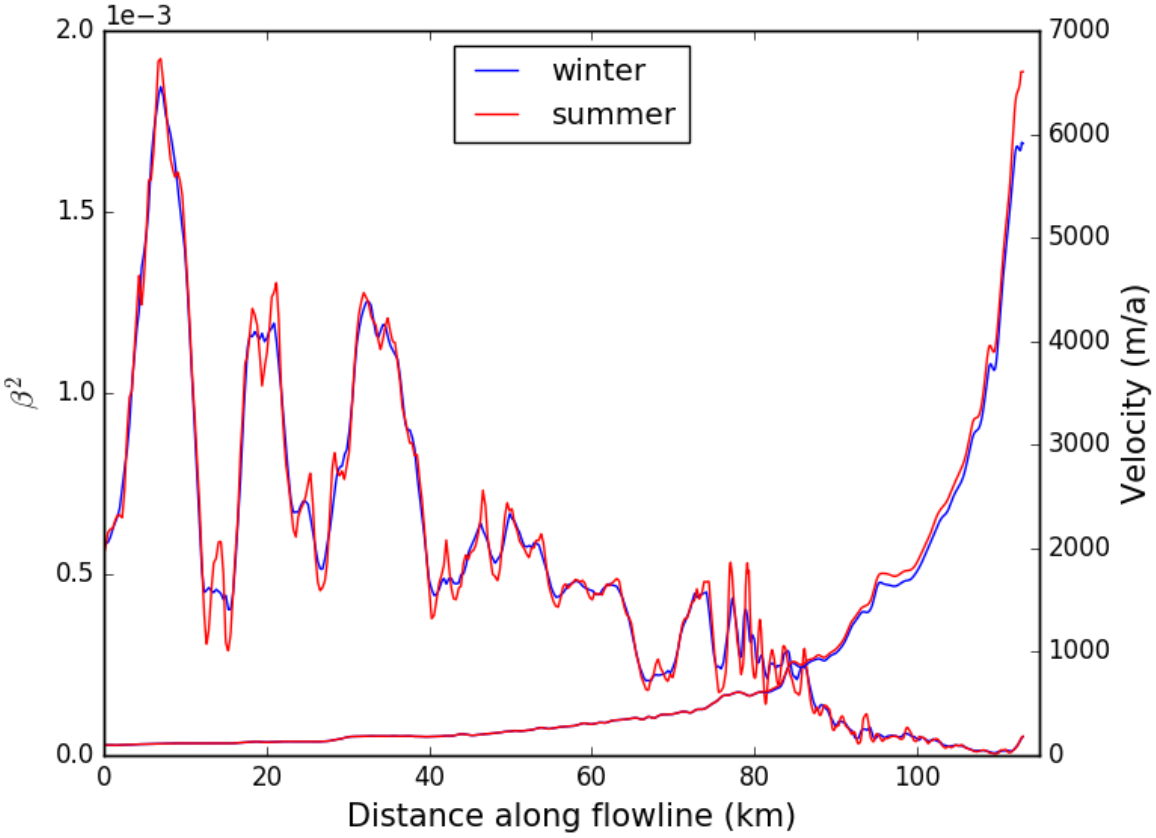

Figure 3.2: Summer (red) and winter (blue) velocity and β^2 profiles along the flowline of the model domain. The velocity profiles are identical up to the 75 km mark, because seasonal velocity was not available upstream of this point. Seasonal range gradually increases from zero at 75 km to 690 m a^{-1} at the terminus.

simulation time, with a fixed terminus position, to ensure that a steady state is reached before attempting to predict calving and apply climate perturbations.

3.6 Modelling Calving in 2D - `Calving.F90`

I use the physically based *crevasse depth model* (Section 2.2.2) to predict calving. Following Nick et al., (2010), I state that calving occurs when *surface and basal crevasses meet*. I use a modified version of the Nye, (1957) criterion to account fully for extensive stress, as opposed to simply the horizontal component, and define a 'net stress' (σ_{net}), for both surface and basal crevasses, which is positive

in an open crevasse field and negative otherwise:

$$\sigma_{net_{surf}} = 2\tau_E \text{sgn}(\tau_{xx}) - \rho_i g d \tag{3.17}$$

$$\sigma_{net_{basal}} = 2\tau_E \text{sgn}(\tau_{xx}) - \rho_i g d + P_w \tag{3.18}$$

where τ_E is effective deviatoric stress, and τ_{xx} is deviatoric stress in the x direction.

The first term on the right represents the tensile deviatoric stress which acts to open crevasses. In previous work implementing the 2D crevasse criterion (Benn et al., 2007a,b; Nick et al., 2010), this term was $2\tau_{xx}$ only. Following the work of Otero et al., (2010), I replace this with an effective stress term to account for stress contributions out of the horizontal plane; in other words, crevasses may open in response to extensional stresses which are not perfectly horizontal. The signum function of τ_{xx} ensures that crevasse opening is only predicted when the most extensional deviatoric stress is predominantly horizontal (i.e. crevasses do not open in response to vertical extensional stress). Note that in 2D, effective deviatoric stress is equal to the first principal stress (Appendix A.1), and so the 2D calving criterion essentially compares the largest principal deviatoric stress, acting to open crevasses, with the ice overburden acting to close them.

The second is the overburden pressure (the weight of the ice), which acts to close the crevasse through creep. The third term in Equation 3.18 is water pressure in basal crevasses, which counteracts the creep closure term, permitting basal crevasses at depths where, in the absence of water, high overburden pressure would prevent dry crevasses.

As discussed in Section 3.2, I do not attempt to model the subglacial hydrological system. Instead, I consider that the basal water pressure near the terminus is dictated by sea level, and so:

$$P_w = -\rho_w g z \tag{3.19}$$

Note that $\sigma_{net_{surf}}$ and $\sigma_{net_{basal}}$ are essentially equivalent, given that P_w is zero for surface crevasses. However, they are defined separately by `Calving.F90`, to allow for distinction between the surface and basal crevasse fields.

Figure 3.3 shows a typical net stress field for the terminus of the flowline model for Store Glacier, marked with a white contour illustrating the edge of

the surface and basal crevasse fields. Calving occurs when the surface and basal contours overlap.

The algorithm for detecting calving in 2D is as follows:

- Calculate net stress (σ_{net}) (Eqs. 3.17 & 3.18) values for every node in the domain.
- Identify connected groups of nodes where $\sigma_{net_{surf}} > 0$, mark `surf`
- Identify connected groups of non-`surf` nodes where $\sigma_{net_{basal}} > 0$, mark `basal`
- Look for adjacent `surf` and `basal` nodes, and interpolate to find the $\sigma_{net_{surf}} = 0$ and $\sigma_{net_{basal}} = 0$ contours.
- If any contours overlap, calving occurs at the furthest inland occurrence.

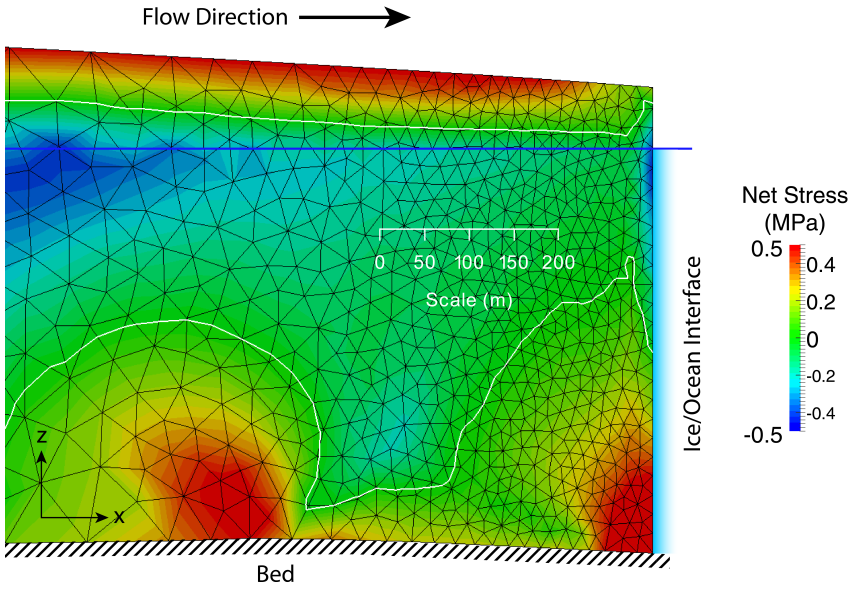

Figure 3.3: Net Stress field at the terminus of Store Glacier. White line shows Net Stress = 0 contour. Where Net Stress > 0, open crevasses exist. Blue line indicates sea level.

Crevasse penetration is assumed to occur vertically, and so a calving event in the 2D model is defined by an x-coordinate. In reality, non-vertical calving can occur; small, lamellar events are observed to fall from the terminus of Store

Glacier. However, these small events are unlikely to have a significant impact on the stress field, and their mass loss contribution is included in subsequent, larger events.

Tuning

The crevasse depth model is physically based and, unlike the water depth or height above buoyancy models (Section 2.2.1), there is no free parameter requiring calibration. However, I found that in the 2D model, Equations 3.17 & 3.18 failed to predict calving for Store Glacier; instead, the glacier advanced a floating tongue which continued without limit.

To account for the apparent underestimation of crevasse penetration in the 2D model, I apply a tuning factor of 1.075 to the principal deviatoric stress term (τ_1) in Equations 3.17 & 3.18. There are several potential reasons for unmodified 2D crevasse depth model to underpredict crevasse penetration, and these are discussed in Section 4.2.1.

3.7 Links to Climate

I use the 2D calving model presented in this chapter to investigate the effect of various climate forcings on the calving rate, flow dynamics and resultant terminus position. I chose to investigate 3 seasonally variable processes: basal slip, submarine melting and ice mélange buttressing. Seasonally varying basal slip is implemented as described in Section 3.5, and the implementation of submarine melting and ice mélange buttressing is described below.

Investigations into the effect of climatic processes was split into two experiments. In Experiment 1, I implement climatic processes using best estimates of the *current climate setting* of Store Glacier. The aim of Experiment 1 is primarily to assess the extent to which the different processes effect the seasonal behaviour presently observed at Store. However, Experiment 1 also permits us to assess the model's fidelity by comparing modelled and observed behaviour. In Experiment 2, I perturb the climate forcings applied in Experiment 1, in order to assess how Store Glacier might react to future climate change.

I chose not to investigate the hydrofracturing effect of meltwater in surface crevasses, though previous studies suggest this may be important (Cook et al.,

2012; Nick et al., 2010; Vieli and Nick, 2011) (Section 2.2.2). I chose not to investigate this process because my aim is to model processes realistically, using real values from data and modelling. There are no estimates for the depth of water in crevasses at Store Glacier, and without knowing crevasse geometry and connectivity to the bed, it is not possible to obtain even an order of magnitude estimate. Furthermore, previous studies using the crevasse depth model (Cook et al., 2012; Nick et al., 2010; Vieli and Nick, 2011) all prescribe quantities water in surface crevasses which are not informed by measurement or theory; instead, the water level is essentially a tuning parameter. I choose, instead, to directly apply a fixed tuning parameter (Section 3.6).

3.7.1 Submarine Melting

Undercutting of the calving face by submarine melting of the front is hypothesised to be an important process linking calving to changes in climate (Section 2.2.4). I investigate the effect of this process on Store Glacier by applying a depth dependent melt term to the advance of the terminus (Eq. 3.15).

Store's central flowline is close to the centre of the largest persistent plume observed by Chauché et al., (2014). As such, I seek to apply melt rates which are consistent with the centre of a buoyant plume. Xu et al., (2013) modelled plume melting at Store Glacier, finding an average frontal melt rate of $3.6\,\mathrm{m\,d^{-1}}$. Melt rate was found to vary from close to zero at the surface to $8\,\mathrm{m\,d^{-1}}$ near the base.

In Experiment 1, I approximate this result with a linear melt profile, varying from $0\,\mathrm{m\,d^{-1}}$ at sea level to $8\,\mathrm{m\,d^{-1}}$ at the base of the terminus. Because subglacial discharge is strongly influenced by surface runoff in summer months, I assume, for the sake of simplicity, that no submarine melting occurs in winter. In Experiment 2, I investigate the model's sensitivity to an increase in melt rates by factors of 1.5 and 2, and increases in melt season length of 33% and 66%.

3.7.2 Ice Mélange Buttressing

Ice mélange is the frozen matrix of icebergs and sea-ice often found in Greenlandic fjords during the winter months. As discussed in Section 2.2.4, it is hypothesised to provide a buttressing force against the termini of marine outlet glaciers. The presence of ice mélange at Store Glacier is well documented (Section 1.3). Indirect

estimates of the buttressing strength of Store's ice mélange suggest a force of 30-60 kPa (Walter et al., 2012). Laser altimeter data by NASA's Operation IceBridge (`https://espo.nasa.gov/missions/oib/`) reveals an average thickness of 75m.

For the applied force, I take the midpoint of the estimate of Walter et al., (2012), 45 kPa, and apply it over the observed 75m thickness. I apply the buttressing as a pressure boundary condition on the flow solution. However, the estimate of Walter et al., (2012) comes from glacier force balance analysis, and so the cited figure is, in fact, the stress as if it were applied across the *entire thickness* of the terminus. Thus, in order to arrive at a *per metre of mélange* value, I apply the following formula:

$$\sigma_{IM} = \sigma_{fb} \frac{H_{term}}{H_{IM}} \tag{3.20}$$

where σ_{IM} and σ_{fb} are the ice mélange and force balance stresses, respectively, and H_{term} and H_{IM} the thicknesses of the terminus and ice mélange. For an average terminus thickness of 470 m and a mélange thickness of 75 m, this results in a mélange buttressing stress of 282 kPa. In Experiment 1, I apply this buttressing stress from the beginning of February to the end of May. In Experiment 2, I investigate the effect of reducing mélange strength by 25% and 50%, and reducing the duration by 33% and 66%.

CHAPTER 4

THE 2D MODEL: RESULTS & DISCUSSION

4.1 Results

4.1.1 Experiment 1

Experiment 1 focuses on reproducing the present day seasonal forcing at Store Glacier's calving terminus. The 'baseline' model setup includes seasonally variable basal slip parameter (β). As expected, seasonally variable β results in a velocity fluctuation at the terminus, from a minimum of $4700\,\mathrm{m\,a^{-1}}$ to a maximum of $4900\,\mathrm{m\,a^{-1}}$ (Fig. 4.1b, blue line).

The calving behaviour of this baseline setup is characterised by the break off of a 80-90 m iceberg every 8.7 days (Fig. 4.1a, blue line). Calving events lead to instantaneous acceleration of the terminus, followed by subsequent deceleration as the terminus readvances. The magnitude of this calving driven velocity fluctuation ($200\,\mathrm{m\,a^{-1}}$) is similar to the total seasonal variability, indicating that terminus geometry is an important control on velocity.

The seasonal velocity fluctuation imposed via β does not result in any seasonal trend in terminus position; the calving behaviour remains constant throughout the year. This suggests that varying basal slip conditions are unlikely to be responsible for the observed seasonality of Store Glacier's terminus.

Submarine melting is imposed from June to August at a maximum rate of $8\,\mathrm{m\,d^{-1}}$ (Fig. 4.1, red lines). There is little response from the terminus to the applied melt rate. Calving events become slightly smaller and more frequent, but the overall terminus position is unaffected. Terminus velocity is slightly reduced during the melt season, compared to the baseline run. The apparent insensitivity

of the terminus to present day melt rates suggests that submarine melting is unlikely to be responsible for observed seasonality.

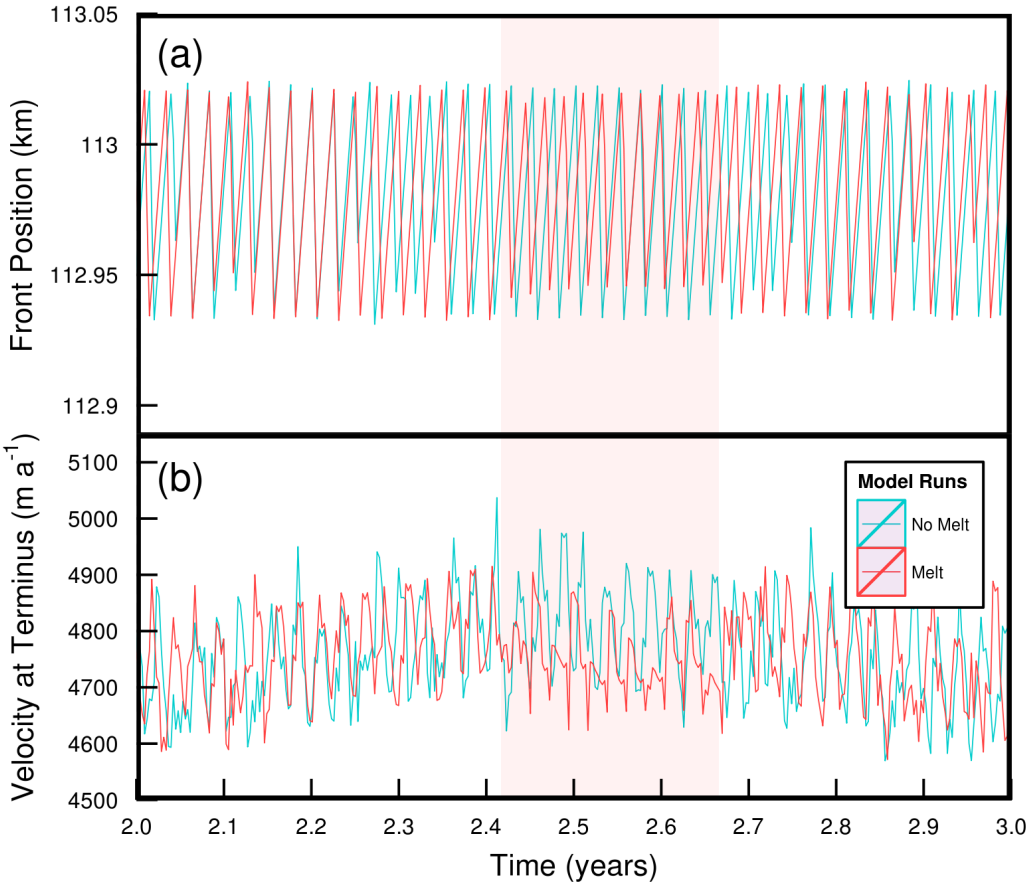

Figure 4.1: Variations in terminus position (a) and velocity (b) over a 1-year period for the control run (blue line) and with submarine melting applied (red line). The red shaded region indicates the melt season, when melting is applied at a maximum of $8\,\mathrm{m\,d^{-1}}$. Observed saw-tooth fluctuations coincide with calving events.

In the 2D model, only the stabilising effect of ice mélange buttressing was able to exert a significant seasonal influence on terminus position. This is illustrated by Figure 4.2, which shows terminus position and velocity for all 4 permutations of ice mélange and submarine melt forcing. When ice mélange buttressing is applied, the terminus immediately begins to advance into the fjord, and this advance is sustained at a constant rate throughout the mélange season (Feb - May, Fig. 4.2, blue shading), reaching a total advance of 1300 m before rapidly retreating once the ice mélange is removed. The retreat of the terminus occurs irrespective of

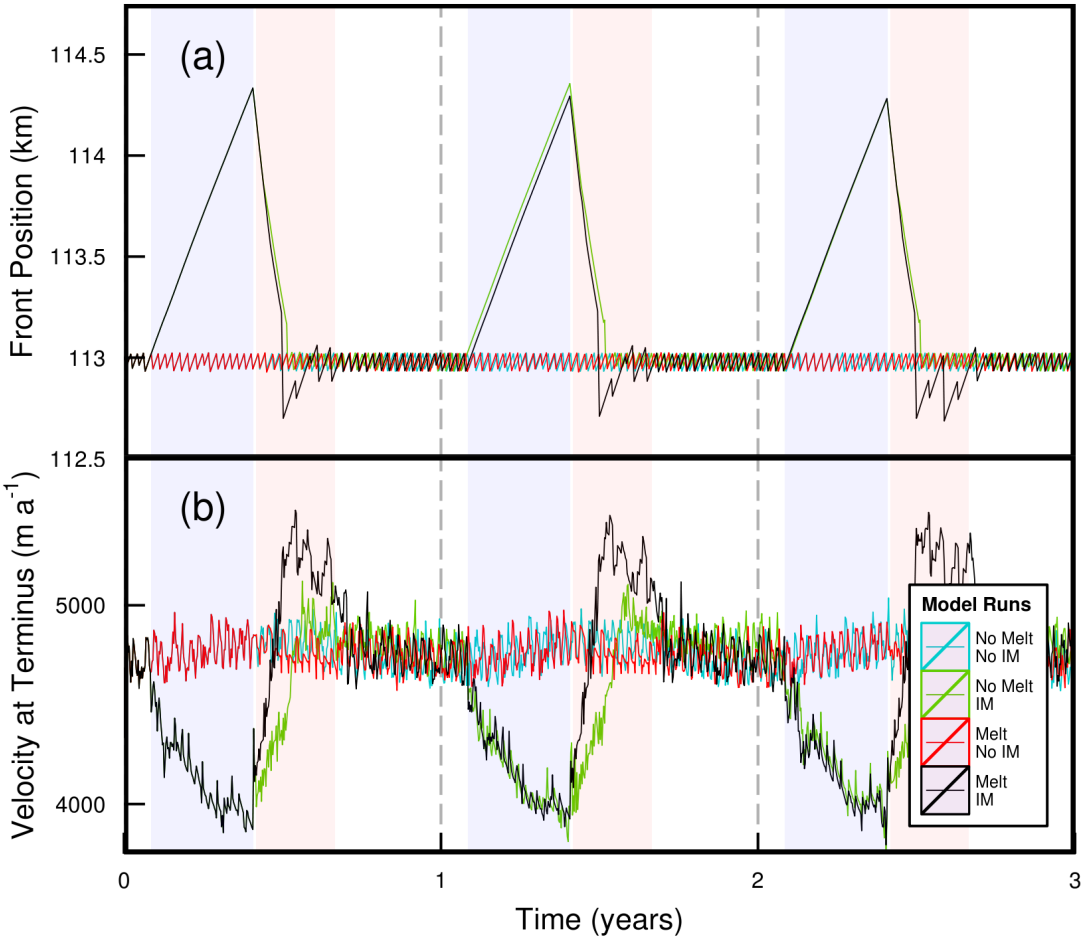

Figure 4.2: Terminus position (a) and velocity (b) fluctuation for the 4 permutations of melt and ice mélange. Blue and red shading indicate mélange and melt seasons respectively. Melting is applied at a maximum of $8\,\mathrm{m\,d^{-1}}$, and mélange buttressing at 45 kPa. Concurrent advance and deceleration occur as soon as mélange buttressing is applied.

submarine melting, although when melting is imposed, the terminus retreats a further 250 m, before returning to its stable position at 113 km.

Figure 4.3 shows a time series of terminus geometries during a period of ice mélange driven advance, with the upper and lower limits of basal and surface crevasse fields delineated by dashed lines. Note that the mélange causes the glacier to advance a floating tongue into the fjord.

As the floating tongue advances, both the surface and basal crevasse field become progressively shallower, despite the constant mélange buttressing force, suggesting that, to an extent, the floating tongue is a self-stabilising feature. Interestingly, the basal crevasse field near the grounding line remains fairly con-

stant, and there is no seasonal trend. This suggests that the loss of basal traction at this point is a significant potential source of calving instability.

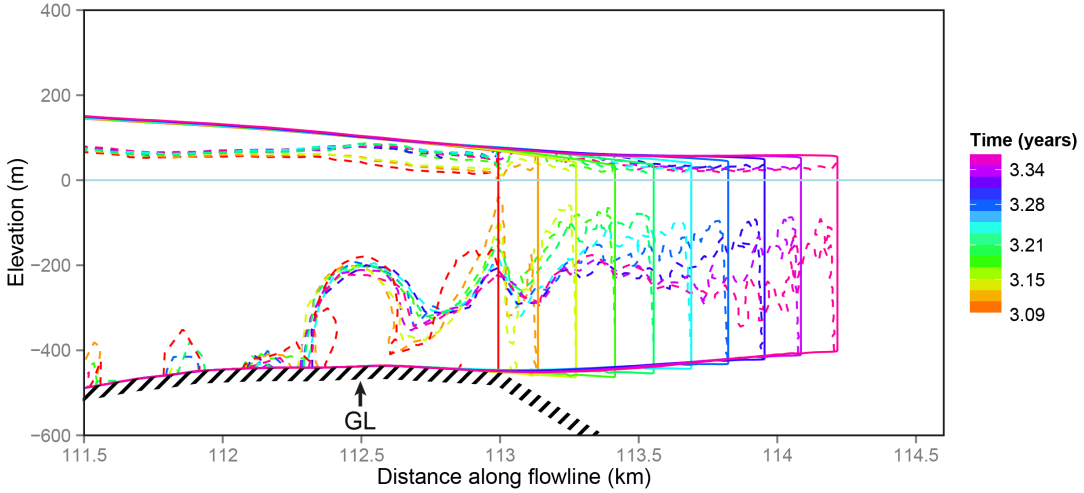

Figure 4.3: Terminus geometry and crevasse depth for successive timesteps during the ice mélange driven advance. 'GL' marks the location of the grounding line. As the floating tongue advances, it is forced upward by buoyant forces.

The result of Experiment 1 reveal a strong relationship between velocity and terminus position. As the terminus advances due to ice mélange buttressing, the velocity is significantly reduced (Fig. 4.2b), and a subsequent acceleration accompanies the retreat. This velocity perturbation dwarfs the seasonal signal imposed by varying basal friction. Figure 4.4a shows that this velocity signal is not limited to the terminus; the deceleration which accompanies the ice mélange driven advance is transmitted more than 30 km upstream, as is the subsequent acceleration.

The deceleration of the final 30 km of the glacier results in dynamic thickening over this region (Fig. 4.4b), followed by dynamic thinning during the terminus retreat, bringing the thickness near the terminus back to its January 1st value. Interestingly, at around 85 km, the velocity is consistently above the January 1st value throughout the year, suggesting that there maybe some lag in the dynamic coupling.

The outcome of Experiment 1 is a stable and seasonally variable calving model of Store Glacier, forced with present day climate perturbations. The results are in good overall agreement with observations (Howat et al., 2010; Walter et al., 2012). The stable terminus position at 113 km matches the observed summer terminus position. Furthermore, the total seasonal range in terminus position

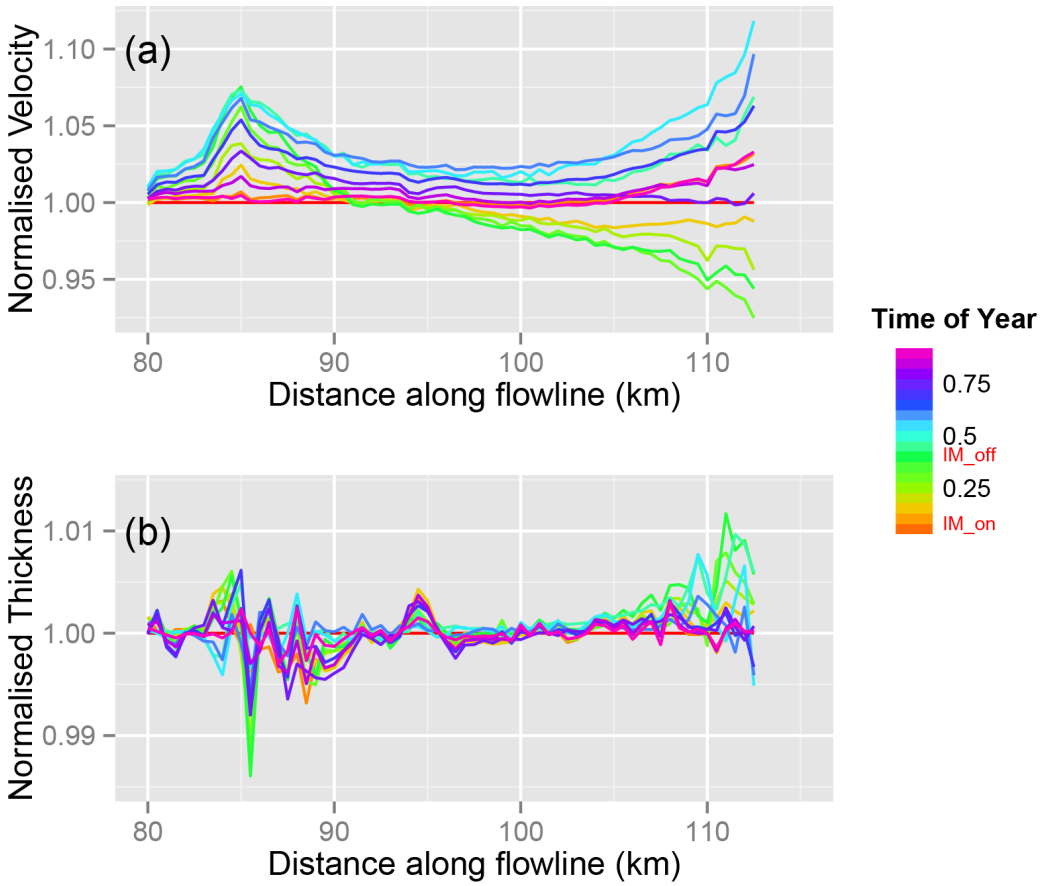

Figure 4.4: Velocity (a) and thickness (b) of the last ∼35km of the terminus through 1 year. Perturbations at the terminus are felt up to 30km upstream.

(1.3 km) is in good agreement with time-lapse imagery collected by the Extreme Ice Survey (`www.eis.com`), showing a variability of terminus position greater than 1 km (J. Box Personal Communication).

4.1.2 Experiment 2

In Experiment 2, I test the sensitivity of Store Glacier to perturbations to present day climate forcing, for both ice mélange and submarine melting. I perturb the magnitude and duration of these climate forcings in the 'direction' of a warming climate. In other words, I increase submarine melt magnitude and duration, but decrease ice mélange buttressing force and duration.

Figure 4.5 shows the change in terminus position in response to all combi-

nations of perturbation. Each individual panel represents a different duration, while each line within the panel represents different magnitude. Left panels ((a) and (d)) represent present day duration, while blue lines represent present day magnitude.

When ice mélange buttressing force is reduced by 25%, (Fig. 4.5a, green line) the floating tongue does not advance until half way through the melt season, though the front does advance slightly before this time. The final length of the tongue is reduced from 1.3 km to 0.7 km. When the mélange buttressing force is reduced by 50% to 22.5 kPa, (red line) no floating tongue forms. These results suggest that future climate driven reduction in ice mélange thickness may affect Store's seasonal advance and retreat.

Reducing the duration of the mélange season to 66 % (Fig. 4.5b) limits the length of the floating tongue to 0.8 km for the 45 kPa case. However, reduction to 33 % (Fig. 4.5c) has no further effect on calving dynamics, and the floating tongue continues to advance for a month following mélange break-up. This is a surprising result, which suggests that the floating tongue is at least temporarily self-stabilising. In the 75 % mélange strength case, when season duration is reduced to 66 % (Fig. 4.5b, green line), the floating tongue begins to advance slightly sooner and thus the final length is slightly higher. However, no floating tongue forms when season duration is further reduced to 33 % (Fig. 4.5c, green line).

An increase in the duration of submarine melting, by 33 and 66 % (Fig. 4.5e and f, respectively), leads to more rapid collapse of the floating tongue, though in no case does the tongue collapse while rigid mélange is still present. As in Experiment 1 (Fig. 4.2), submarine melting has an appreciable effect on the calving dynamics of the grounded terminus in late summer. As such, a longer submarine melt season leads to a longer period of larger, less frequent calving events and a retreat in average terminus position. The response of the modelled terminus to increasing melt magnitude, on the other hand, appears somewhat stochastic. It should be noted, however, that the positions shown in Figs. 4.1, 4.2 and 4.5 represent the terminus at the surface, which is able to advance into the fjord when undercutting takes place, due to the fact that the glacier's topography exerts a control on the position of the grounding line. Broadly speaking, the calving dynamics are, according to this model, relatively unaffected by increasing melt magnitude over the timescales investigated. In

even the most severe "warming climate" scenario, with melt rate double that of present-day values and duration increased from 3 to 5 months, the modelled terminus remains stable.

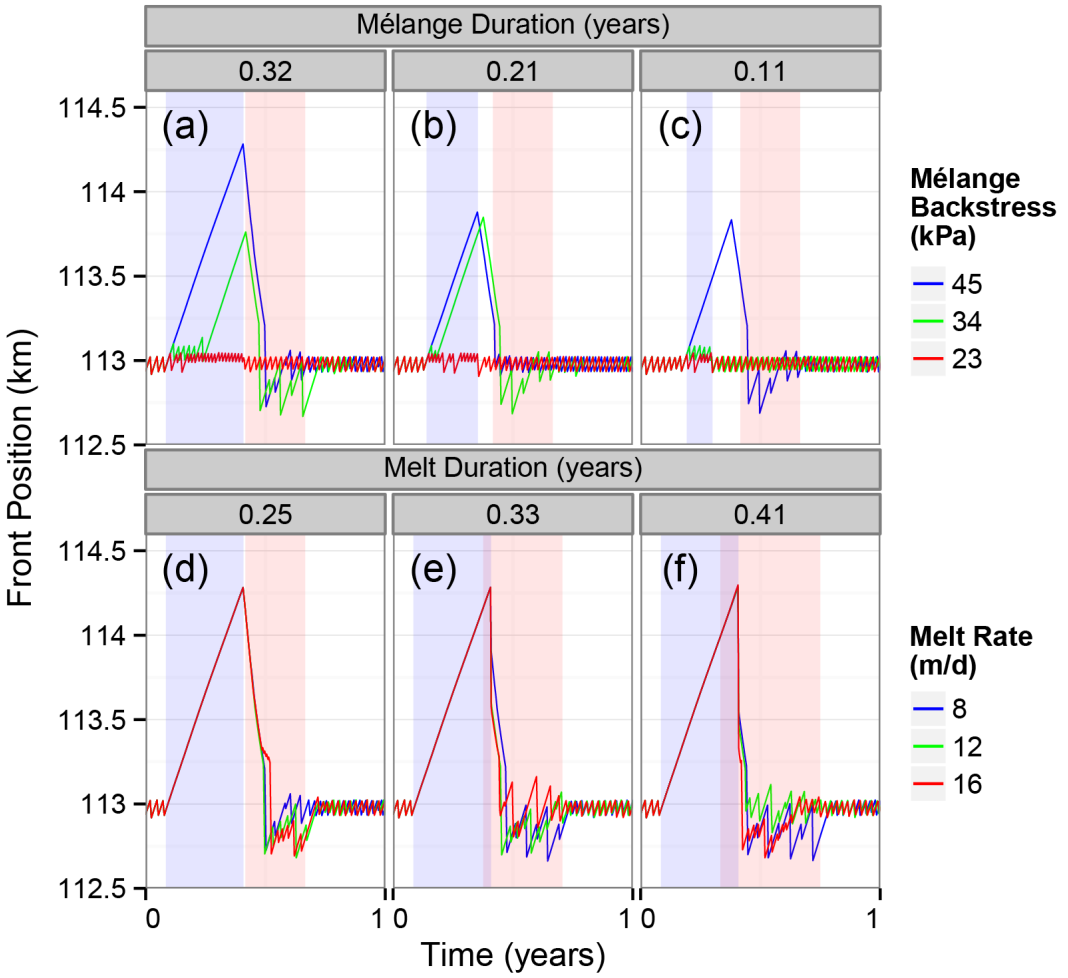

Figure 4.5: Terminus position through 1 year for all Experiment 2 perturbations. Each panel represents a different season length, while coloured lines indicate magnitude of forcing. Blue and red shading indicate mélange and melt season, respectively.

4.2 Discussion

The results of the modelling experiments shed new light on marine-terminating glacier dynamics and the calving mechanism. The calving dynamics of the modelled glacier vary significantly through the year (Experiment 1, Fig. 4.2), from

high-frequency (8.7 days), low-magnitude ($\sim$ 80 m) calving events when no seasonal forcing is applied to complete cessation of calving during the mélange season, with rapid retreat following mélange collapse, and seemingly stochastic calving behaviour during the melt season. This behaviour is in good overall agreement with year-round observation of Store (N. Chauché, personal communication, 2014). Figure 4.6 shows observed terminus evolution and upstream velocity from Howat et al., (2010). The modelled terminus evolution (Fig. 4.2) shows a similar trend to observations, with advance during the mélange season and rapid retreat following mélange clearing. However, the terminus range in the model was 1.3 km is greater than observed (0.5 km). This may be because the value reported by Howat et al., (2010) is the mean across the width of the terminus, while we are modelling a central flowline. In terms of velocity, observations are too sparse to draw conclusions about seasonal trends (Fig. 4.6), but the range 2500-4400 m a^{-1} is fairly consistent with the modelled range of 3900-5450 m a^{-1}, given that observed velocity is measured 5km upstream of the terminus.

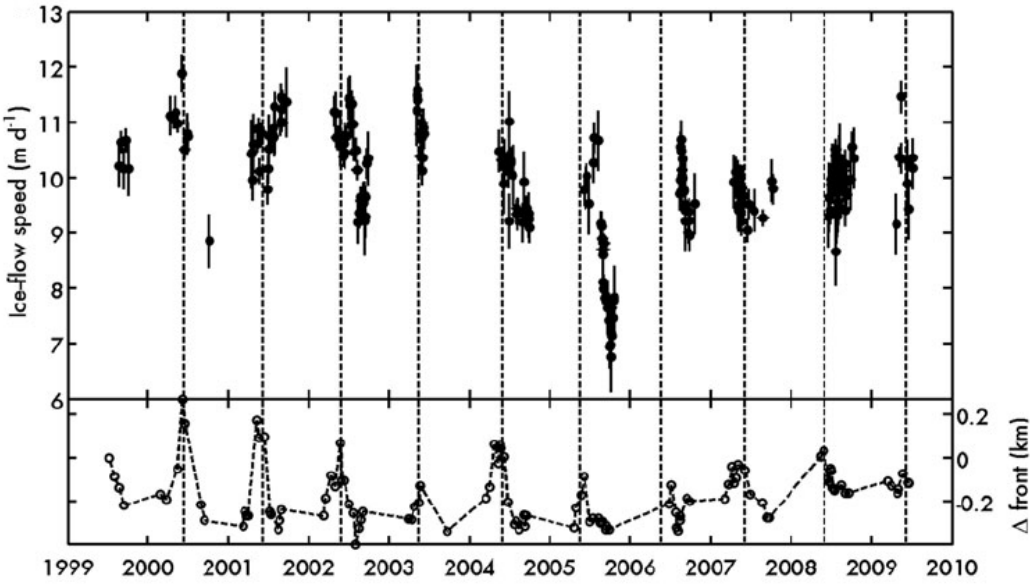

Figure 4.6: Store Glacier velocity (5km upstream of terminus) and terminus position (1999-2009) from Howat et al., (2010).

The model captures two important aspects of Store's behaviour. Seasonally, Store's terminus position is highly sensitive to external perturbation. However, on interannual timescales, Store's calving dynamics are stable, and the terminus position remains fairly constant (Howat et al., 2010). In the model, the seasonal

advance and retreat is specifically related to a floating tongue, which forms during winter in response to the buttressing effect of rigid mélange (Figs. 4.2, 4.3) and breaks apart once the buttressing effect of the mélange disappears. This finding provides theoretical understanding for the observed temporal correlation between mélange break-up and frontal retreat at Store and other glaciers in the Uummannaq region (Howat et al., 2010), as well as Jakobshavn Isbræ (Amundson et al., 2010) farther south, and glaciers such as Kangerdlugssuaq and Daugaard-Jensen on the east coast (Seale et al., 2011). The results from experiment 2 suggest that the estimate of Walter et al., (2012) of a mélange strength of 30–60 kPa is most likely correct, and that any future climate-driven reduction in mélange strength or thickness could significantly impact the seasonal dynamics of Store (Fig. 4.5).

When isolating the effect of submarine melting of the ice front (Experiment 1, Fig. 4.2), I found a slight increase in calving frequency, an associated decrease in calving event size, and a slight dampening of the glacier's velocity response to calving events. However, the overall effect of submarine melting alone was minimal. Only when combined with mélange forcing was submarine melting capable of significantly affecting calving dynamics (Fig. 4.2). This suggests that some process during the mélange season preconditions the glacier for slight instability later in the season. Potentially, the upward bending associated with the formation of the floating tongue (Fig. 4.3) changes the glacier geometry near the grounding line such that it is more susceptible to the effect of undercutting by submarine melting.

Despite doubling melt rates and increasing melt duration by 66 % in experiment 2 (Fig. 4.5), the terminus of Store remained stable at 113 km, suggesting that there is no direct link between submarine undercutting and longer-term calving stability of the grounded terminus at present. This result contradicts previous work suggesting that undercutting of the terminus promotes calving (Motyka et al., 2003; Rignot et al., 2010) by intensifying extensional stresses near the terminus (O'Leary and Christoffersen, 2013). I propose, however, that this apparent contradiction is a feature specific to Store, due to the strong stabilising influence of its topography.

The location of the terminus of Store coincides with a significant basal pinning point (Fig. 3.1), as well as a "bottleneck" in the fjord width (Fig. 1.1). The combined effect of these topographical features is to significantly affect the stress

field and crevasse depth. The suppression of crevasses penetration depth at the stoss side of the basal pinning point at the terminus exceeds the deepening of crevasses in response to undercutting of the ice front by submarine melting. As such, the latter alone cannot cause the front to retreat in this case. This suggests that, as long as the melt rate is less than the rate of ice delivery to the front, the terminus position of Store will be relatively insensitive to the rate of ice front melting. Thus, the rate of iceberg production will be solely controlled by the velocity at the terminus. The topographic setting of Store explains why this glacier remained stable during a period when others in the same region experienced rapid retreats (Howat et al., 2010) and, more generally, why neighbouring glaciers are often observed to respond asynchronously to similar climate forcing (Moon et al., 2012).

Inland of Store's stable frontal pinning point is a 28 km long overdeepening reaching 950 m below sea level (Fig. 3.1), which could make Store susceptible to sudden retreat, i.e. if the terminus becomes ungrounded from its current pinning point at 113 km. I found that, by forcing the model with unphysically large values for submarine melt rate (not shown), I was able to force the terminus back off its pinning point. This led to rapid retreat through the trough, a result which supports the Marine Ice Sheet Instability (MISI) hypothesis. However, none of the climate forcing scenarios were able to trigger such a retreat, which suggests that the current configuration of Store is stable and will most likely remain so in the near future.

As discussed above, the model is capable of reproducing the flow and seasonal calving dynamics of Store simply by perturbing the backstress exerted by mélange and the rate of submarine melting. The model excludes the effect of water in surface crevasses, which may conceivably affect calving due to hydrofracture if water levels are high (Benn et al., 2007a). Although recent work included this effect (Nick et al., 2010), I ignore it because high-resolution images captured in repeat surveys of Store with an unmanned aerial vehicle in July 2013 detected water in only a small number of surface crevasses near the terminus (Ryan et al., 2014). Although the possibility that undetected water is contributing to crevasse penetration cannot be excluded, it is not necessary to invoke this process to explain the observed behaviour of Store. This exclusion of hydrofracturing is a useful model simplification, as it is difficult and potentially impossible to accurately estimate the depth of water in crevasses. The latter would require

knowledge of surface meltwater production as well as the number and size of surface crevasses, which is infeasible with the type of model used here.

Although the model captures the flow and seasonal calving dynamics of Store in a realistic manner, it is important to note that the outcome of the study is specifically limited to this glacier and that multiyear dynamics remain to be fully investigated. I use inverse methods to determine basal traction, rather than a hydrological model; this ensures that the flow field matches observations, allowing us to focus on processes at the terminus. However, prescribing basal traction means I am unable to investigate its interannual evolution in response to dynamic thinning, rising sea level or hydrological processes. The difficulty of implementing realistic hydrological routing in a flow line model suggests that only a 3D model will be fully capable of representing these processes.

It is useful, at this point, to compare the development of time-evolving models for calving with recent developments in the implementation of grounding line dynamics. The lack of consistency of grounding line treatment in ice flow models was raised by Vieli and Payne (2005), and this issue has since received a great deal of attention from the ice sheet modelling community. A comprehensive intercomparison study, MISMIP (Pattyn et al., 2012), compared the ability of various 2D ice flow models to simulate grounding line dynamics, before MISMIP3d (Pattyn et al., 2013) did the same for 3D models. Similarly, I hope that the 2D model presented here will guide the future development of full 3D time-evolving models for calving.

Finally, I note that, in terms of accounting for the feedback between crevasse formation and bulk density and flow characteristics, a damage mechanics approach may prove useful (Pralong and Funk, 2005; Borstad et al., 2012). A counterpart study to this one by Krug et al. (2014) attempts to couple a damage model with a calving model for Helheim Glacier using Elmer/Ice.

The results suggest that ice mélange is primarily responsible for Store Glacier's seasonal advance and retreat. No significant response was exhibited to either variations in basal friction or submarine melt rate. This could be interpreted as evidence of the unimportance of these processes. This interpretation is at odds with the large body of evidence linking calving glacier sensitivity to changes occurring in the ocean (Motyka et al., 2011; Rignot et al., 2010; Seale et al., 2011). It is possible that these perturbations in the ocean resulted in shorter ice mélange seasons, leading to calving retreat. However, the model does not retreat in the

absence of mélange, so this hypothesis is also unsupported by the results. Instead, I suggest that topographic control is responsible for Store's insensitivity to both submarine melting and basal friction. Store's terminus currently sits on a significant basal pinning point (Fig. 3.1), and at a constriction in valley width (Fig. 1.1). Both of these topographic effect are hypothesised to encourage terminus stability (Section 2.2.3). Further evidence for Store's topographic stability comes from Howat et al., (2010), who observed that Store's terminus position remained stable between 2000-2010, while other glaciers in the Uummannaq region retreated. While submarine melting is a process with the potential to destabilise the terminus by increasing stress and opening crevasses, ice mélange is a stabilising influence, buttressing the terminus and closing crevasses. The results of the 2D model suggest that Store's terminus is currently too stable to be overcome by melt undercutting, but that crevasse closure by mélange buttressing permits the terminus to advance beyond its pinning point as a floating tongue.

4.2.1 Tuning

I found it necessary to apply a tuning factor to the crevasse depth model (Eqns. 3.17, 3.18); the effective stress term (τ_E) is scaled by a factor of 1.075. This suggests that either the crevasse depth criterion is based on flawed assumptions, or that the 2D model fails to properly capture the underlying physics. Chapter 6 will show that the 3D model is able to reproduce observed seasonal behaviour *without tuning*; this suggests that it is a limitation of the 2D model which leads to the underprediction of crevasse depth.

There are several potential reasons which might explain the need for a tuning factor. Firstly, the model does not account for the reduction in bulk density associated with the opening of crevasses, and so the creep closure term in Equation 3.17 is likely to be overestimated. However, this is also the case in the 3D model which correctly predicts crevasse depth, making this unlikely. Secondly, I assume a constant temperature of $-10\,^{\circ}\mathrm{C}$; the effect of temperature on the stress-strain relationship of ice means that this assumption probably affects the near-terminus stress field.

More fundamentally, a 2D flowline model implicitly assumes that the terminus is straight in the neglected lateral dimension. In other words, the terminus is assumed to traverse in a straight line from one side of the fjord to the other.

This is not the case for Store Glacier, whose terminus is frequently observed to be composed of headlands and bays, which undoubtedly affects the stress regime.

In terms of climate forcing, the absence of the lateral dimension is most significant for submarine melting. In reality, multiple roughly conical plumes emerge from the terminus of Store Glacier, resulting in significantly heterogeneous undercutting (Chauché et al., 2014). However, in 2D no lateral variability is possible, and I am limited to investigating the centre of a single plume.

Finally, Store's terminus at the central flowline is usually further advanced into the fjord than the lateral margins. As such, this central region of the terminus will experience reduced lateral drag from the valley walls. By imposing lateral drag as discussed in Section 3.3.1, I may, therefore, be overestimating the resistive stress here, inhibiting calving.

CHAPTER 5

The 3D Model: Methods

Following successful development of the 2D calving model described with application to Store Glacier in Chapter 3, I progressed to the 3D implementation. For many reasons, the 3D model proved more challenging. Issues involving the changes in geometry became inherently more complex with the addition of a new dimension. Furthermore, the size of the numerical problems to be solved is significantly larger, which made running and testing the model computationally expensive. This chapter describes how the 3D model was developed, and the numerical and computational methods involved, as well as the application of the model to Store Glacier. Chapter 6 presents and discusses the results of the application to Store Glacier.

All of the calving model development and testing, the model application to Store Glacier and subsequent data analysis were carried out by J. Todd, with guidance from P. Christoffersen and T. Zwinger. Bathymetric data used to constrain Store's near terminus geometry, as well as oceanographic data for the proglacial fjord, were provided by A. Hubbard and N. Chauché. TerraSAR-X data which were used to invert for basal drag (Section 5.7), and from which front positions were extracted (Section 6.3.1), were provided by A. Luckman. UAV imagery used to determine plume location and to help characterise Store Glacier's calving behaviour was collected by J. Ryan and N. Toberg. Subsequent analysis of UAV data to provide ice mélange thickness and strength estimates was carried out by N. Toberg. The analytical plume models used to estimate melt rates at Store (Section 5.9.2) were provided by D. Slater and T. Cowton. I am very grateful to all of the aforementioned collaborators for their help, without which this project would not have been possible.

5.1 3D Model Domain

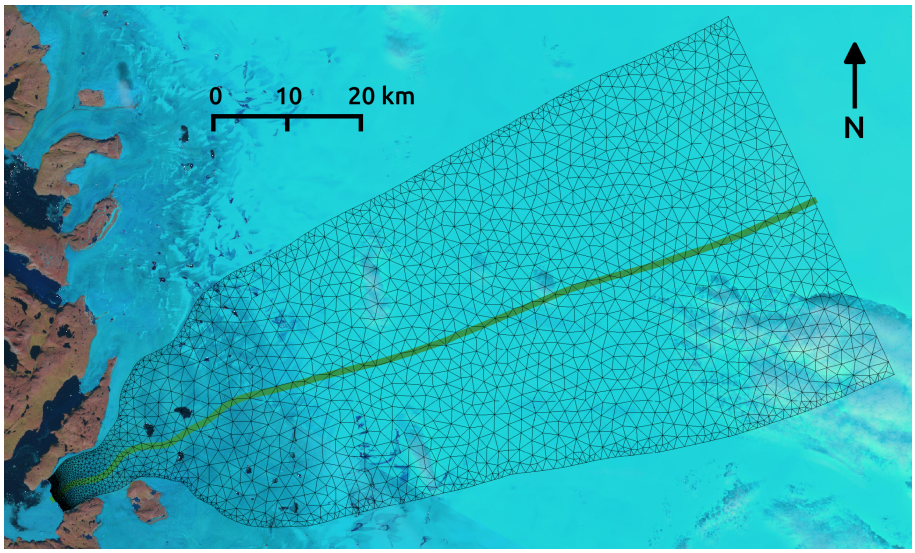

Figure 5.1: Plan view of the 3D model mesh of Store Glacier. The mesh resolution increases significantly towards the terminus. Green line indicates flowline of 2D model.

As in the 2D case, I chose to model a domain which extends significantly inland from the terminus of Store Glacier. The central flowline modelled in 2D, as described in Chapter 3, extended 113 km inland, and began where ice velocity first exceeds $100\,\mathrm{m\,a^{-1}}$ at the surface. In 3D, I maintain this longitudinal coverage, and extend the domain laterally so that the model covers the entire glacier catchment (Fig. 5.1).

The edges of Store Glacier's ice catchment is a natural choice for the lateral boundaries of the model mesh, as it means a 'no penetration' boundary condition can be specified there. I chose to extend the domain as far inland as in the 2D application to ensure that the terminus was insensitive to the inflow boundary. Furthermore, this allows us to thoroughly investigate the extent to which dynamic changes initiated at the terminus are transmitted upstream through longitudinal coupling. Finally, due to the ability of the Finite Element Method to operate on meshes of variable resolution, it is possible to extend the domain more than 100 km inland with little additional computational cost as the mesh can easily be made coarser in the interior, where ice flow is slower.

The basal topography from near the glacier terminus is shown in Figure 5.2. This shows that, as the ice reaches the terminus in the northern side, it is rising

up onto a bedrock sill. In the southern side, the ice flows over a bedrock sill 2km inland of the terminus; downstream of this inland bedrock bump the bed deepens once more.

The model domain (Fig. 5.3) is constrained by 6 boundary conditions: the base of the ice (Γ_{base}), the upper ice surface (Γ_{surf}), the inflow (Γ_{inflow}), the calving front (Γ_{term}), and the two lateral boundaries (Γ_{left} and Γ_{right}).

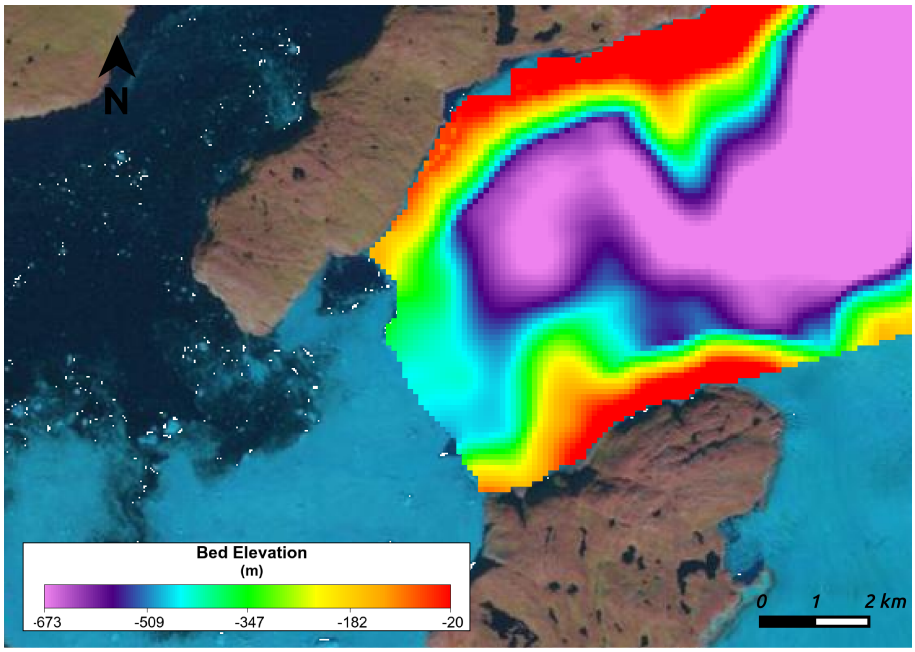

Figure 5.2: Bed topography for Store Glacier produced via mass conservation as described in Appendix A.2

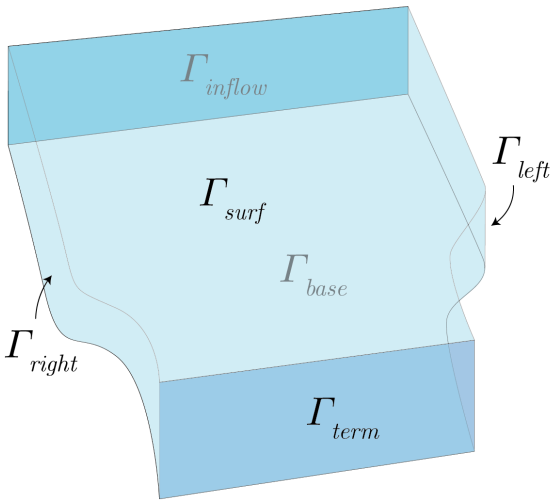

Figure 5.3: Schematic of the model domain with boundary conditions annotated.

5.2 The Mesh

The Finite Element Method for solving Partial Differential Equations operates on an unstructured mesh, consisting of nodes, which are the points at which the solution is evaluated, and elements between these nodes, in which the integral of the PDE is defined. Various algorithms exist for 3D mesh generation. These algorithms operate by iteratively adding and removing nodes to improve some heuristic condition of the mesh, typically aspect ratio. Unfortunately, the meshes which result from these algorithms are inappropriate for a high aspect-ratio domain such as a glacier catchment. Instead, the desired mesh should have a vertical resolution which is much finer than the horizontal, so as to capture the glacier's internal deformation, while still allowing relatively coarse treatment of horizontal aspects of flow.

To address this problem, Elmer/Ice features internal mesh extrusion (`MeshExtrude`), whereby the user supplies a 2D plan-view mesh, and two DEMs describing surface and bed elevation. Elmer/Ice then extrudes this plan-view mesh to the desired number of vertical layers, and adjusts the z-coordinate to match the supplied data.

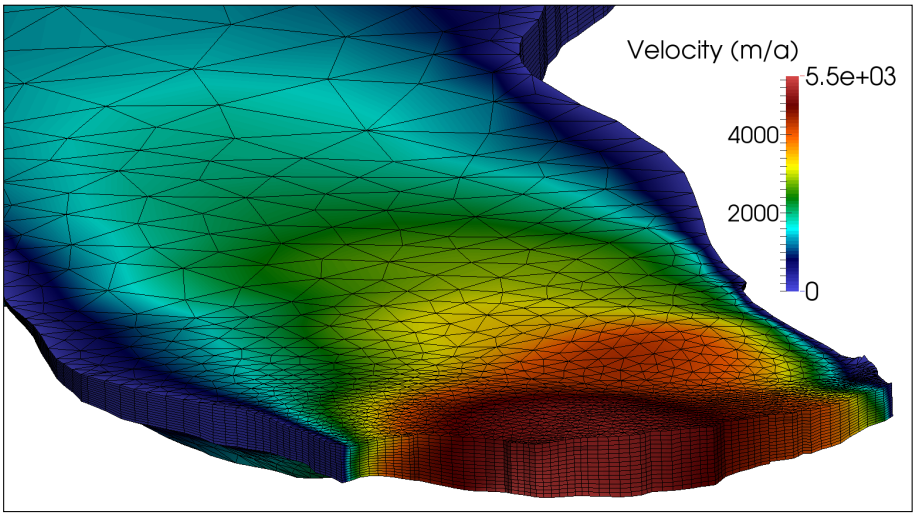

Figure 5.4: 3D model mesh of Store Glacier as viewed from the northern ridge next to the glacier. The mesh is unstructured in the horizontal direction, but vertically extruded. Mesh resolution increases from 2km in the interior to 100m at the terminus.

5.3 Ice Dynamics

As with the 2D model, the bulk of the computational effort is concerned with solving for the flow of ice. I use the `FlowSolve` module of Elmer/Ice to solve the Stokes equations (Eqs. 2.1, 2.2), using Glen's flow law (Eq. 2.3) to describe the stress-strain relationship of ice.

As discussed in Section 5.4, I solve for the temperature distribution of the ice; the flow field is coupled to the temperature solution via the Arrhenius factor (A) in Glen's flow law.

Recalling the Arrhenius (rate factor) Equation (Eq. 2.4), which describes the evolution of ice stiffness (A) with respect to temperature (T_h):

$$A = A_0 e^{-\frac{Q}{RT_h}}, \tag{5.1}$$

where the reference rate factor (A_0) and the activation energy (Q) depend on temperature (T_h) (Cuffey and Paterson, 2010), and R is the gas constant. I use the following values for the parameters in the rate factor equation, consistent with several previous studies using Elmer/Ice (Gagliardini et al., 2013; Gillet-Chaulet

et al., 2012; Seddik et al., 2012):

$$A_0 = \begin{cases} 3.985 \times 10^{-13}\,\mathrm{s^{-1}\,Pa^{-3}}, & \text{if } T_h < -10.0 \\ 1.916 \times 10^{3}\,\mathrm{s^{-1}\,Pa^{-3}}, & \text{otherwise} \end{cases} \tag{5.2}$$

$$\tag{5.3}$$

$$Q = \begin{cases} 60\,\mathrm{kJ\,mol^{-1}}, & \text{if } T_h < -10.0 \\ 139\,\mathrm{kJ\,mol^{-1}}, & \text{otherwise} \end{cases} \tag{5.4}$$

$$\tag{5.5}$$

$$R = 8.314\,\mathrm{J\,mol^{-1}\,K^{-1}} \tag{5.6}$$

5.3.1 Boundary Conditions

On the inflow boundary (Γ_{inflow}), I prescribe annual mean observed surface velocity from InSAR-derived surface velocity data:

$$\boldsymbol{u} = \boldsymbol{u}_{obs} \qquad \text{on } \Gamma_{inflow} \tag{5.7}$$

For simplicity, I assume that ice velocities at depth are the same along this boundary. Observed velocities at the inflow boundary are around $100\,\mathrm{m\,a^{-1}}$, and while it would have been possible to prescribe a depth-dependent velocity profile based on the Shallow Ice Approximation, the difference in total flux would be small, as most deformation occurs in the lower layers of the ice.

The lateral boundaries (Γ_{left},Γ_{right}) are aligned with the edge of Store's ice catchment (Section 5.1), and so I impose a no penetration condition on these boundaries. Flow tangential to these boundaries is controlled by a Neumann boundary condition, prescribing a slip coefficient. Thus, the lateral boundary condition is:

$$u_\perp = 0 \qquad \text{on } \Gamma_{left}, \Gamma_{right} \tag{5.8}$$

$$\sigma_\parallel = -u_\parallel \beta \qquad \text{on } \Gamma_{left}, \Gamma_{right} \tag{5.9}$$

where the subscripts $_\perp$ and $_\parallel$ refer to the perpendicular and tangential components. Note that there is one perpendicular and 2 tangential components in 3D. β is the slip coefficient which, for the lateral boundary, is prescribed dependant

on whether the boundary is an ice-ice ($\beta = 1.0E-3$) or ice-rock ($\beta = 1.0E-2$) boundary.

For grounded ice, the basal boundary condition (Γ_{base}) is identical to the lateral, although rather than prescribing an approximate value for β I employ inverse methods to estimate the spatially and temporally variable β field (Section 5.7). Grounded ice is not permitted to move perpendicular to the bed. When flotation occurs, the boundary condition changes to account for this. Floating ice encounters negligible basal friction, and so traction is set to zero. The floating base is permitted to move up or down in response to changes in normal stress ($\sigma_\perp$) which is equal to the pressure from the sea when present:

If grounded:

$$u_\perp = 0 \qquad \text{on } \Gamma_{base} \tag{5.10}$$

$$\sigma_\parallel = -u_\parallel \beta \qquad \text{on } \Gamma_{base} \tag{5.11}$$

If floating:

$$\sigma_\perp = \min(-\rho_w g(z - z_{sl}), 0) \qquad \text{on } \Gamma_{base} \tag{5.12}$$

$$\sigma_\parallel = 0 \qquad \text{on } \Gamma_{base} \tag{5.13}$$

In reality, subglacial hydrology dictates this water pressure, but I do not model the subglacial hydrology, and in the region near the terminus where the ice approaches flotation, sea pressure provides a reasonable approximation, assuming an efficient subglacial drainage system.

The calving terminus (Γ_{term}) experiences no traction, as it is in contact with either air or water, and the normal stress is equal to sea pressure below sea level, and zero otherwise:

$$\sigma_\perp = \min(-\rho_w g(z - z_{sl}), 0) \qquad \text{on } \Gamma_{term} \tag{5.14}$$

$$\sigma_\parallel = 0 \qquad \text{on } \Gamma_{term} \tag{5.15}$$

The upper ice surface (Γ_{surf}) is stress free:

$$\boldsymbol{\sigma}_{\perp} = \mathbf{0} \qquad \text{on } \Gamma_{surf} \tag{5.16}$$

5.4 Ice Temperature

In the 2D model, I assumed a constant temperature of $-10\,^{\circ}\mathrm{C}$. In the 3D case, however, I use the temperature solver in Elmer/Ice to gain more accurate estimates of the ice viscosity and thus also the stresses within the ice. During the inversion and spin up phase of the model (Section 5.7), I solve for steady-state ice temperature using the Elmer/Ice module `TemperateIce`. Once the spin up has reached a steady state, the temperature field is extracted from the model and saved in a NetCDF file.

In the calving simulations, I interpolate the temperature field from the NetCDF file created during spin up, rather than solving for it. This reduces the computational cost by an order of magnitude, as the temperature and flow solution are strongly coupled, meaning they must be solved iteratively at each timestep.

Given that the calving model is concerned with dynamic response on timescales ranging from days to a few years, the ice temperature is unlikely to evolve significantly over the course of the simulations. I therefore consider the model to be equipped with a realistic temperature field, while also remaining computationally efficient.

The temperature boundary condition on the upper ice surface (Γ_{surf}) is derived from the MODIS Ice Surface Temperature product (Hall et al., 2012), available at `http://modis-snow-ice.gsfc.nasa.gov/?c=greenland`. The 2000-2014 monthly data were reduced, first into calendar month averages over the period, then into an annual average map. The resulting temperature field is applied to Γ_{surf} as a Dirichlet boundary condition. I also use this mean temperature product to set the temperature on the upstream inflow boundary (Γ_{inflow}), constant through depth. Thus:

$$T = T_{obs} \qquad \text{on } \Gamma_{surf}, \Gamma_{inflow} \tag{5.17}$$

On the lateral and calving boundaries (Γ_{left},Γ_{right},Γ_{term}), I assume no heat

transfer (i.e. adiabatic boundary condition).

On the base of the ice (Γ_{base}), there are two sources of heat: frictional heating and geothermal heat flux. For the geothermal source, I apply a constant flux of $75\,\mathrm{mW\,m^{-2}}$ following the estimate of Greve, (2005). The basal frictional heating source (q_{bf}) is the product of tangential velocity ($U_{\parallel}$) and basal friction (τ_b):

$$q_{bf} = \tau_b U_{\parallel} \tag{5.18}$$

In Elmer/Ice, the module `USF_GetFrictionHeating` computes this contribution. I found that the frictional source is typically orders of magnitude larger than the geothermal; this reduces the impact of the significant uncertainty in the geothermal estimate (Christoffersen et al., 2012).

A final source of heat, within the ice body, comes from internal strain heating:

$$q_{strain} = \boldsymbol{\tau} \cdot \dot{\boldsymbol{\epsilon}} \tag{5.19}$$

and this contribution is computed by the module `DeformationalHeat`.

5.5 Surface Evolution & Mass Balance

Glacier geometry evolves through time in response to ice flow and mass balance. As such, the shape of the free surfaces must be solved for at each time step, following the convergence of the Stokes equations (Section 5.3). The upper ice surface evolves freely, while on the base of the glacier, the surface is limited, due to the inability of ice to penetrate the bedrock. The calving front also evolves over time, as discussed in Section 5.6. The lateral margins and the influx boundary are fixed.

The evolution of the height (h) of the glacier's surface is described by the kinematic free surface equation:

$$\frac{\partial h}{\partial t} + u_x \frac{\partial h}{\partial x} + u_y \frac{\partial h}{\partial y} - u_z = \left[1 + \left(\frac{\partial h}{\partial x}\right)^2 + \left(\frac{\partial h}{\partial y}\right)^2\right]^{1/2} a_{\perp} \tag{5.20}$$

where $a_{\perp}$ is the accumulation normal to the surface. Equation 5.20 computes the change in surface height ($\frac{\partial h}{\partial t}$) from the advection of thicker or thinner ice (second and third terms on l.h.s.), uplift (u_z) and accumulation/ablation (r.h.s.).

These components are illustrated in Figure 5.5. The movement of the nodes is limited to the z-direction so that mesh quality is maintained; this is an Eulerian approach with respect to the horizontal directions. As such, the displacement of the nodes is the product of the applied forcing (advection, accumulation) and the surface slope. This is illustrated in Figure 5.5, where the blue arrow represents the direction of the surface displacement, while the red arrow indicates the resulting movement of the nodes in the z-direction only.

Aside from the velocity field, the only other component of the free surface evolution is accumulation and ablation, a. I apply surface mass balance (SMB) from RACMO 2.3 data (Noël et al., 2015), averaged over the period 1958-2013. Although, accumulation and ablation vary seasonally, I apply annually averaged SMB for simplicity, as seasonal variability is unlikely to have a significant effect on ice flow due to the diffuse nature of the forcing.

On the base of the glacier the surface is fixed, except when basal water pressure approaches ice overburden, in which case the base of the ice may begin to lift off of the bed (flotation).

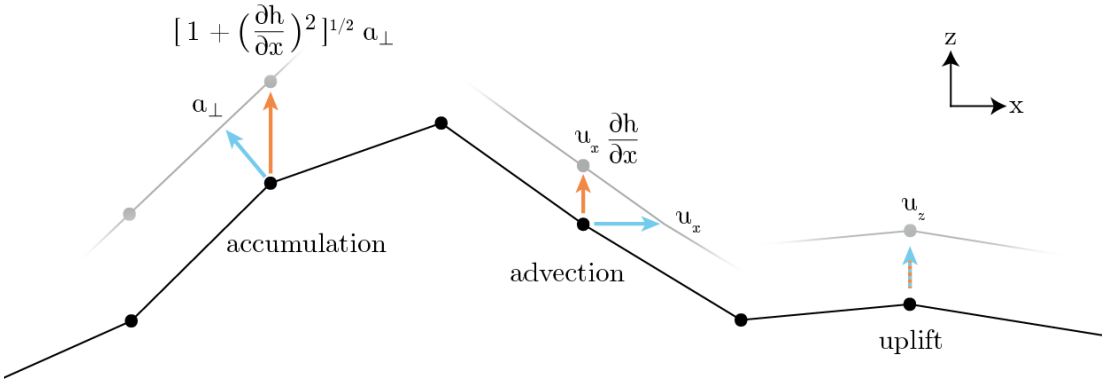

Figure 5.5: Illustration of the Free Surface Equation (Eq. 5.20) which is used to predict the evolution of the upper and lower ice surfaces (shown in 2D for simplicity). Node movement is restricted to the z-direction, and so physical processes (blue arrows) must be implemented with a consideration of the surface slope (red arrows). Grey lines indicate the natural evolution of the surface in response to the corresponding physical process. Under a Lagrangian approach, the nodes would shift to the head of the blue arrow. However, in the Eulerian approach, the node shifts to the point on the new surface (grey line) which is vertically aligned with its current location (red arrow).

5.6 Ice Front Evolution - `FrontAdvance3D.F90`

In addition to the upper and lower free surfaces discussed in Section 5.5, the calving front is also a free surface whose evolution must be resolved at each timestep. Unlike the upper and lower surfaces, evolution of the front occurs as a result of two distinct processes: continuous advance due to dynamics, and instantaneous retreat due to fracture (calving). This section describes the implementation of the former, while the latter is discussed in Section 5.8. As with the upper and lower surfaces, the evolution of the front is governed by the ice velocity and accumulation/ablation, which in this case is composed entirely of submarine melting, the computation of which is discussed in Section 5.9.2.

Rotated Coordinate System

The current implementation of the calving (Section 5.8) and remeshing (Section 5.8.2) algorithms require that the terminus remains projectable in some rotated coordinate system. I define a coordinate system in which the x-axis spans the terminus from side to side, and the z-axis is roughly aligned to the direction of ice flow. By temporarily rotating the model geometry into this coordinate system to compute front evolution, I can treat the free surface in a similar manner to the upper and lower surfaces (Section 5.5), and easily impose the requirement of projectability. For the remainder of this section, I discuss calving front evolution in this *rotated coordinate system*, as this is the coordinate system in which the relevant mathematics apply.

Lagrangian Approach

The computation of free surface evolution is complicated by the fact that the calving front often exhibits much higher gradients, in the rotated coordinate system, than the upper and lower free surfaces. This is because the upper and lower ice surface are orthogonal to the gravity vector, which means that sharp edges are smoothed out by ice flow. However this is not the case for the ice calving front, which is oriented parallel to the gravity vector. Furthermore, calving events also leave sharp edges and steep gradients in the terminus when propagating fractures cause icebergs to break off.

Figure 5.5 illustrates why high gradients cause problems for the stability of

the free surface equation. The components of Equation 5.20 which account for advection and accumulation both depend on the surface gradient, due to the fact that nodes are only permitted to move vertically (in the rotated coordinate system). Note, for example, that the nodal displacement due to accumulation in Figure 5.5 is larger than the accumulation itself. As the surface gradient increases, the displacement resulting from accumulation and advection become much larger than the actual forcing; this is a fundamental limitation of the free surface equation.

I first attempted to address this limitation by modifying the free surface equation in regions of high gradient. However, this required neglecting important dynamic and ablation terms, as well as a somewhat arbitrary choice for the threshold between 'high' and 'low' gradient. Furthermore, this treatment often led to unphysical terminus geometry in regions of conical plume melting.

It became apparent that the free surface equation (Eq. 5.20) is not a suitable framework for the evolution of a calving terminus in 3D. Instead, I adopt a *fully Lagrangian* approach, in which the nodes on the terminus are free to move in any direction in response to dynamics and ablation. In this approach, the displacement of nodes is a vector ($\boldsymbol{d}$) defined by:

$$\boldsymbol{d} = \boldsymbol{u} + a_{\perp} \tag{5.21}$$

where $\boldsymbol{u}$ is velocity and $a_{\perp}$ is accumulation normal to the front. In this way, node movement is no longer restricted to the vertical direction. Figure 5.5 illustrates the difference between the Eulerian free surface method (Eq. 5.20) and the Lagrangian approach (Eq. 5.21).

This treatment of front evolution is, at face value, significantly simpler than the free surface approach (Eq. 5.20); indeed, there is no longer a Partial Differential Equation to solve. However, by allowing the nodes to move in any direction, projectability of the terminus is no longer guaranteed. Therefore, a post-processing step is required to check and enforce projectability by moving nodes laterally. Section 6.3.7 discusses in more detail the requirement for projectability, its limitations and potential alternatives to be explored in future work.

5.7 Basal Inversion & Spin Up

Basal drag is the predominant source of resistance to flow under most of Store Glacier, and indeed most of the Greenland Ice Sheet. This means that an accurate estimate of basal drag is *essential* for modelling ice flow. However, little is known about the properties of the till or bedrock over which Store Glacier flows, nor is the subglacial hydrological system well constrained. For these reasons, I carry out inverse simulations to constrain basal drag under the model domain. This involves using observed surface velocity to drive an 'inverse' flow model, in order to determine the basal slip coefficient (β) and its seasonal variability.

Elmer/Ice is equipped with solvers to invert the full-Stokes flow model using the adjoint method, thanks to Gillet-Chaulet et al., (2012). I use this adjoint solver in conjunction with seasonal velocity data provided by A. Luckman from 24 TerraSAR-X 11-day image pairs collected from April 2014 to April 2015. This process is complicated by the fact that the upper ice surface is free to evolve (Section 5.5). Simply running the inversion once before running the forward model results in a poor fit between modelled and observed velocities, because the upper surface rapidly adjusts, changing the driving stress (τ_D) which alters the force balance. Therefore, it is necessary to iteratively invert for the basal slip coefficient and evolve the upper ice surface.

I begin by reducing the seasonal velocity maps into a representative annual mean, and then using this annual velocity to drive an initial inversion which produces an annual basal slip map. The forward ice flow model is then run for a few years with this annual basal slip map to permit the surface to evolve towards a steady state. This new glacier geometry is then used to carry out another inverse simulation, and the process is repeated until convergence is achieved. At each stage, the model geometry was checked to check for instability of the free surface solution, particularly near boundaries; these instabilities manifest as visible unphysical 'spikes' in the surface. If and when instability was detected, the spin-up was restarted from the last checkpoint.

I wish to model the seasonal variability in basal conditions and velocity in order to investigate its effect on calving. To this end, a series of 20 inversions was carried out using 20 velocity maps, which were temporally interpolated evenly throughout the year from May 2014 to May 2015. This produced a timeseries of

basal slip coefficient maps, which allows us to specify seasonal variation in basal slip consistent with observations, without knowing the specific nature of basal sediment and the basal hydrological system.

The final stage of the inversion and spin-up phase of the model involved running the forward model for 300 years with seasonally variable basal slip, with a timestep of 0.05 years, until a steady-state was achieved. This spin-up phase ensures that, when the model is forced with external climate processes, the observed response is real, rather than simply an adjustment to the glacier's internal dynamics. During this spin-up the terminus position was fixed and the calving model was not active, as it requires up to 100 times as many timesteps per year of simulation time, rendering it prohibitively computationally expensive. This simplification is also justified by the fact that Store Glacier's current terminus position has remained stable for at least the past 40 years (Weidick et al., 1995, p.C41).

5.8 Modelling Calving in 3D

As in the 2D case (Chapter 3), I implement the *crevasse depth calving model* (Benn et al., 2007b; Nick et al., 2010), which predicts the occurrence of calving based on the penetration of surface and/or basal crevasses. Two variants of the crevasse depth calving model exist: the original model proposed by Benn et al., (2007b) suggests that calving occurs when surface crevasses meet the waterline, at which point hydrofracturing leads to full thickness calving. A modification developed by Nick et al., (2010) takes into consideration the formation of basal crevasses, and states that calving occurs when surface and basal crevasses meet. Both of these models are feasible, and so I implement *both*, and predict calving when either condition is met. Here, I make a modification to the equation which determines crevasse depth.

The foundation of the crevasse depth model is the observation by Nye, (1957) that, in the case of negligible surface slope, tensile stresses exist to a depth where:

$$\rho g d = 2\tau \tag{5.22}$$

This equation effectively splits the essentially unmeasurable Cauchy, or full,

stress (σ) into the ice overburden component on the left, and the deviatoric term (τ), of dynamic origin, on the right. Thus, based on the hydrostatic assumption ($\sigma_{zz} = -\rho g d$), and the assumption that horizontal deviatoric stress remains constant through depth, crevasse penetration can be estimated purely from surface measurements. This 'observational' formulation of the crevasse depth model is further exemplified by the work of Benn et al., (2007a,b) who invert Glen's flow law to substitute the deviatoric stress term with a strain rate term.

Previous modelling studies using the crevasse depth model (Nick et al., 2010; Vieli and Nick, 2011) have implemented it into depth integrated flow simulations, meaning that the two assumptions outlined above are justifiable. However, as the full-Stokes flow solution is solved, it is no longer necessary nor desirable to split the Cauchy stress (σ) into its dynamic and hydrostatic components; instead, the Cauchy stress can be computed everywhere directly from the flow solution. In this case, the Nye, (1957) crevasse depth model states that crevasses should exist to a depth where:

$$\sigma = 0 \tag{5.23}$$

which illustrates the underlying simplicity of the Nye, (1957) crevasse criterion: *crevasses exist where extensional stress exists to open them.*

I note also an ambiguity in the stress terms in Equations 5.22 and 5.23. In Nye, (1957), τ signified the horizontal deviatoric stress τ_{xx}, as the study considered glacier dynamics in a 2D flowline. However, in a 3D context, it is less clear which component of the stress field should be signified by σ (or τ).

Presently, I argue that extensional stress in *any* direction should be sufficient to open a crevasse and, as such, I make use of the first principal Cauchy stress (σ_1). The first principal stress represents the 'most' extensional eigenvalue of the stress tensor, and will be positive where a true extensional stress exists, and negative if the stress regime at a point is entirely compressional.

A counterargument to the choice of arbitrary stress direction would be that it is difficult to envisage how an extensional stress closely oriented to the z-axis could result in vertical crevasse propagation. However, it is equally difficult to envisage how a truly extensional stress in a glacier *could* be oriented close to the z-axis, given the effect of gravity. Indeed, analysis of preliminary results indicated that this was never the case.

I define two 'net stress' values for surface and basal crevassing:

$$\sigma_{surf} = \sigma_1 \tag{5.24}$$

$$\sigma_{basal} = \sigma_1 + P_w \tag{5.25}$$

where P_w is water pressure in basal crevasses. Where the values of σ_{surf} and σ_{basal} are greater than zero, open surface and basal crevasses are predicted to occur, respectively.

Water pressure (P_w) enters into Eq. 5.25 because the high water pressure of the subglacial hydrological system is essential for the opening of basal crevasses, due to the high, compressive overburden pressure of the glacier at depth. Surface crevasses, on the other hand, are capable of opening and remaining open without water pressure. Aerial photography from Store Glacier indicates that only a small number of surface crevasses fill with water during the summer melt season (Ryan et al., 2015). Furthermore, the presence and depth of this surface meltwater in crevasses is extremely difficult to predict, depending not only on surface melt rates, but also crevasse geometry and the supra- and englacial drainage systems. As such, I do not attempt to model the influence of this meltwater on surface crevasses.

Basal water pressure is, in reality, controlled by the subglacial hydrological system, which I do not model in the present study. Instead, I rely on the fact that basal water pressure is only important near the terminus, where calving may occur. The base of the hydrological system is defined by sea level: the observation that water is discharged outwards from the subglacial system into the fjord requires that the subglacial water pressure is higher than that in the fjord (sea pressure). I assume that the discharge through the hydrological system here is sufficiently high to imply an efficient drainage system, and thus that the water pressure gradient (piezometric gradient) is sufficiently low that sea pressure provides a reasonable estimate of basal water pressure near the terminus.

The above assumption allows us to estimate water pressure at the base of the glacier (P_{wb}) near the terminus. Within a basal crevasse filled with fresh meltwater, water pressure drops at a rate dictated by the density of fresh water

(ρ_{fw}). Thus, water pressure in a basal crevasse (P_w) is given by:

$$P_{wb} = (z_{sl} - z_b)\rho_{sw}g \tag{5.26}$$

$$P_w = P_{wb} - (z - z_b)\rho_{fw}g \tag{5.27}$$

where ρ_{fw} and ρ_{sw} are the densities of fresh and salt water respectively, z is elevation, z_{sl} is sea level, and z_b is the elevation of the base of the ice.

In the 2D model (Section 3.6), calving is defined by a point along the length of the glacier where surface and basal crevasses meet. However, calving in the 3D model does not occur until surface and basal crevasses meet along an uninterrupted line which meets the terminus in two locations, isolating a portion of the glacier from the remainder of the terminus. This makes the algorithm for identifying calving events in 3D significantly more complex compared to the 2D case. Furthermore, the change in glacier geometry which results from successive calving events mean that the model mesh can become 'degenerate'. As such, in addition to the 3D calving algorithm (Section 5.8.1), it was necessary to develop routines for remeshing the glacier following calving events (Section 5.8.2).

5.8.1 3D Calving Algorithm - `Calving3D.F90`

The first stage in predicting calving events is the calculation of crevasse penetration. To this end, it is necessary to compute the values of the Cauchy stress tensor ($\boldsymbol{\sigma}$), for which Elmer/Ice provides the solver `ComputeDevStress`. This solver is run following the completion of the `FlowSolver` at the current timestep. Subsequently, at the end of each timestep, the 3D calving solver (`Calving3D`) is called. `Calving3D` uses the previously computed Cauchy stress tensor to calculate crevasse depth and identify if and where calving occurs. The full algorithm for identifying calving is shown in Fig. 5.6.

The first stage of the calving algorithm is to compute, for each node in the 3D mesh, σ_{surf} and σ_{basal}, the surface and basal 'net stress' values, whose values indicate the presence or absence of open crevasses. Next, a 2D planar mesh (`PlaneMesh`) is generated, which covers the extent of the 3D terminus, up to 3 km upstream. This planar mesh is used to convert 3D stress into a 2D map of crevasse penetration.

Figure 5.7 illustrates the process of 'collapsing' the 3D stress state into the 2D

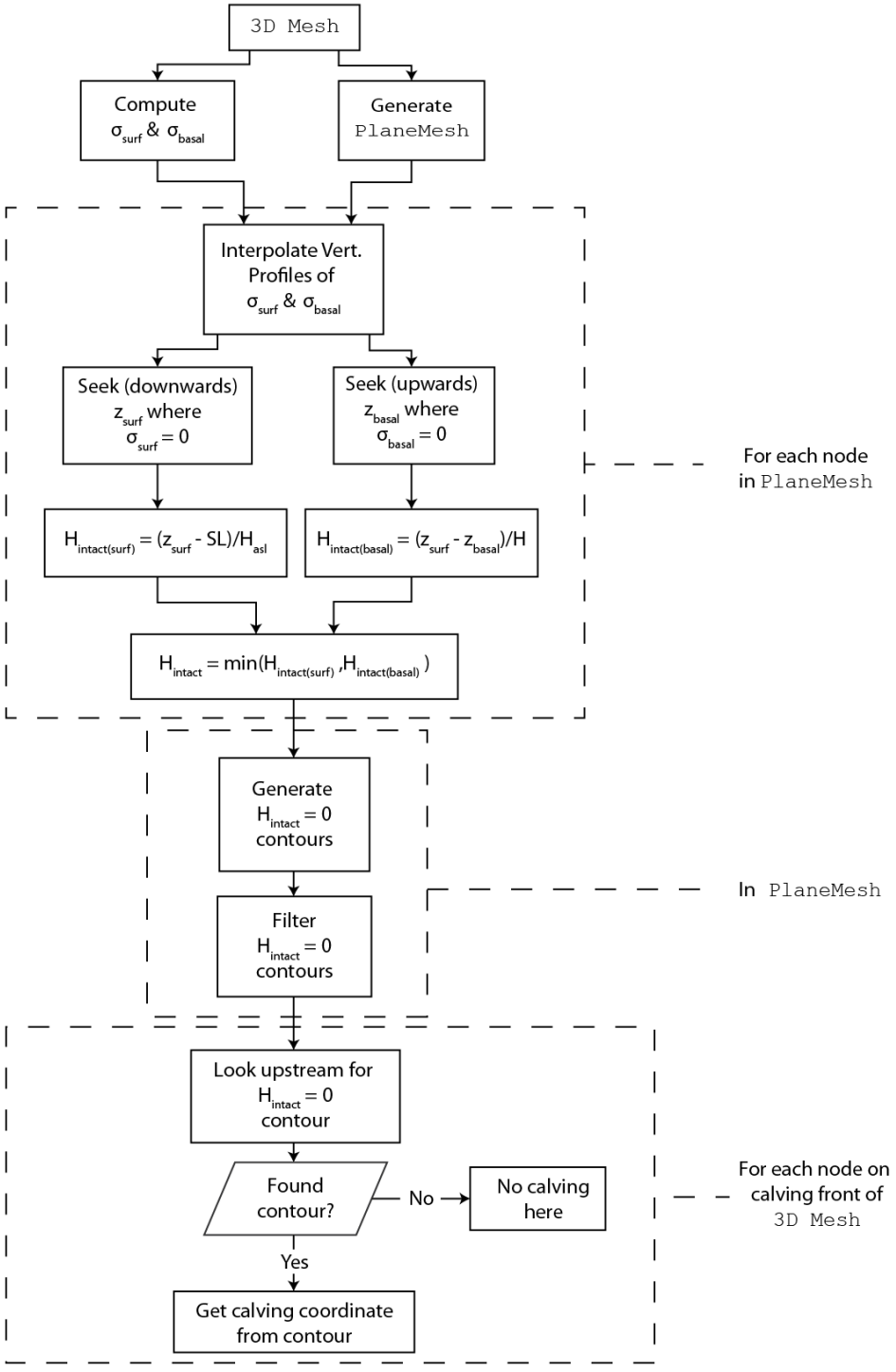

Figure 5.6: The full calving algorithm implemented in `Calving3D`

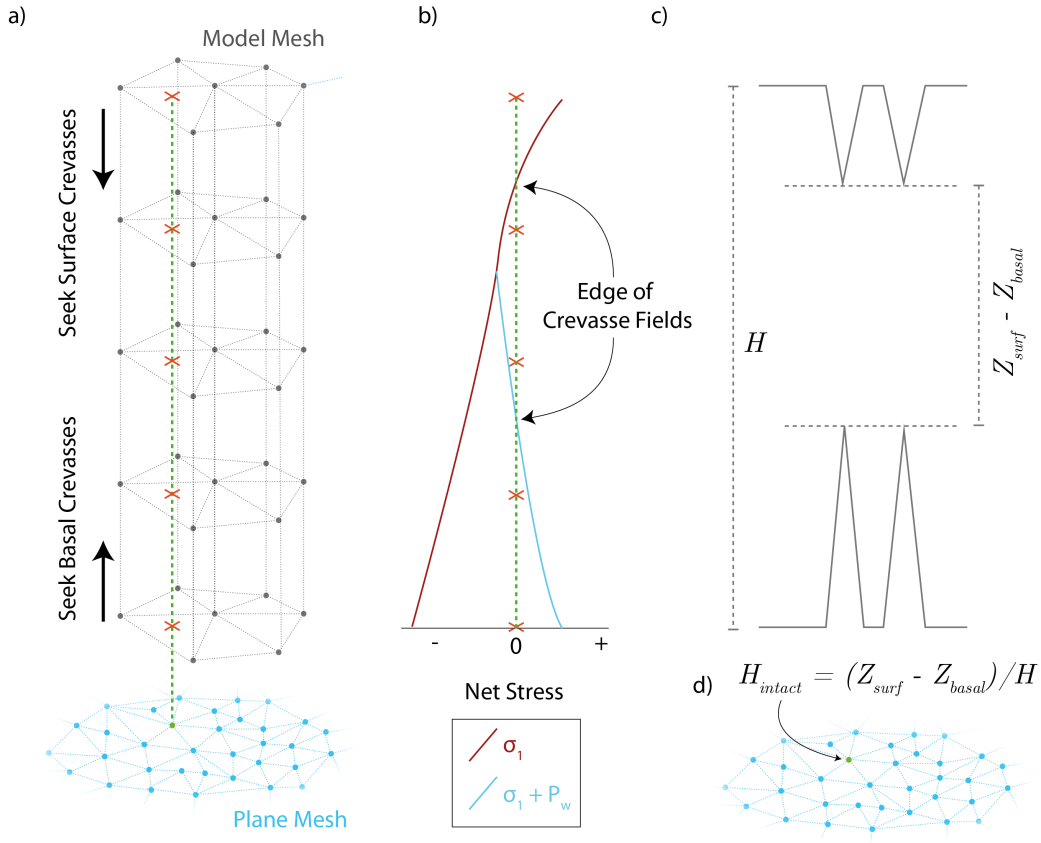

Figure 5.7: Schematic showing 3D calving algorithm. a) For each node in `PlaneMesh`, vertical intersections with 3D mesh are identified. b) Surface/basal crevasses exist to the depth/height where net stress is 0. c) The intact proportion (H_{intact}) is computed from the thickness and crevasse penetration and d) this is set on the relevant node of the `PlaneMesh`.

`PlaneMesh`, generating a map of crevasse penetration. This process corresponds to the first dashed box in Fig. 5.6, marked 'For each node in `PlaneMesh`'. Note that `PlaneMesh` is independent of the 3D model mesh, and so it is possible to choose a high mesh resolution, without impacting the performance of the other components of the model (e.g. `FlowSolve`). Furthermore, `PlaneMesh` is only required to extend inland beyond the distance where calving could conceivably occur. In the present investigation, I opt for a `PlaneMesh` that extends 3 km inland, with a resolution that varies from 30 m at the ice-ocean interface to 100 m at the inland edge.

The result of the process shown in Figure 5.7 is a 2D map of the crevasse penetration, denoted by the variable H_{intact}, which is equal to zero where crevasses

penetrate fully, and between 0 and 1 elsewhere. In the 2D model, the penetration of crevasses at a single point was sufficient for calving. However, in 3D, the penetration of crevasses at a single point is simply a moulin, and does not imply calving. Instead, it is necessary to identify uninterrupted regions of crevasse penetration in `PlaneMesh` which make contact with the ice-ocean interface. In other words, calving occurs if and where the $H_{intact} = 0$ contour makes contact with the ice-ocean interface at two points, isolating a region of ice from the rest of the terminus. For reasons outlined below, it was necessary to post-process the resulting $H_{intact} = 0$ contours to ensure that predicted calving events were physically plausible.

Following the identification of contour lines that delineate calving events, the final stage of the calving algorithm is to identify points on the calving front that lie within a region predicted to calve. Thus, for each 3D mesh node on the calving front, an upstream $H_{intact} = 0$ contour line is sought and, if found, the post-calving position of the node, which lies on this contour, is marked. For any node for which a corresponding post-calved position is found, the 'calving vector' is computed, which represents the displacement from the pre-calved position to the post-calved position. For nodes that do not calve, all components of this vector are zero. The calving vector is then passed to the remeshing algorithm (Section 5.8.2), which displaces the calving front before beginning the remeshing.

Ice Evacuation

Preliminary simulations indicated that simply requiring the $H_{intact} = 0$ contour to reach the front twice was an insufficient condition for predicting calving, as illustrated in Figure 5.8a. With this condition alone, large calving events were sometimes predicted when the actual crevasse penetration map indicated that such events were unphysical. Most commonly, a narrow band of full-depth crevasses would expand inland and open into a large wide region. In reality, the surrounding intact ice prevents the fully crevassed ice from being evacuated out into the fjord. Therefore, an additional step was added to the calving algorithm which checks that crevassed ice can indeed be evacuated before predicting a calving event. This ice evacuation test inspects each $H_{intact} = 0$ contour that meets the ice-ocean interface, and looks for constrictions like that shown in Figure 5.8a. Wherever a constriction exists, the contour is cut, preventing calving inland of

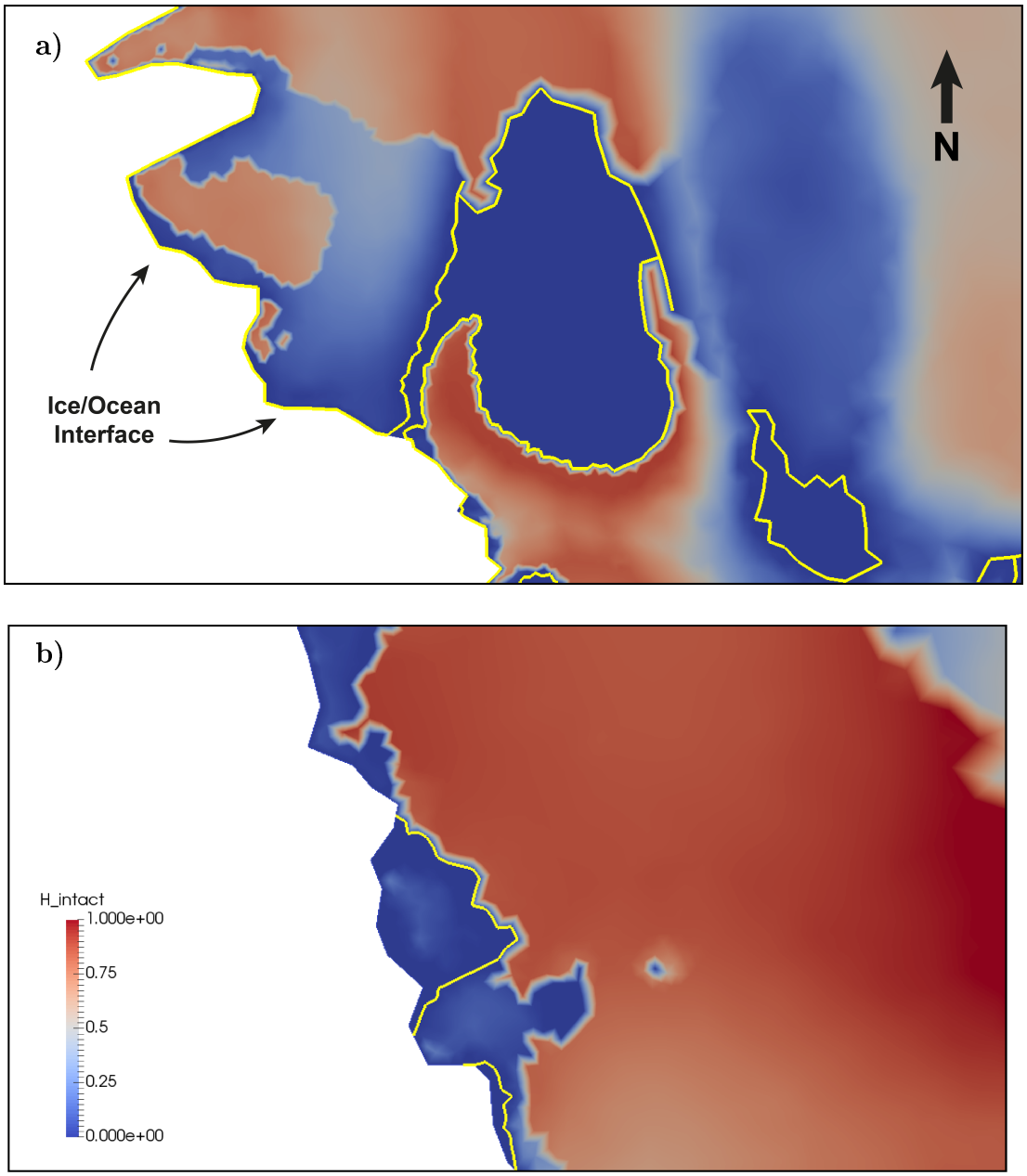

Figure 5.8: a) Full-depth crevassed ice incapable of evacuating: the large blue region behind the ice-ocean interface has full crevasse penetration throughout, and is thus enveloped by the $H_{intact} = 0$ contour (yellow line) which makes contact with the ice-ocean interface twice. However, the crevassed region where the contour makes contact with the ice-ocean interface is much narrower than the large fully crevassed region further inland, so the interior crevassed region cannot be evacuated, and so does not form a large calving event. **b)** Full-depth crevassed ice capable of evacuating: in this case, the fully crevassed ice is not constrained laterally, and so it all calves.

this point. The two calving events shown in Figure 5.8b are entirely capable of evacuating into the fjord, as they are not constrained by surrounding ice.

Ice-Ocean Interface Projectability

The current remeshing implementation (Section 5.8.2) requires that the ice-ocean interface remain projectable in some arbitrary coordinate system (chosen based on the orientation of the terminus). In other words, if the mesh is rotated such that the z-coordinate is roughly aligned to the direction of flow, the ice-ocean interface is not permitted to 'overlap' itself *in this coordinate system*. The effect that this projectability requirement has on the calving algorithm is that any ice which is downstream of a calving event is also calved. For example, if the 'narrow slit' in Figure 5.8a were not prevented from calving for the reason stated above, this calving event would take with it all the downstream ice (i.e. everything to the left of the slit).

On the whole, this requirement of projectability should not be a major limitation, as a consideration of stress and calving stability would suggest that *significant* overlap of this kind would be difficult for a real glacier terminus to sustain, although small overlap features are occasionally present in UAV imagery of Store's terminus. The implications of this requirement are discussed in more detail in Section 6.3.7.

Time-stepping

Calving events involve a change in terminus geometry which may affect the state of stress in the glacier. As such, it is often possible for a calving event to trigger subsequent calving by increasing crevasse penetration. These changes in stress regime can occur effectively instantaneously, following calving. However, in a typical time-evolving model, these secondary calving events would not be predicted until the next timestep, introducing an artificial delay in the calving rate. The *instantaneous* nature of this effect means that it cannot be solved by simply reducing the timestep size.

In order to overcome this limitation, a timestepping scheme was developed whereby, following a calving event, all the time dependent solvers (`FreeSurfaceSolver`, `Mesh Update`, `FrontAdvance3D`) are switched off, and the timestep size is set to a small value (1.0×10^{-10} years), allowing the flow solution and the calving cri-

terion to be recomputed until no more secondary calving events occur. Once secondary calving events cease, the timestep size is reset to its normal value.

This scheme performs well, but during testing it was noted that small calving events were often followed by other small events from different parts of the terminus. The small size and distance between these events suggested that these secondary events were, instead, a product of the remeshing algorithm (Section 5.8.2). By re-discretising the geometry and recomputing the flow solution, slight changes in the resulting stress field may lead to calving being predicted where previously the criterion was not quite met. This often led to series of more than 10 sets of 'secondary' calving events, meaning that the model takes a very long time to progress. Thus, it was decided to limit these pseudo-steady-state steps by imposing a minimum threshold on calving event volume. The rationale for this choice is that small calving events are unlikely to have a significant effect on the stress state of the remaining ice. I impose a calving event volume threshold of $1.0 \times 10^6\,\mathrm{m}^3$, and require an event larger than this to trigger a timestep pause.

5.8.2 Remeshing - `Remesh.F90`

In 2 dimensions, the geometry of calving events are sufficiently simple that the initial model mesh can simply be stretched or compressed in the direction of flow to accommodate the new shape (Section 3.6). However, in 3 dimensions, the development of headlands and embayments, as well as undercutting, mean that the model mesh quickly becomes 'degenerate' as the geometry evolves. Mesh degeneracy describes the displacement of nodes within a mesh to the extent that some of the elements begin to overlap, or become inside out (Fig. 5.9); when this occurs, the model equations can no longer be solved in this region and the simulation breaks down. Thus, in order to model a complex evolving geometry like a glacier terminus, remeshing is required.

A robust remeshing algorithm proved to be one of the most challenging components of the 3D calving model presented in this chapter. Not only was it necessary to generate a new mesh to fit the glacier geometry, but also to interpolate all the variable values from the old to the new mesh and recompute the various solver matrices. Furthermore, remeshing a given geometry is not guaranteed to produce a good quality mesh without degenerate elements; at times the combined processes of calving, submarine melting and advance due to ice flow

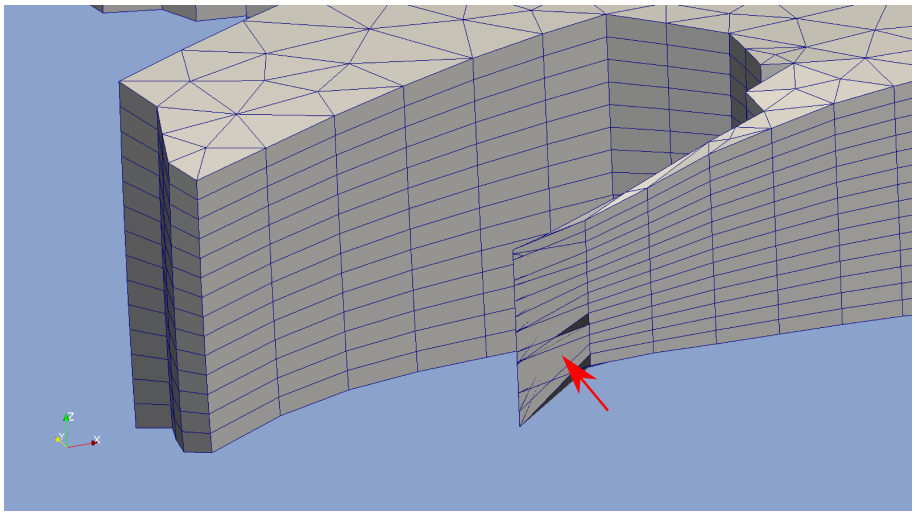

Figure 5.9: Due to changing terminus geometry, the elements indicated by the red arrow have become degenerate. Ice flow is from right to left.

resulted in terminus geometries for which no satisfactory mesh can be produced. For this reason, it was sometimes necessary to identify problematic regions of the mesh, and approximate the geometry in such regions, so that a good mesh could be produced.

Figure 5.10 outlines the full algorithm implemented in `Remesh.F90`, which produces a new mesh from the post-calving geometry at a given timestep, and interpolates the field variables from the old to the new mesh. Starting with the post-calving geometry, the first step is to identify a representative footprint of the existing 3D mesh. For the lateral and inflow margins, which remain vertical throughout the simulation, this process is trivial. However, for the calving front, which can deviate significantly from vertical due to melt undercutting and ice flow, it is necessary to identify an 'average' line that provides a best fit to the 3D terminus surface.

Once the footprint of the 3D mesh has been generated, nodes at the terminus which are closer than the target horizontal resolution are removed. This is important because without the filtering of close nodes, repeated remeshing would continue to increase the mesh resolution beyond the target resolution. The filtered mesh footprint is then written to a `GMSH` geometry file, which defines the shape of the domain to be meshed by GMSH, and an external call to `GMSH` produces a 2D footprint mesh of the glacier, which is converted into Elmer format using `ElmerGrid`. The 2D `FootprintMesh` is extruded vertically to the desired

number of vertical layers, equally spaced from 0 to 1 in the z-direction. I denote the resulting 3D mesh `NewMesh`. I extrude the mesh rather than directly meshing the 3D geometry to produce elements of the desired aspect ratio, as discussed in Section 5.2.

At this stage, I have the original mesh, `OldMesh`, which represents the current, post-calving geometry of the glacier, and `NewMesh`, a 3D mesh whose horizontal geometry matches `NewMesh`, aside from the vertical terminus, and which sits in the region $0 <= z <= 1$ in the vertical direction. To complete the remeshing requires that `NewMesh` be deformed to match `OldMesh`. However, it is mathematically simpler to instead compute the deformation which brings `OldMesh` into alignment with `NewMesh`, given the simpler geometry of the latter, and then apply the *reverse* deformation to `NewMesh`. Thus, I deform `OldMesh` in two stages, first to make the terminus vertical, and second to bring the mesh into $0 <= z <= 1$, saving the deformations as **deform_h** and **deform_v**, respectively. I then interpolate **deform_h** and **deform_v** from `OldMesh` to `NewMesh`, and apply the reverse of the interpolated deformations to `NewMesh`. The result of this process is a new 3D mesh that covers the domain of the previous mesh, but with improved mesh quality. Finally, all the field variables defined on `OldMesh` are interpolated onto `NewMesh` and the simulation can continue.

Preventing Mesh Degeneracy

Remeshing after calving events helps to prevent mesh degeneracy, but this is not guaranteed, especially when the front evolves to the point where it has become severely undercut by submarine melting. Because `NewMesh` is extruded from a 2D footprint, large subsequent deformations in the horizontal direction can lead to degeneracy. In practice, undercutting was found to cause problems when two node columns were closely spaced and one had a large horizontal range due to undercutting. For example, in the vicinity of a concentrated plume, a given column of nodes may be undercut by up to 300 m. I found that, if an adjacent column of nodes was closer than around 50 m from such a severely undercut column of nodes, this would quite consistently cause mesh degeneracy and cause the simulation to break down. To overcome this problem, the remeshing algorithm identifies 'severely undercut' columns of nodes, and enforces a slight coarsening of the mesh in this region. Coarser node spacing (i.e. larger elements) was found

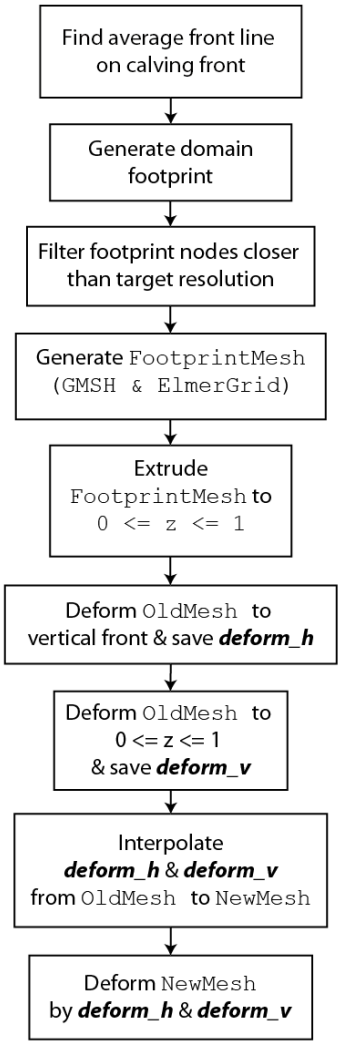

Figure 5.10: The remeshing algorithm

to be less likely to result in mesh degeneracy in such cases.

5.9 Model Forcing and Frontal Processes

One of the primary objectives of the 3D model was to improve our understanding of the processes that cause calving and link glacier dynamics to environmental processes and conditions, including atmospheric and oceanic climate. As discussed in Section 2.2.4, various processes are hypothesised to link calving and ice flow to changes in the atmosphere and ocean systems. The two principal processes investigated in this project are undercutting of the calving ice front by submarine melting and buttressing by proglacial ice mélange, both of which exhibit strong seasonal variability. In addition, I incorporate seasonal changes in basal traction, which drive seasonal variability in ice velocity. This section describes how environmental forcings are applied in the 3D model. The magnitude and duration of the forcings in the various simulations are described in Section 5.9.3.

Previous modelling studies (Cook et al., 2012; Nick et al., 2010) have suggested that the presence of water in surface crevasses can significantly influence calving rate. However, as discussed in Section 2.2.4, it is currently impossible to estimate the water depth in surface crevasses. Given that the aim of this study is to force a calving model with realistic, present day environmental forcings, I opt to focus on the quantifiable processes of submarine melting and ice mélange buttressing, and do not investigate water in surface crevasses.

5.9.1 Ice Mélange

Ice mélange is the rigid mixture of calved icebergs and sea ice that often forms in the winter months in front of calving glaciers in Greenlandic fjords (Amundson et al., 2010; Sohn et al., 1998). The presence and properties of ice mélange at Store Glacier are summarised in Section 1.3. Model forcing relating to ice mélange in 3D is identical to that in the 2D model, discussed in Chapter 3. The buttressing force of the mélange is simply applied as an external pressure boundary condition on the terminus, applied over the prescribed mélange thickness. I investigate the sensitivity of the model to various mélange thicknesses (Section 5.9.3); the 'present day' forcing consists of a strength of 385 kPa applied over a thickness of 140 m, based on observations from Store Glacier in 2014 (Toberg et al., 2016).

5.9.2 Submarine Melting

A significant advantage of moving from 2D to 3D is that it allows frontal melting to be realistically represented. In 2D, any imposed melt rate is implicitly laterally homogeneous. However, aerial photography from Store Glacier (Section 1.3) indicates the presence of concentrated conical plumes at locations where vigorous upwelling is driven by high, localized subglacial discharge into the fjord in summer. Indeed, direct observation of melt rates at Store (Chauché, 2016; O'Leary, 2011) shows that there is a large degree of horizontal variability due to these concentrated plumes.

In the 3D model, I split frontal melting into 'distributed plume' melt rate covering the entire submerged ice front, and 'concentrated plume' melting which melts the front at higher rates, but only at two discrete locations, where these concentrated plumes are persistently visible in imagery (Fig. 5.12). In reality, submarine melt patterns at Store are undoubtedly more nuanced than this, but this simplified approach allows us to partition the effects of distributed and concentrated melting more easily.

As described in Section 2.2.4, frontal melting at outlet glaciers is primarily driven by the outflow of buoyant meltwater at the base of the terminus, and this meltwater comes from two main sources: basal melting as a result of frictional heating due to basal sliding, and surface meltwater which drains through moulins to the bed. The former occurs year round, while the latter is confined to the summer months when the surface of the glacier melts. Both modelling (Rignot et al., 2016) and observations (Chauché, 2016) for Store Glacier indicate significant differences in front averaged melt rate between summer and winter, due primarily to the increase in subglacial meltwater flux.

In order to implement realistic melt profiles from distributed and concentrated plume melting, I use analytical plume models which were kindly provided by D. Slater and T. Cowton. These models, which run in a few seconds in MATLAB, numerically solve the Ordinary Differential Equations which describe the evolution of distributed planar and concentrated conical plumes (Cowton et al., 2015), given the salinity and temperature profiles of the fjord, also kindly provided by D. Slater and T. Cowton for Store's fjord.

The concentrated plume model generates conical plumes with a radius which increases linearly to a maximum at the surface of 150 m (Fig. 5.12a). I impose

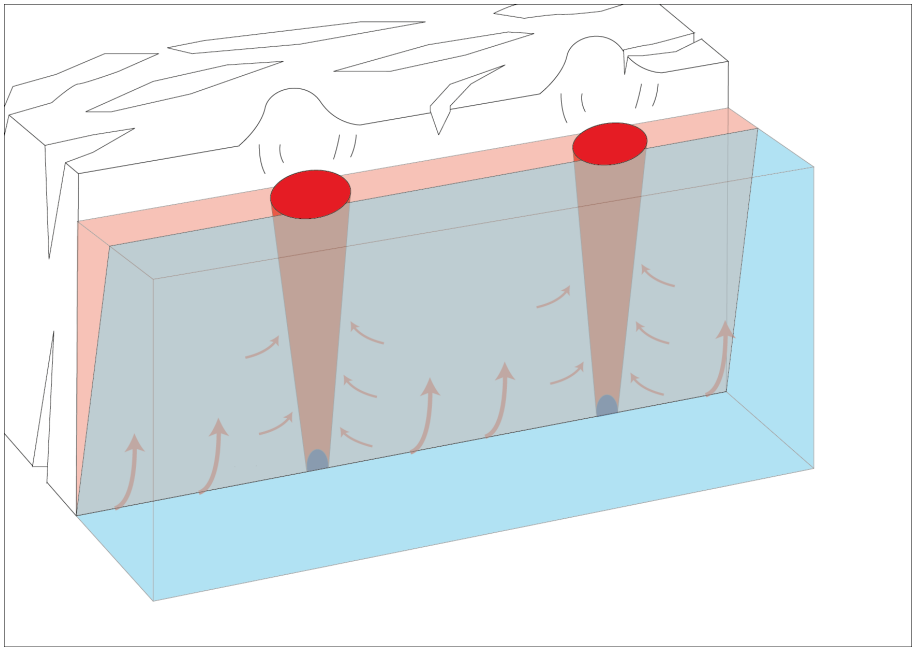

Figure 5.11: Plume implementation in the 3D model. I simplify complex melt patterns into a combination of two end members: planar and conical plumes.

two such plumes in the model, which therefore affect less than 3% of the total surface area of the ice-ocean interface. Thus, although melt rates in the concentrated conical plumes are higher (O'Leary, 2011), their narrow width means that the vast majority of total melting occurs due to the distributed planar melting (Slater et al., 2015). The negligible contribution of concentrated plumes to total submarine melting indicates that the observed increase in submarine melt in summer (Chauché, 2016) must be almost entirely due to an increase in the *distributed* submarine melt rate. For this reason, I make the simplifying assumption that distributed melting is *entirely* responsible for observed average melt rates in winter and summer.

To determine the vertical melt profile of the distributed plume, I specify a target average submarine melt rate consistent with modelling and observational data (Section 5.9.3) for both summer and winter, and then run the MATLAB script with varying subglacial discharge until the target frontal average melt rate is achieved. I then export the resulting vertical melt profile and apply this at the ice-ocean interface in the model.

The conical plume profile cannot be derived from front averaged submarine melt rates, for the reasons outlined above; instead I use direct observations of in-

plume maximum melt rates from Chauché, (2016). I run the conical plume model until obtaining the conical plume profile which matches the target maximum. While the planar plume is described uniquely by a melt profile through depth, the conical plume also has a width profile. Given this width, I assume that the melt rate decays as a Gaussian curve from the centreline outwards (Turner, 1973):

$$\dot{m} = \dot{m}_{x=0} e^{-(x/W)^2} \tag{5.28}$$

where x is the horizontal distance from the centre of the plume and W is the width the of the plume at the given elevation.

The conical and planar plume profiles for Experiment 1 are shown in Figure 5.12, alongside a map of the terminus showing the location of the two persistent conical plumes. For simplicity I assume an instantaneous switch from winter to summer melting. Conical plume melting is assumed to be present during the summer months.

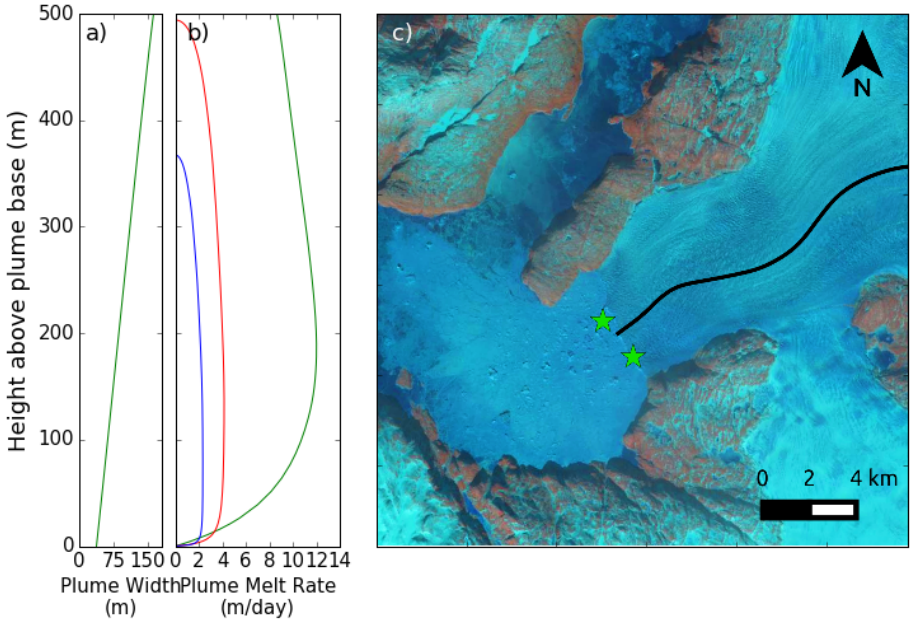

Figure 5.12: a) Vertical profile of conical plume width. b) Melt profiles for concentrated plumes (green), and distributed plumes in summer (red) and winter (blue). c) Location of the two persistent concentrated conical plumes observed at Store Glacier.

Melt & Terminus Geometry

Figure 5.12 shows that the predicted plume melt rates reach a maximum value at some point relatively near, but not at, the base. Below this point, the plume has, presumably, had insufficient time to entrain warm saline fjord water, and so consists largely of cold, fresh meltwater, inhibiting its ability to melt the terminus. The effect of this melt profile on the terminus geometry over time is to produce a front which is undercut, but with small, sharp 'toes' remaining at the base. These toes are real features (Motyka, 1997; Warren et al., 1995) known to calve suddenly due to the buoyant force acting on them. However, the calving mechanism incorporated into Elmer/Ice in this study works with vertically integrated crevasse depths (Fig. 5.7), requiring that crevasses penetrate the *full thickness* of the ice for calving to occur. Of course, in reality, it would be sufficient for crevasses to penetrate the full thickness of a calving toe, but the current model implementation is unable to make this distinction, such that calving of a toe cannot occur unless the overlying subaerial portion of the front also calves. As a result, these toes were found to be unrealistically stable in the model, growing in length until they caused mesh degeneracy and model breakdown. To avoid this issue, I add a 'toe calving' term to the melt rate which ensures that the maximum melt rate applies down from the observed maximum to the base of the terminus. I keep track of this implicit 'toe calving' rate separately from the actual imposed melt and calving events predicted by the calving algorithm.

Basal Melting

In addition to submarine melting of the vertical calving front, I also impose melting underneath the floating portion of the terminus. As in the 2D model, I simply take the maximum *frontal* submarine melt rate, and apply basal melting at 10% of this value. This is consistent with the work of Jenkins, (2011), who analysed the change in submarine melt rate with respect to the angle of the ice/ocean interface.

In reality, basal melting also occurs underneath grounded ice. However, I chose not to model this effect, as the two are fundamentally different processes. Melting underneath grounded ice is a result of basal friction as the ice flows over the bed. Basal melting underneath floating ice, on the other hand, is controlled by fjord circulation and subglacial discharge. This is a frontal process which is

closely linked to frontal submarine melting, and so for consistency, I include it in my analysis.

5.9.3 Experimental Design

As with the 2D model (Chapter 3), I apply the 3D calving model to two distinct sets of experiments. In Experiment 1 I run the time-evolving calving model with environmental forcings which are representative of present day conditions at Store Glacier. Experiment 2 forms a sensitivity analysis through which I investigate the model's response to changes in the applied environmental forcings. I perturb these environmental forcings in a manner consistent with a warming climate, to investigate how climate change may affect Store Glacier's calving behaviour and stability.

I begin by spinning up the ice flow model for 300 years, without calving, to allow the model to obtain a steady-state. During this 300 year spinup, I impose seasonally variable basal drag to reproduce the observed seasonal velocity cycle, as described in Section 5.7. I then carry out the Experiment 1 simulations from the end of this 300 year spinup. Experiment 2 simulations start from the end of the most realistic scenario obtained in Experiment 1 simulation (Run 111, Table 5.1). I do not simulate calving during the spin-up phase because the temporal resolution required to do so is prohibitive.

Experiment 1

The aim of Experiment 1 is two-fold. Firstly, by incorporating ice-ocean interactions tied to present day climate, I can compare the model results to observations from Store, allowing us to effectively validate the model. Secondly, with a good agreement between model and observations, the model allows us to determine the climate processes which are responsible for observed seasonal behaviour of the glacier, thus improving our understanding of calving and environmental stimuli tied to changes in ocean and/or atmospheric conditions.

I run four combinations of the three forcing parameters: ice mélange buttressing, distributed melting and concentrated melting (Table 5.1). In the 2D experiments, ice mélange thickness came from IceBridge data (`https://espo.nasa.gov/missions/oib/`), while strength estimates came from Walter et al., (2012). However, since the completion of the 2D experiments, a field campaign

carried out by researchers at the Scott Polar Research Institute, in collaboration with Aberyswyth University, has produced a large quantity of high spatial and temporal resolution data about Store Glacier's calving behaviour and ice mélange properties. Mélange was found to have an average thickness of 140 m; the buttressing force exerted on the terminus was estimated, using force balance, at 120 kPa. In Experiment 1, I use these values, and apply the mélange forcing from 1st February to 29th May (Julian Day 149) each year, based on the observations of Howat et al., (2010).

I apply submarine melting from a combination of distributed and concentrated plumes as described in Section 5.9.2. I use mean frontal melt rates of $3.1\,\mathrm{m\,d^{-1}}$ and $1.3\,\mathrm{m\,d^{-1}}$ for summer and winter, respectively, to constrain the distributed plume model. These values are consistent with a recent modelling study of Store's submarine melting by Rignot et al., (2016). The concentrated conical plumes which are active in the model in summer are constrained by a maximum in-plume melt rate of $12\,\mathrm{m\,d^{-1}}$ as observed by Chauché, (2016).

Experiment 2

In Experiment 2, I investigate the model's sensitivity to changes in the magnitude and seasonal duration of environmental forcings applied in Experiment 1. I scale the magnitude and duration in a manner consistent with a warming climate; Store Glacier has maintained a stable terminus position for the past decade (Howat et al., 2010), and so to investigate potential sources of instability requires a destabilising climate influence. I do not attempt to specify the likely *magnitude* of climate change in the 21st century, as that is beyond the scope of this study, and I emphasise that the simulations are diagnostic rather than prognostic. Instead, I apply stepped changes to the magnitude and duration of ice mélange buttressing and submarine melting, consistent with the ongoing trend of the warming climate, as well as modifying basal slip. Because the model is the first 3D full-Stokes calving model, I deliberately focus on the model's sensitivity to changes in the glacier's primary environmental forcings.

In terms of melt magnitude, I modify both distributed planar and concentrated plume melt rates by a factor of 1.5 and 2. For the planar plume, this involves scaling the target average melt rate (Section 5.9.2) and rerunning the planar plume model to produce new melt profiles. For conical plume melting, I

found it difficult to achieve the desired scaling with the conical plume model, due to the nonlinear relationship between subglacial discharge and melt rate. Thus, I instead directly scale the conical plume melt profile from Experiment 1 (Fig. 5.12).

For ice mélange, I investigate the effect of scaling its thickness by 0.5 and 0 (i.e. absent mélange). For basal slip, I investigate the effect of scaling the basal slip parameter uniformly by 0.9 and 0.8.

To investigate the effect of varying forcing durations, I concurrently scale the ice mélange and melt seasons first by 1 month and then by 2 months. As I focus specifically on changes tied to global warming, I increase the length of the melt season while *decreasing* the length of the mélange season. These changes are applied symmetrically; in other words, when increasing the melt season by 1 month, I achieve this by adding half a month on each end of the season, and simultaneously decrease the mélange season by half a month at each end. I do not investigate changes in season length with respect to basal slip, because there is no reasonable approach by which to do so with this model; basal slip does not simply decrease in summer and increase in winter, and so there is no simple strategy to extend the 'summer' basal slip season.

Table 5.1 outlines the simulations performed as part of Experiment 2, and their environmental forcings.

	Ice Mélange			Submarine Melt					Basal Slip
Run Code	Thickness (m)	Formation	Collapse	Dist. Summer Ave ($m\,d^{-1}$)	Dist. Winter Ave ($m\,d^{-1}$)	Conc. Max ($m\,d^{-1}$)	Summer Start	Summer End	β factor
Exp1									
000	0	-	-	0	0	0	-	-	1
010	0	-	-	3.1	1.3	0	1st June	31st Aug	1
011	0	-	-	3.1	1.3	12	1st June	31st Aug	1
111	140	1st Feb	29th May	3.1	1.3	12	1st June	31st Aug	1
Exp2 – Mag									
CONTROL	140	1st Feb	29th May	3.1	1.3	12	1st June	31st Aug	1
MM1	70	1st Feb	29th May	3.1	1.3	12	1st June	31st Aug	1
MM2	0	-	-	3.1	1.3	12	1st June	31st Aug	1
MD1	140	1st Feb	29th May	4.65	1.95	12	1st June	31st Aug	1
MD2	140	1st Feb	29th May	6.2	2.6	12	1st June	31st Aug	1
MC1	140	1st Feb	29th May	3.1	1.3	18	1st June	31st Aug	1
MC2	140	1st Feb	29th May	3.1	1.3	24	1st June	31st Aug	1
MA1	70	1st Feb	29th May	4.65	1.95	18	1st June	31st Aug	1
MA2	0	-	-	6.2	2.6	24	1st June	31st Aug	1
Exp2 – Dur									
D1	140	15th Feb	14th May	3.1	1.3	12	17th May	15th Sept	1
D2	140	2nd March	29th April	3.1	1.3	12	2nd May	30th Sept	1
DM1	70	15th Feb	14th May	4.65	1.95	18	17th May	15th Sept	1
DM2	0	-	-	6.2	2.6	24	2nd May	30th Sept	1
Exp2 – Bas									
B09	140	1st Feb	29th May	3.1	1.3	12	1st June	31st Aug	0.9
B08	140	1st Feb	29th May	3.1	1.3	12	1st June	31st Aug	0.8

Table 5.1: Experiment 1 & 2 Simulations. Experiment 2 simulations are split into magnitude, duration and basal slip perturbations, and are assigned codes for brevity: the first letter distinguishes between (M)agnitude, (D)uration or (B)asal drag simulations. For magnitude simulations, the second letter distinguishes between (M)élange, (D)istributed melt, (C)oncentrated melt or (A)ll forcings. Duration simulations are either duration only (D) or duration and magnitude combined (DM). For magnitude and duration, the digit refers to either the 1st or 2nd perturbation, where the 2nd is more 'severe'. Green highlights the parameter values which deviate from the control simulation (i.e. the active perturbation).

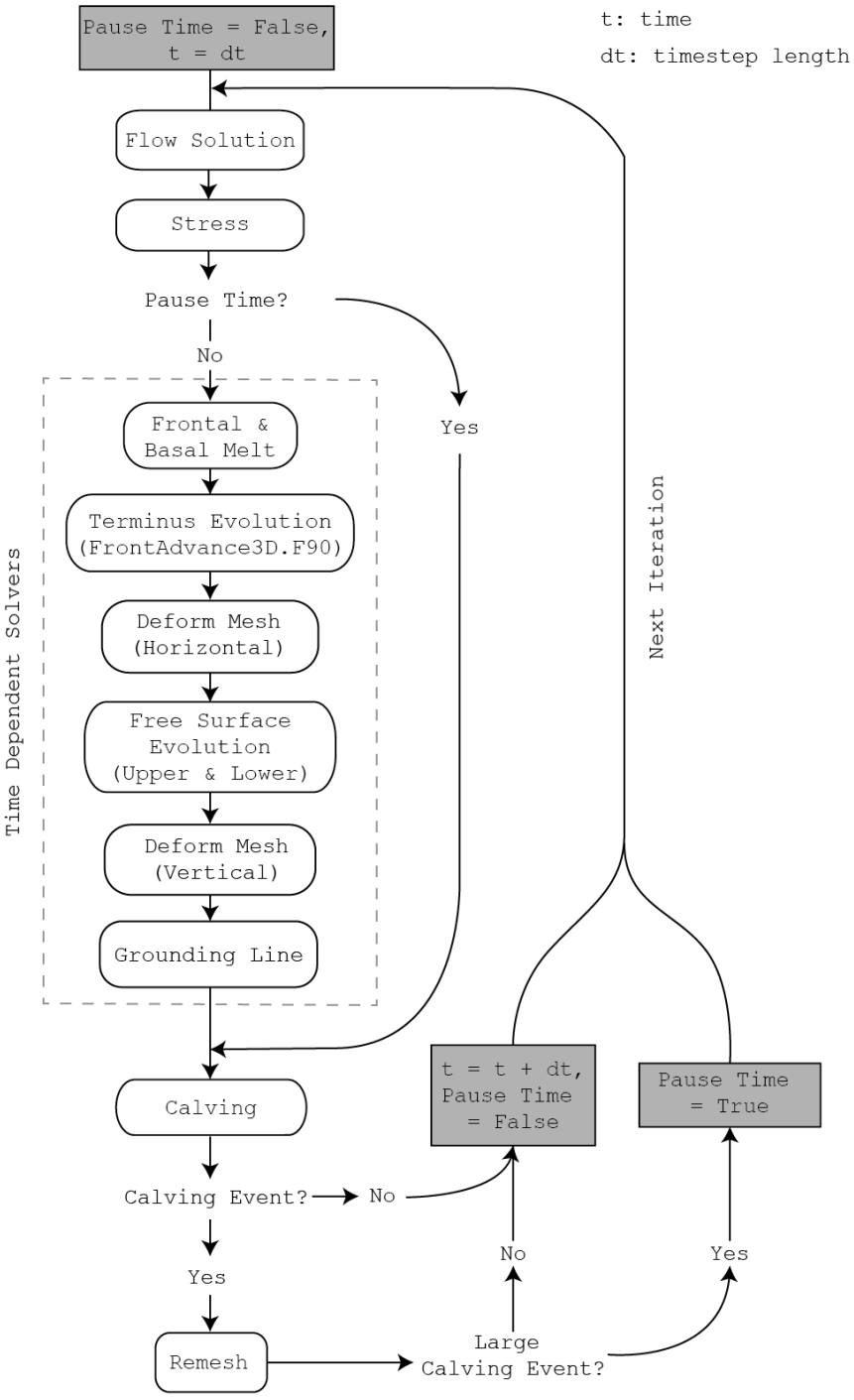

Figure 5.13: 3D Model Implementation

CHAPTER 6

THE 3D MODEL: RESULTS & DISCUSSION

This chapter presents and discusses the results of the 3D calving model applied to Store Glacier. Section 6.1 presents the results of the Experiment 1 'present climate' simulations, while Section 6.2 describes the outcomes of Experiment 2, the sensitivity analysis. Finally, Section 6.3 analyses and discusses the outcomes of both experiments, and draws conclusions about Store Glacier's seasonal evolution, its sensitivity to climate and the performance of the 3D model as a whole.

6.1 Results: Experiment 1 - Present Climate

As outlined in Chapter 5, I investigate the effects of seasonally varying basal slip, changes in the magnitude and distribution of frontal submarine melting, and the buttressing effect of ice mélange. I present results from simulations with and without the submarine melt and ice mélange forcings, in order to better isolate these processes. For brevity and clarity, the simulations in this section are referred to by a 3 digit code (e.g. '011'), where the first digit indicates the presence or absence of ice mélange, the second indicates distributed submarine melting, and the third signifies concentrated submarine melting. Thus, simulation '010' has only distributed melting applied.

All of the simulations are forced with seasonally varying basal slip. This is because the simulation is first spun up to a steady state (Section 5.7) before the calving model is applied, and this spin-up includes the seasonally varying basal slip. Therefore, to then *remove* the seasonality of the basal slip would result in an immediate divergence from the achieved steady-state, rendering the results unrealistic and uninformative. However, the results of Experiment 2 (Section 6.2)

include changes in basal slip which might accompany a warming climate.

Section 6.1.1 presents crevasse fields as predicted by the model, and Section 6.1.2 discusses the buoyant forces which arise as the glacier flows into the proglacial water body. These sections provide the glaciological context onto which the frontal processes of submarine melting and ice mélange buttressing are imposed in Experiment 1. Section 6.1.3 shows the seasonal patterns of terminus position and velocity which arise from the 4 Experiment 1 forcing scenarios, and Section 6.1.4 investigates these seasonal patterns further by exploring the characteristics of calving events, and their spatial and temporal distribution. Finally, Section 6.1.5 considers the evolution of the glacier terminus through time in terms of mass balance, the balance between the flow of ice towards the terminus and the loss of ice through calving and melting.

6.1.1 Crevasse Depth

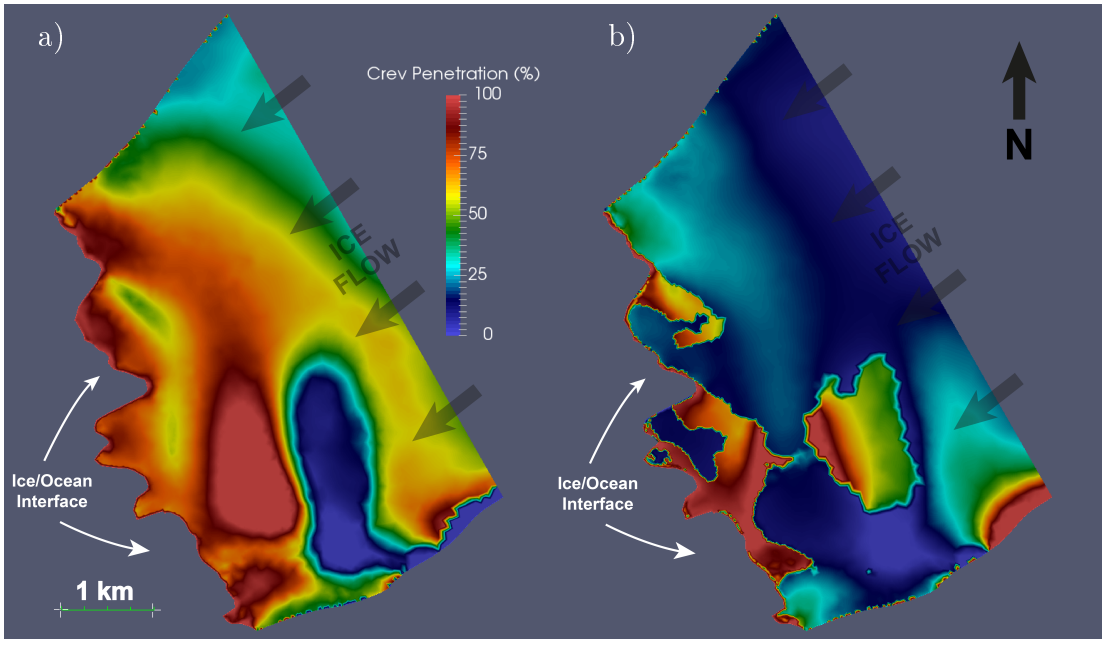

Figure 6.1: Crevasse penetration for a) surface and b) basal crevasse models. The two models show distinctly different patterns; while the surface crevasse field displays generally smooth transitions from shallow to deeper crevasses, the basal crevasse field is punctuated by sharp regions of almost intact ice. The calving model (`Calving3D`) uses the maximum penetration from the two models for each point when detecting calving.

Figure 6.1 shows typical crevasse penetration for both the surface crevasse

model and the basal crevasse model. In the surface crevasse model (Fig. 6.1a), the crevasse penetration percentage is from surface to sea level, at which point the model predicts calving. For the basal crevasse model (Fig. 6.1b), the percentage indicates how far through the entire glacier thickness surface and basal crevasses penetrate. Given that basal crevasses are typically larger than those at the surface, Figure 6.1b is largely an indicator of basal crevasse penetration.

In the surface crevasse field, there is a general trend of increasing crevasse depth towards the terminus, as is to be expected. Surface crevasse depth typically varies smoothly, especially compared with the pattern of basal crevasse penetration. The southern side of the terminus is dominated by a region of complete crevasse penetration, slightly inland from the terminus, followed by a region of extremely shallow crevasses just upstream. The coincidence of these two features, and their similar extent, suggests that they may be controlled by the same underlying process. This will be explored further in the discussion.

Basal crevasse maps show a distinctive pattern of rapidly changing crevasse field depth (Fig. 6.1b), unlike the surface crevasse field. Interestingly, the basal crevasse field appears to be composed of two components: for the majority of the front, basal crevasse penetration is very low and so the ice is largely intact. In regions near the terminus, there is a sharp boundary to much greater crevasse penetration, which has a pattern that is broadly similar to surface crevasse penetration.

6.1.2 Grounding Line & Buoyancy

Store Glacier, like most outlet glaciers in Greenland, flows into a marine fjord and, as the glacier flows into the proglacial water body, it experiences significant hydrostatic pressure. This buoyant force acting on the base of the glacier can reach or exceed the ice overburden pressure, leading to flotation. Figure 6.2 illustrates the variability in buoyant forces across the terminus of Store Glacier as predicted by the model, during the ice mélange season for the 'full forcing' run, as well as the grounding line. The grounding line is significantly inland of the front on the south side of the terminus. The north side of the terminus, on the other hand, is almost entirely grounded. The variable denoted as 'Hydrostatic

Imbalance' is defined on the base of the glacier, and is equal to:

$$\frac{-z_b/H}{\rho_i/\rho_{sw}} - 1 \tag{6.1}$$

where ρ_i and ρ_{sw} is the density of ice and sea water, respectively, z_b is the elevation of the bed relative to sea level, and H is the thickness of the ice column. This provides a measure of how far the glacier deviates locally from hydrostatic equilibrium. Positive values indicate that the glacier is resting above the elevation of free floating ice, while negative values indicate that the ice is below the elevation of neutral buoyancy, a state referred to as 'superbuoyancy'. In other words, ice which is 'superbuoyant' is being held underwater by non-local forces.

Most of the ice near the terminus is grounded, and so it has a positive hydrostatic imbalance. However, the pattern of hydrostatic imbalance in the floating region to the south make it clear that flotation does not necessarily imply hydrostatic equilibrium. Instead, just downstream of the grounding line, ice is above neutral buoyancy, while the ice towards the middle of the floating cavity is below hydrostatic equilibrium, and so is superbuoyant. This pattern is due to the bedrock topography: the grounding line in the south side of the terminus is located on the lee side of a large bedrock obstacle, beyond which the bedrock elevation descends rapidly (Fig. 1.3). Thus, as the ice flows past the grounding line towards the terminus, it descends rapidly, passing the level of neutral buoyancy. The velocity of the ice here, and the lateral drag from the surrounding grounded ice, prevent it from immediately adjusting upwards to neutral buoyancy. Instead, as it continues to flow away from the grounding line, the leverage exerted by hydrostatic pressure around the pivot at the grounding line increases, raising the ice near the grounding line above neutral buoyancy.

The relationship between the modelled calving behaviour and buoyant forces is discussed in Section 6.3.6. Briefly, the large region of low surface crevasse penetration in Fig. 6.1a is a manifestation of the upward bending moment discussed above. As the distance from the grounding line increases, so too does the upward force exerted by the proglacial water body, generating a bending moment which pivots at the grounding line, generating compressional forces at the surface and inhibiting surface crevasse growth.

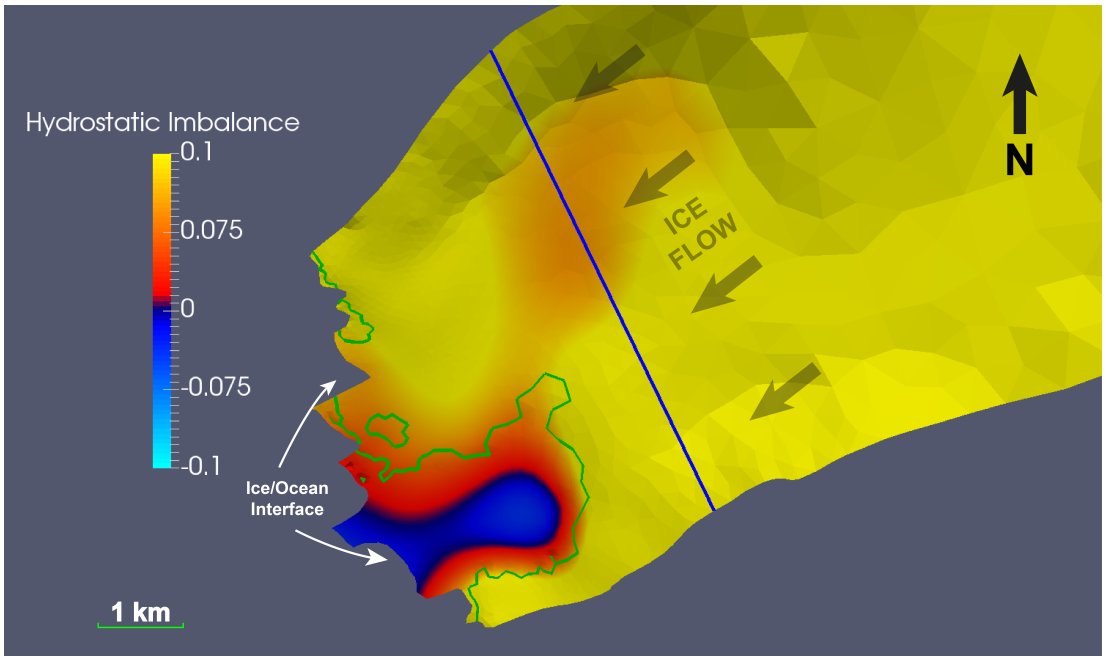

Figure 6.2: Plan view of Store Glacier model showing the hydrostatic imbalance near the terminus. Hydrostatic imbalance (Eq. 6.1) is defined as the deviation, in terms of buoyant forces, from free floating ice in hydrostatic equilibrium. Positive values (red to yellow) indicate that the ice is *above* the height which would result from hydrostatic equilibrium, while negative values (blue to white) imply that the ice is sitting *below* hydrostatic equilibrium. The grounding line is shown in green. The blue line shows the location of the flux gate used to compute influx and volume in this chapter.

6.1.3 Seasonal Terminus Position & Velocity

Figure 6.3 shows the mean terminus position and velocity for four combinations of frontal forcing.

In Run 000, the only seasonal forcing applied is basal slip; ice mélange and submarine melting are absent. There is a clear seasonal signal in the terminus velocity (Fig. 6.3b), which peaks in early summer at 5100 m a^{-1}, before a deceleration through late summer to an annual minimum of 4200 m a^{-1}. Following this late-summer minimum, the velocity steadily increases through the winter. This seasonal velocity cycle is maintained through several years of simulation, despite significant and seemingly stochastic evolution of terminus position (Fig. 6.3a). The total range in terminus position over the period is 800 m, but there is no seasonal signal in the terminus position.

When distributed submarine melting is applied (Run 010), the seasonal evolu-

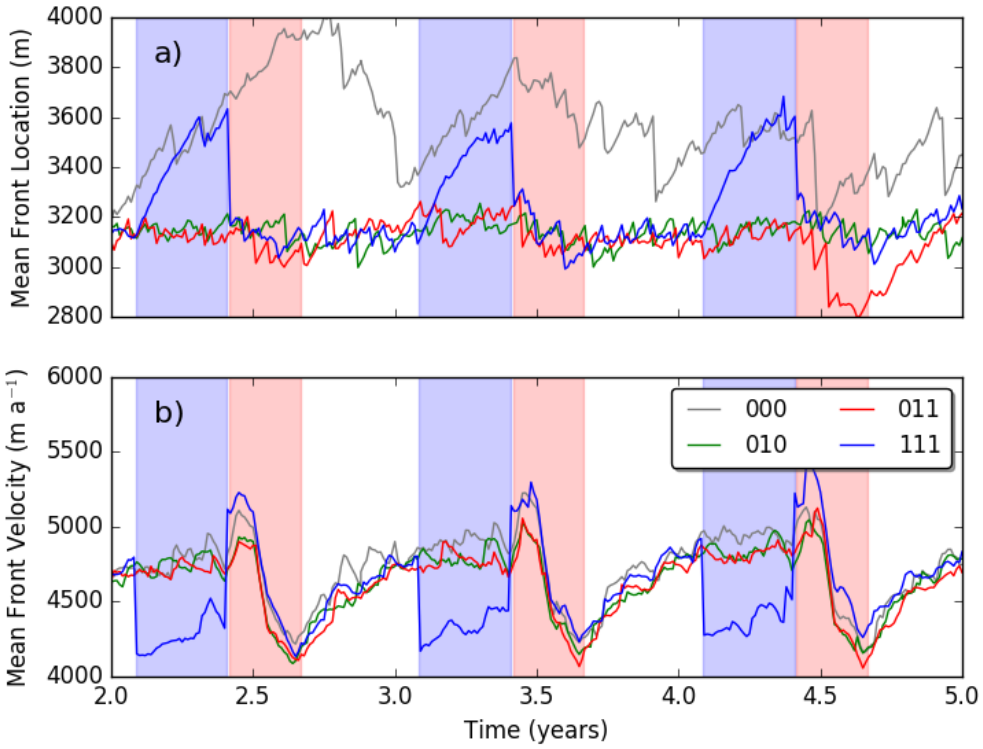

Figure 6.3: Mean terminus position (a) and velocity (b) for the four forcing combinations. Front 'position' is relative to the flux gate shown in Fig. 6.2. Blue and red shading indicate the mélange buttressing and summer melt seasons, respectively.

tion of terminus position is significantly different from Run 000. The total range in terminus position is reduced to around 200 m, and it displays a subtle seasonal cycle, reaching a maximum before the onset of summer melting, and retreating slowly over the course of the summer, before gradually advancing after the summer melt season. There is little difference in the terminus velocity compared to the 'no forcing' case, despite the significant difference in the position of the terminus.

The addition of concentrated melting from conical plumes (Run 011) amplifies the seasonal response of the glacier to submarine melting. Most notably, in the final year of the simulation, the mean front position retreats more than 400 m, well behind the position otherwise observed in any of the simulations. The velocity shows no systematic deviation from that of the distributed melt simulation.

When all three forcings are applied (Run 111), the pattern of terminus advance and retreat becomes distinctly seasonal. This seasonality is primarily a

consequence of the introduction of buttressing stress from proglacial ice mélange. Immediately following the formation of the mélange, the terminus advances into the fjord. On average, the front advances 500 m into the fjord during winter, before retreating almost immediately when the mélange collapses. In addition to its effect on front position, the ice mélange also exerts an instantaneous effect on the velocity at the terminus (Fig. 6.3b). When the mélange forms in February, the terminus rapidly decelerates by around 400-600 $\mathrm{m\,a^{-1}}$, and at the end of May, when the mélange collapses, there is an equivalent acceleration of the terminus. This pattern of advance and retreat and the concurrent deceleration and acceleration is notably absent from the model runs without mélange.

6.1.4 Calving Behaviour

To investigate the spatial and temporal distribution of calving events, Figure 6.4 shows the location, volume and season of individual calving events for the entire 5 year simulation (right panels) and the evolution of the terminus position through a single year (left panels). In all 4 simulations, there is a tendency for the largest calving events to occur towards the south of the terminus, in the region which is floating (Fig. 6.2). This southern floating region is also where the largest changes in front position over time occur.

The 'no forcing' simulation (Fig. 6.4a) produces a 3 km long floating ice tongue on the south, whereas the northern part of the terminus remains fairly fixed. With no external forcing acting on the calving front, the floating tongue remains stable and does not fully collapse for the entire 5 years of the simulation. The somewhat unphysically straight southern edge of this floating tongue is an artefact of the model implementation, which is discussed in Section 6.3.7.

Calving event size varies significantly across the terminus, with the largest bergs ($4.9 \times 10^8\,\mathrm{m^3}$) being released from the floating tongue. There is also a general trend, across the front, of larger icebergs occurring further to the southwest (i.e. front advanced), while those further upstream are predominantly small.

When distributed submarine melting is applied (Fig. 6.4b), the floating tongue does not form, and the terminus position is much less dynamic than the 'no forcing' run. There are significantly fewer large calving events, the largest ($2.4 \times 10^8\,\mathrm{m^3}$) being around half the size of the largest in the 000 run ($4.9 \times 10^8\,\mathrm{m^3}$). Again, the largest calving events are predominantly in the south-

ern half of the terminus.

In Run 011, which includes concentrated as well as distributed melting (Fig. 6.4c), the southern region of the terminus retreats around 500 m compared to the distributed melt-only simulation (Run 010), indicating that concentrated melting from conical plumes is capable of exerting significant influence on calving rate and terminus stability. The maximum ($2.95 \times 10^8\,m^3$) and mean ($1.65 \times 10^6\,m^3$) berg volumes are slightly greater than the distributed melt-only case, highlighting the ability of concentrated melting to promote calving.

The addition of ice mélange buttressing in Run 111 (Fig. 6.4d) promotes a strong seasonal signal in terminus position. The bright pink colour which marks the mélange season is quite consistently further advanced than the rest of the year. In this simulation, too, frontal melting appears to promote retreat in summer (light blue colours), though this is not as pronounced as when ice mélange is absent.

Because the backstress from ice mélange promotes the growth of a large floating tongue, the full forcing simulation also produces the largest calving events by a significant margin (Table 6.1). The five largest of these all occur within a 1 km region of the front, at the end of May each year. These are the large tabular bergs (4.62×10^8-$1.27 \times 10^9\,m^3$) which occur immediately following the collapse of the ice mélange each year, as illustrated in Figure 6.8d. The largest of these (Year 1) was 1.58 km long, and is shown in Figure 6.7.

Figure 6.5 shows the frequency distribution of iceberg volume as well as the total volume lost from icebergs of the corresponding size for Run 111, while Figure 6.6 compares all four Experiment 1 simulations using a probability density function. Table 6.1 shows the maximum, mean and standard deviation for iceberg volume for the Experiment 1 simulations. Iceberg volume from Run 111 shows a bimodal distribution (Fig. 6.5), with peaks at $1.0 \times 10^{-2}\,m^3$ and $1.0 \times 10^6\,m^3$. Just under half of the 32 Gt lost from calving in the 111 simulation was calved as bergs between 1×10^6-$1 \times 10^7\,m^3$. These calving events were also the most common, accounting for just under half of all icebergs released. A significant proportion of mass loss comes from larger bergs; the five largest bergs were released annually following ice mélange collapse, ranging in size from 4.62×10^8-$1.27 \times 10^9\,m^3$. These five bergs equate to 3.54 Gt mass loss between them, 11% of the total calving loss for the simulation.

The small volumes of the lower peak render them physically insignificant; these

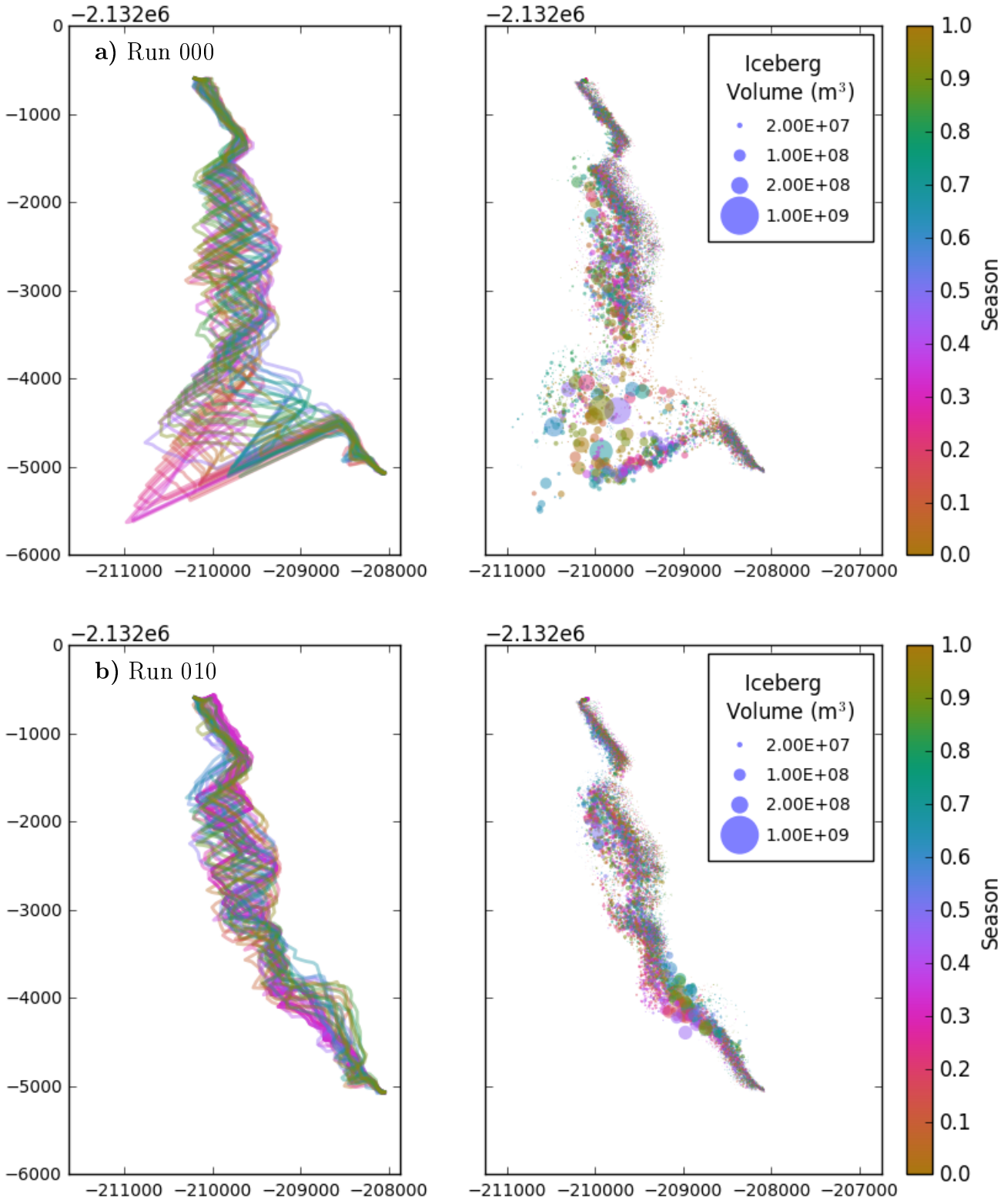

Figure 6.4: Seasonal terminus position through one year (left) and calving event locations and season for all 5 years (right) for the 4 forcing combinations: a) Run 000 b) Run 010 c) Run 011 d) Run 111. Green stars in (c) indicate locations of concentrated plumes.

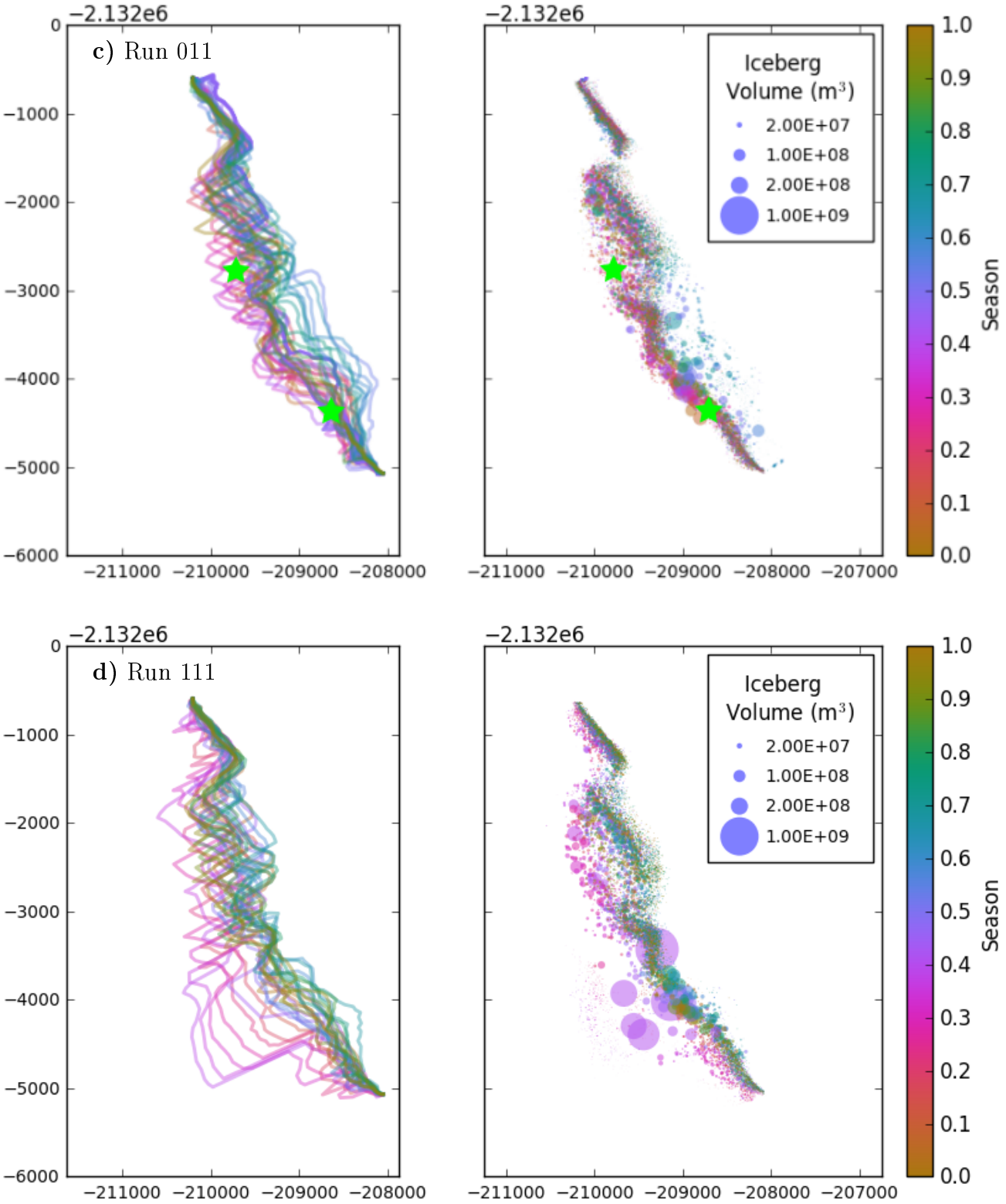

Figure 6.4 (Continued): Continued from previous page.

bergs make a negligible contribution to the terminus mass balance, as illustrated by the cumulative loss histogram. In fact, this lower peak may be considered somewhat of a model artefact; the volume of these bergs indicate that the stress criterion for calving was reached a few centimetres (or less) behind the terminus. This is orders of magnitude smaller than observed crevasse spacing. As such, I set a volume threshold of $1\,\mathrm{m}^3$ for the volume statistics in Tables 6.1 and 6.2.

The probability density functions for all 4 simulations (Fig. 6.6) show the same peak at $1.0 \times 10^6\,\mathrm{m}^3$, though the peak is highest for the submarine melt simulations (Runs 010,011), indicating a tendency for more smaller icebergs and fewer large bergs. The 'no forcing' simulation (000) shows a tendency for larger bergs, while the full forcing scenario has the largest bergs, on the whole. This fits with the observed seasonal ranges of the various simulations (Figs. 6.3, 6.4); both Run 000 and Run 111 extend a long floating tongue in the south, capable of calving large icebergs, while Runs 010 and 011 maintain a fairly constant terminus geometry, calving predominantly smaller icebergs triggered by submarine melt undercutting.

The statistics in Table 6.1 show that Run 111 produced the largest icebergs ($1.29 \times 10^9\,\mathrm{m}^3$), and also showed the greatest variability in iceberg size. However, mean iceberg volume was greatest in Run 000 ($2.29 \times 10^6\,\mathrm{m}^3$) when no environmental forcing was applied. Run 010 showed the smallest mean berg volume ($1.64 \times 10^6\,\mathrm{m}^3$), as well as the smallest maximum berg size and the least variability.

Run Code	Max Berg Vol. (m^3)	Mean Berg Vol. (m^3)	StdDev Berg Vol. (m^3)
000	4.90e+8	2.29e+6	8.28e+6
010	2.40e+8	1.64e+6	5.48e+6
011	2.95e+8	1.65e+6	5.96e+6
111	1.28e+9	1.90e+6	1.50e+7

Table 6.1: Iceberg Volume Statistics for 4 Forcing Combinations (Bergs $< 1\,\mathrm{m}^3$ removed)

To quantify the observed pattern of larger bergs to the south, I split the terminus in half north/south, and present calving event statistics for each side in Table 6.2. In every simulation, the largest calving events occur on the south, as expected; in every case, the largest bergs on the south are at least twice as large as the those on the north. In simulation 111, the largest calving event in

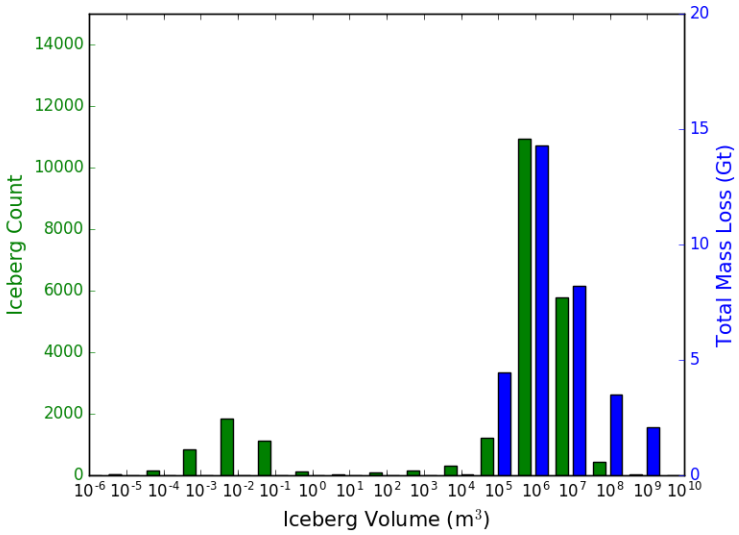

Figure 6.5: Histogram of iceberg volume (green) and total mass loss from calving events of corresponding size (blue) for Experiment 1 simulation 111. The distribution of calving event sizes is bimodal, but icebergs smaller than $1\,\mathrm{m}^3$ make a negligible contribution to mass loss.

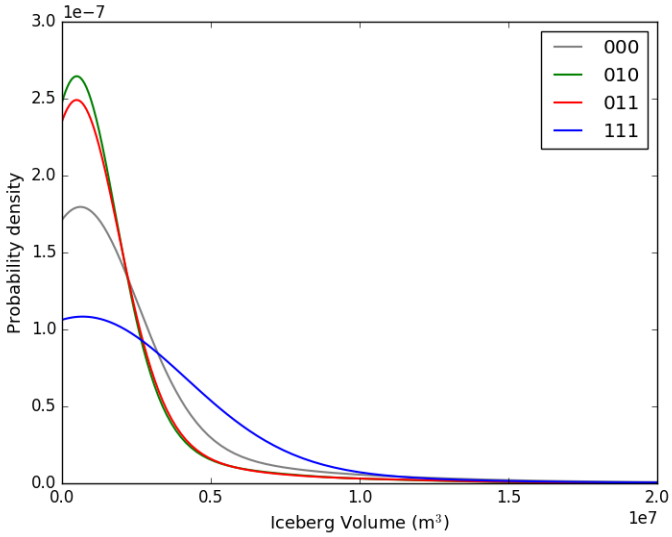

Figure 6.6: Probability density function of iceberg volume for the 4 forcing scenarios. Note linear x-axis, in contrast to Fig. 6.5 above. As in Fig. 6.5,all simulations show the peak at $1.0 \times 10^6\,\mathrm{m}^3$. The submarine melt simulations (010, 011) show a tendency for smaller bergs, while the full forcing simulation (111) tends towards the largest bergs. PDF estimated using Kernel Density Estimate.

the south (post-mélange tabular berg) is almost an order of magnitude larger than the largest in the north. The mean iceberg size is also consistently larger in the south than the north, as is the standard deviation, indicating a larger range of iceberg volumes calved from the southern portion of the terminus. The observation that maximum and mean iceberg volumes are greater in the south for all simulations indicates that the flotation of the southern side promotes larger icebergs, even without the extension of the long floating tongue seen in Runs 111 and 000.

	Max Berg Vol. (m^3)		Mean Berg Vol. (m^3)		StdDev Berg Vol.(m^3)	
Run Code	South	North	South	North	South	North
000	4.90e+8	1.67e+8	2.85e+6	1.97e+6	1.26e+7	4.21e+6
010	2.40e+8	1.03e+8	1.87e+6	1.48e+6	7.64e+6	3.02e+6
011	2.95e+8	1.15e+8	1.86e+6	1.48e+6	8.35e+6	3.16e+6
111	1.28e+9	1.67e+8	2.21e+6	1.65e+6	2.19e+7	4.25e+6

Table 6.2: Iceberg Volume Statistics for 4 Forcing Combinations partitioned North/South (Bergs $< 1\,\mathrm{m}^3$ removed)

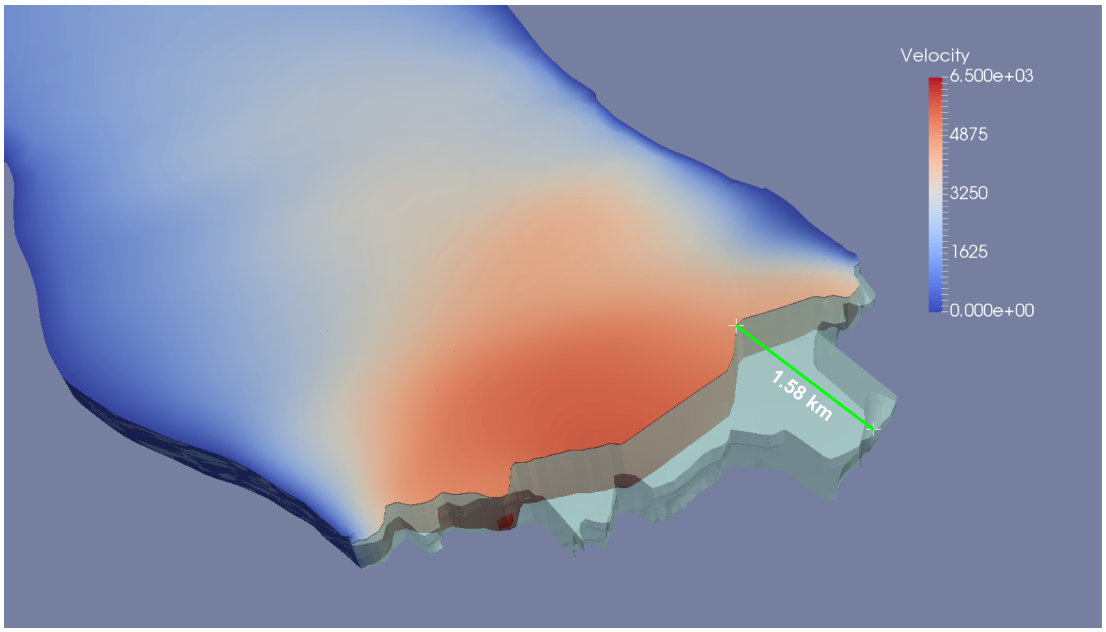

Figure 6.7: Rendering of model terminus showing large tabular calving event at 1.41 years of simulation 111. Transparent region defines the geometry of the tabular berg (and additional concurrent bergs) released following the ice mélange collapse. The large tabular berg is 1.6 km long in the flow direction, with a mass of 1.14 Gt and a volume of $1.28 \times 10^9\,\mathrm{m}^3$.

6.1.5 Mass Components

The seasonal advance and retreat of Store's terminus, discussed in Section 6.1.3, can be understood to reflect changes in the balance between mass influx and mass loss. The terminus mass balance consists of a single mass source (influx) and three sources of mass loss: calving, submarine melting and surface melting. In this section, I investigate the balance between these processes in the region beyond the flux gate shown in Figure 6.2, instead of the entire model domain; this allows us to focus on frontal processes, as the mass balance of the full glacier domain contains a significant contribution from surface mass balance.

Figure 6.8 demonstrates how the components of the near-terminus mass balance change through time for each of the Experiment 1 simulations. The green line in Figure 6.8 plots the total flux through the flux gate shown in Figure 6.2, while the cumulative shading shows the mass loss components. The balance between these mass sources and sinks is the total mass beyond the flux gate, which is shown by the black line. For the sake of visual clarity, calving mass loss is smoothed by a moving average with a window size of 5 timesteps (0.05 years), as

calving losses from tabular bergs up to 1.58 km in length and mass up to 1.14 Gt can dwarf all other ablation processes in a given timestep. Surface melting is included in these plots, though it appears to be absent due to its negligible contribution to mass balance *in the region downstream of the flux gate.* Table 6.3 shows the cumulative values for the mass components in Figure 6.8, over the full 5 years of each simulation. These cumulative data reveal that mass loss is dominated by calving in all simulations, though submarine melt processes remove a significant quantity of ice when present.

In the 'no forcing' run (Fig. 6.8a), the only sources of mass loss are calving and negligible surface melting. Calving losses are characterised by a fairly constant background rate, punctuated with periodic large losses which display a periodicity of around 42 days. The largest calving event was $4.9 \times 10^8\,\mathrm{m}^3$ (Table 6.1). The influx through the flux gate remains fairly constant in comparison to the large variability in calving losses. There is a slight increase in the early summer, followed by a late summer dip, mirroring the observed changes in front velocity (Fig. 6.3).

The addition of distributed submarine melting (Fig. 6.8b) leads to a markedly different pattern of calving. While some periodicity remains, overall the calving rate is more constant than in the 'no forcing' run. The magnitude of the largest calving events are significantly smaller ($2.4 \times 10^8\,\mathrm{m}^3$, Table 6.1). The summer increase in submarine melt rate results in a slight negative overall mass balance, as made evident by the slight decrease in terminus mass (Fig. 6.8b, black line), and the corresponding retreat shown in Figure 6.3a. However, the change in total mass loss in summer is less than the additional melt, indicating that there is a *reduction* in calving rate when melt rate is increased. This suggests that the primary effect of distributed melting in the model is to consume ice mass which would otherwise have calved, rather than promoting calving by undercutting.

Adding concentrated melting (Fig. 6.8c) on top of the distributed melt each summer also has an effect on the pattern of calving, despite its small contribution to the total mass loss. The conical plumes significantly *promote* calving (pink spikes), whereas the distributed melting inhibits it. This results in greater seasonal range in terminus mass (Fig. 6.8c) and position (Fig. 6.3a). However, mean annual calving rate is actually slightly reduced from 7.17 Gt with only distributed melting to 6.99 Gt with additional concentrated melting, illustrating the fact that the concentrated melt does not induce any long term change in terminus position,

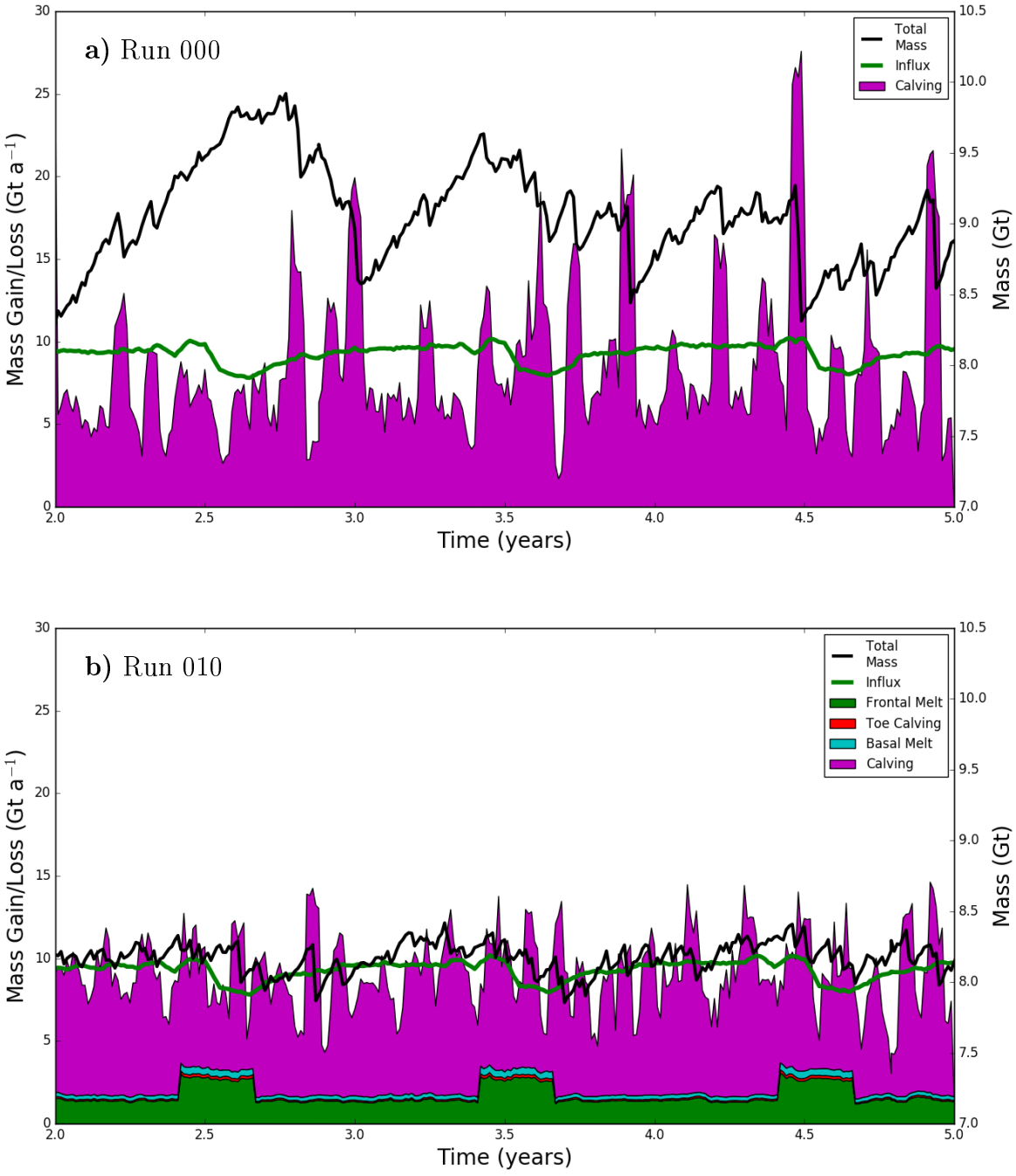

Figure 6.8: Components of mass loss near the terminus (shaded region), influx through the flux gate shown in Fig. 6.2 (green line), and glacier mass beyond the gate (black line), for the 4 forcing combinations: a) Run 000 b) Run 010 c) Run 011 d) Run 111. 'Total Mass' refers to the mass of the glacier beyond the flux gate, so only the change in this value is relevant. The negligible contribution of surface melting beyond the flux gate is omitted.

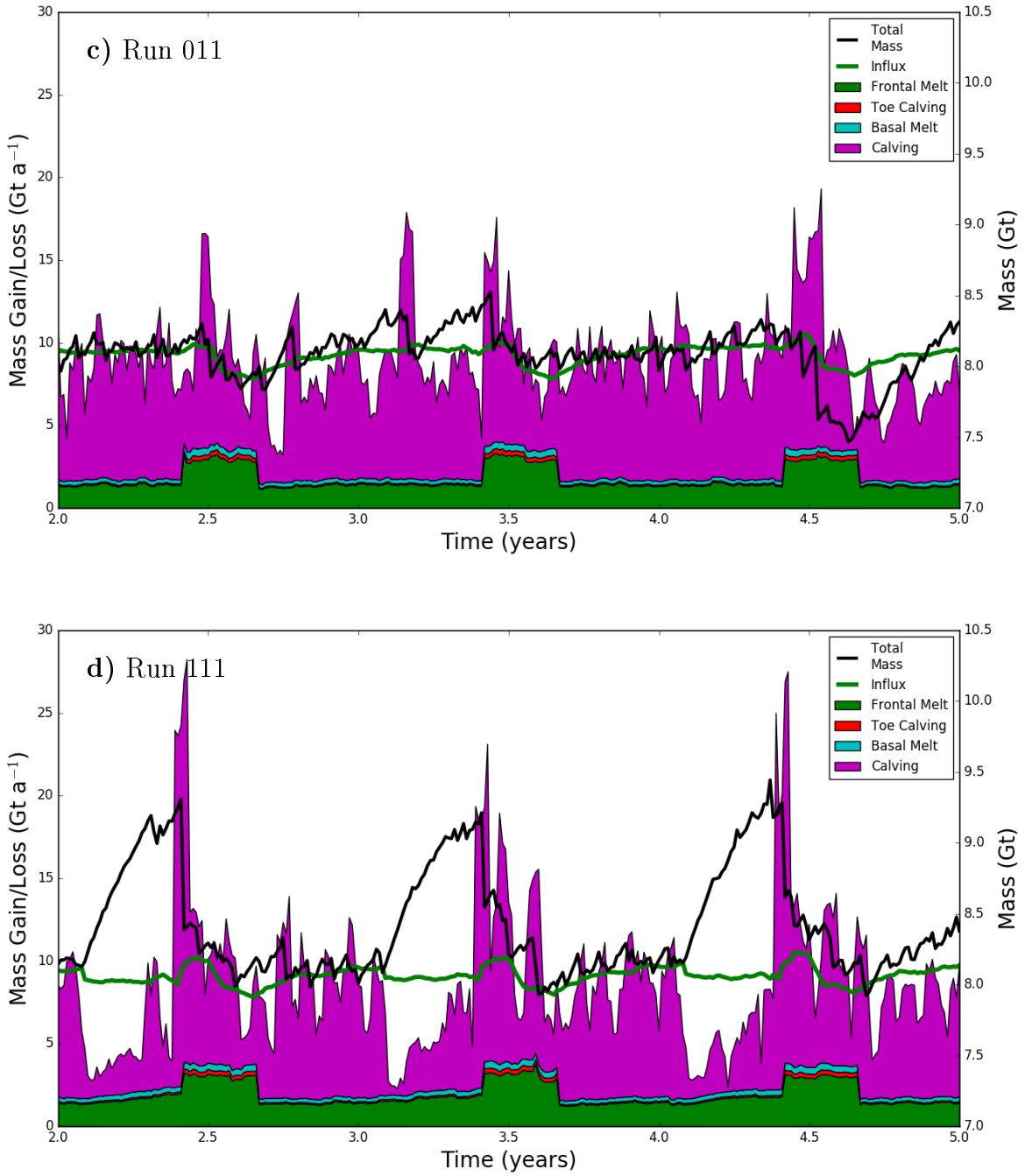

Figure 6.8 (Continued): Continued from previous page.

at least over the 5 years of the simulation. In the fifth summer of the simulation (Time 4.5), the terminus retreats significantly, rapidly losing 0.9 Gt of mass, and retreating beyond the range otherwise observed in any of the simulations. However, it rapidly readvances from the end of summer through to the end of year 5, regaining all the previously lost mass.

Adding ice mélange buttressing (Fig. 6.8d) completes the suite of environmental forcing parameters in Experiment 1. The mélange exerts a significant influence on the components of the total mass balance. As already illustrated in Figure 6.3b, the buttressing effect of the 140 m thick mélange decreases the velocity at the terminus by up to $600\,\mathrm{m\,a^{-1}}$, and Figure 6.8d confirms that this buttressing effect reduces the flux towards the front, which decreases from $10\,\mathrm{Gt\,a^{-1}}$ to $8\,\mathrm{Gt\,a^{-1}}$ over the mélange season. The deceleration from this buttressing effect manifests as a reduction in mean annual influx towards the terminus (8.96 Gt, Table 6.3). It is also clear that the mélange significantly affects calving rate, leading to an almost complete cessation of calving when present, and promoting the release of large tabular bergs when it collapses each spring. The largest of these tabular bergs was $1.28 \times 10^9\,\mathrm{m^3}$ (Table 6.1), almost an order of magnitude larger than the biggest icebergs released by the melt-only simulations (Runs 010, 011). Figure 6.7 shows one of these annual tabular calving events, released in year 2 of the all-forcing simulation (Run 111).

Looking in more detail at the effect of ice mélange on calving, modelled calving rates are lowest immediately following the formation of the mélange in February each year. As the floating tongue advances into the fjord, calving rate increases, suggesting that the terminus is evolving towards a state of instability, increasing stresses near the terminus and promoting calving. The collapse of the ice mélange causes the terminus to become immediately unstable, but the increase in calving rate prior to this collapse may indicate that, even if ice mélange were present year round, the floating tongue may eventually reach a limit beyond which it cannot advance further.

The mélange driven growth and collapse of the floating tongue dominates the change in mass shown in Figure 6.8d. During the mélange season, there is also a slight upward trend in mass lost from submarine melt. This is due to the fact that the growth of the floating tongue increases the surface area of the terminus, as well as increasing the floating area of the base, which is exposed to basal melting. Table 6.1 confirms this effect: mean annual mass loss from

distributed ($1.77\,\mathrm{Gt\,a^{-1}}$), concentrated ($0.11\,\mathrm{Gt\,a^{-1}}$) and basal ($0.3\,\mathrm{Gt\,a^{-1}}$) melt rates are highest in the all-forcing simulation (Run 111), despite the fact that the same melt rates are applied as in Run 010 and 011.

Figure 6.8 includes a mass loss component 'toe calving' which is explained in Section 5.9.2. Briefly, forced convective plume simulations carried out to constrain frontal melting indicate a maximum submarine melt rate slightly above the base of the ice (Fig. 5.12b). The cumulative effect of this melt pattern is to leave a very long, thin 'toe' at the base. The removal of these toes by buoyant calving is not predicted by the calving model, as explained in Section 5.9.2. Instead, toe removal is forced by artificially setting the melt to a maximum at the base; this additional artificial melt is labelled 'toe calving'. In all the results presented in this chapter (Tables 6.3 - 6.6), the contribution of this 'toe calving' to overall terminus mass loss is extremely small.

Run Code	Influx	Submarine Melt			Surface Melt	Toe Calving	Calving
		Distributed	Concentrated	Basal			
000	9.14	0	0	0	$2.51e{-2}$	0	8.6
010	9.18	1.74	0	0.29	$2.34e{-2}$	0.11	7.17
011	9.15	1.7	0.1	0.29	$2.32e{-2}$	0.13	6.99
111	8.96	1.77	0.11	0.3	$2.39e{-2}$	0.14	6.5

Table 6.3: Annual mean mass gain and loss ($\mathrm{Gt\,a^{-1}}$) for 4 forcing scenarios, for the region beyond the flux gate shown in Figure 6.2.

6.2 Results: Experiment 2 - Model Sensitivity

This section presents results from Experiment 2, the sensitivity analysis. I investigate the effect of perturbing the model forcings in a manner consistent with a warming climate, focusing on the processes of submarine melting, both distributed and concentrated, and ice mélange. First, I investigate the effect of changing the magnitude of each forcing, the results of which are presented in Section 6.2.1. Subsequently, I modify the *duration* over which each forcing is applied (Section 6.2.2). I also briefly investigate the effect of changing basal slip (Section 6.2.3). These sensitivity experiments and the relevant forcing parameters are outlined in Table 5.1 (p. 103).

Experiment 2 simulations are assigned a code for brevity and clarity (e.g. 'Run MA2'). The first letter distinguishes between (M)agnitude, (D)uration or (B)asal drag simulations. For magnitude simulations, the second letter distinguishes between (M)élange, (D)istributed melt, (C)oncentrated melt or (A)ll forcings. Duration simulations are either duration only (D) or duration and magnitude combined (DM). In both cases, the final digit refers to either the 1st or 2nd perturbation, where the 2nd is more 'severe'. Basal slip simulations are coded Run B09, where 09 indicates that the value of the basal slip coefficient has been scaled by 0.9.

All of the sensitivity experiments outlined above were run for 5 years, or until the simulation broke down irrecoverably. These 5 year simulations begin from the end of the Experiment 1 'full forcing' simulation (Run 111). As a control, I also run the full forcing simulation for a *further* 5 years for comparison. In the figures and text that follows, this run is referred to as 'control'.

6.2.1 Magnitude Sensitivity

The magnitude sensitivity experiments comprise step changes in the magnitude of distributed melting, concentrated melting, ice mélange and the combined effect of all 3. Melt rates are scaled by a factor of 1.5 (Runs MD1, MC1) and 2.0 (Runs MD2, MC2), while ice mélange thickness is scaled by 0.5 (Run MM1) and 0 (Run MM2) (i.e. mélange absent). Finally, I combine all three of these forcings in Runs MA1 and MA2. Figure 6.9 shows how the range in terminus position (maximum, minimum and mean extent) is affected by these changes, compared with the

control simulation. These maximum, minimum and mean points are calculated by interpolating at 500 equally spaced points across the width of the terminus. Figure 6.10 shows the patterns of seasonal terminus position and velocity for the eight different magnitude forcing simulations.

Increasing distributed melting by 50% (Run MD1) has only a small effect on the seasonal terminus position over the 5 years of the simulation (Fig. 6.10a) and the overall range in terminus position (Fig. 6.9a). Through the melt season, the mean terminus position is around 150 m behind that of the control simulation, and this pattern repeats consistently each melt season for the 5 years of the simulation. The terminus extrema plot shows that this additional retreat is largely limited to the region of the terminus slightly south of centre. The mean terminus position in this region is also slightly upstream of the control simulation.

Doubling the distributed melt rate (Run MD2) has a significant destabilising effect on the calving terminus. For the first year of the simulation, the mean terminus position is very similar to Run MD1 (Fig. 6.10a). However, at the start of the summer melt season in the second year, the terminus rapidly retreats by an average of 900 m, far beyond the usual seasonal range. Fig. 6.9a shows that this retreat is entirely limited to the southern side of the terminus, which retreats by up to 1.5 km. Towards the end of the melt season of the second year, the simulation breaks down irrecoverably, due to problems with the free surface evolution.

Mean annual mass loss components and influx for the distributed melt perturbation experiments are shown in Table 6.4. These results reveal that for both the x1.5 and x2 perturbations (Runs MD1, MD2), calving rate is less than the control. This agrees with the results of Experiment 1, in which the addition of distributed melting reduced the calving rate. For Run MD1, average annual mass loss from calving is reduced from 7.19 Gt to 6.66 Gt. Doubling the distributed melt rate (Run MD2) causes calving rate to increase slightly compared with MD1 to 7.07 Gt, due to the greater overall mass loss which accompanies the significant retreat of the terminus.

Increasing the melt rate from concentrated plumes by a factor of 1.5 (Run MC1) has no systematic effect on the shape or velocity of the terminus over the 5 year simulation. There is some difference in the minimum extent of the terminus, but the pattern varies between years: in years 1, 3 and 5, the increase in concentrated melting causes more retreat in summer, but in year 4 there is no

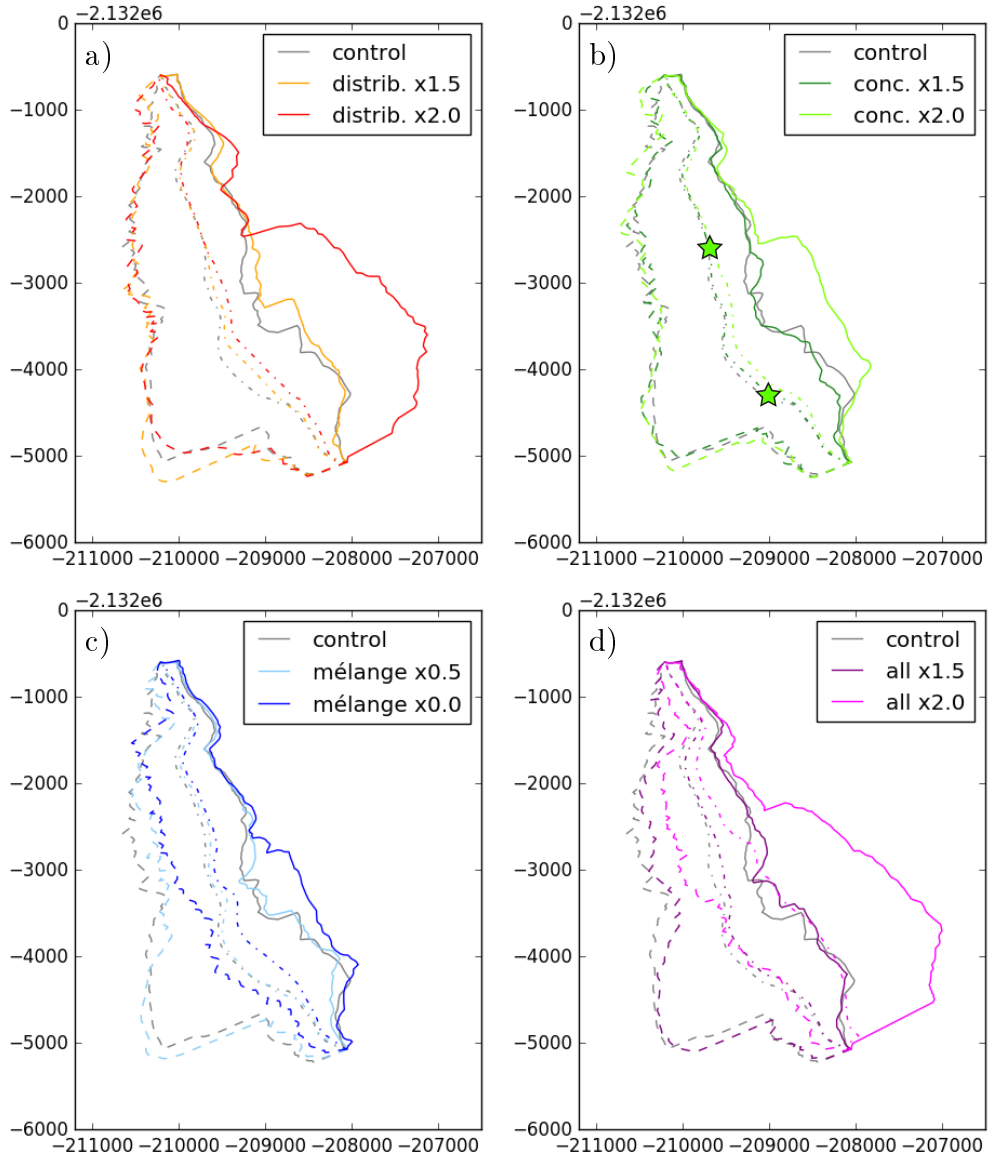

Figure 6.9: Maximum (dashed), mean (dash-dotted) and minimum (solid) terminus positions for step changes in a) distributed melt rate (Runs MD1, MD2), b) concentrated melt rate (Runs MC1, MC2), c) mélange thickness (Runs MM1, MM2), and d) all of the above (Runs MA1, MA2). Green stars in (b) show the position of the two concentrated plumes. Grey lines indicate the control simulation, and increasingly bright colour indicates more severe environmental forcing.

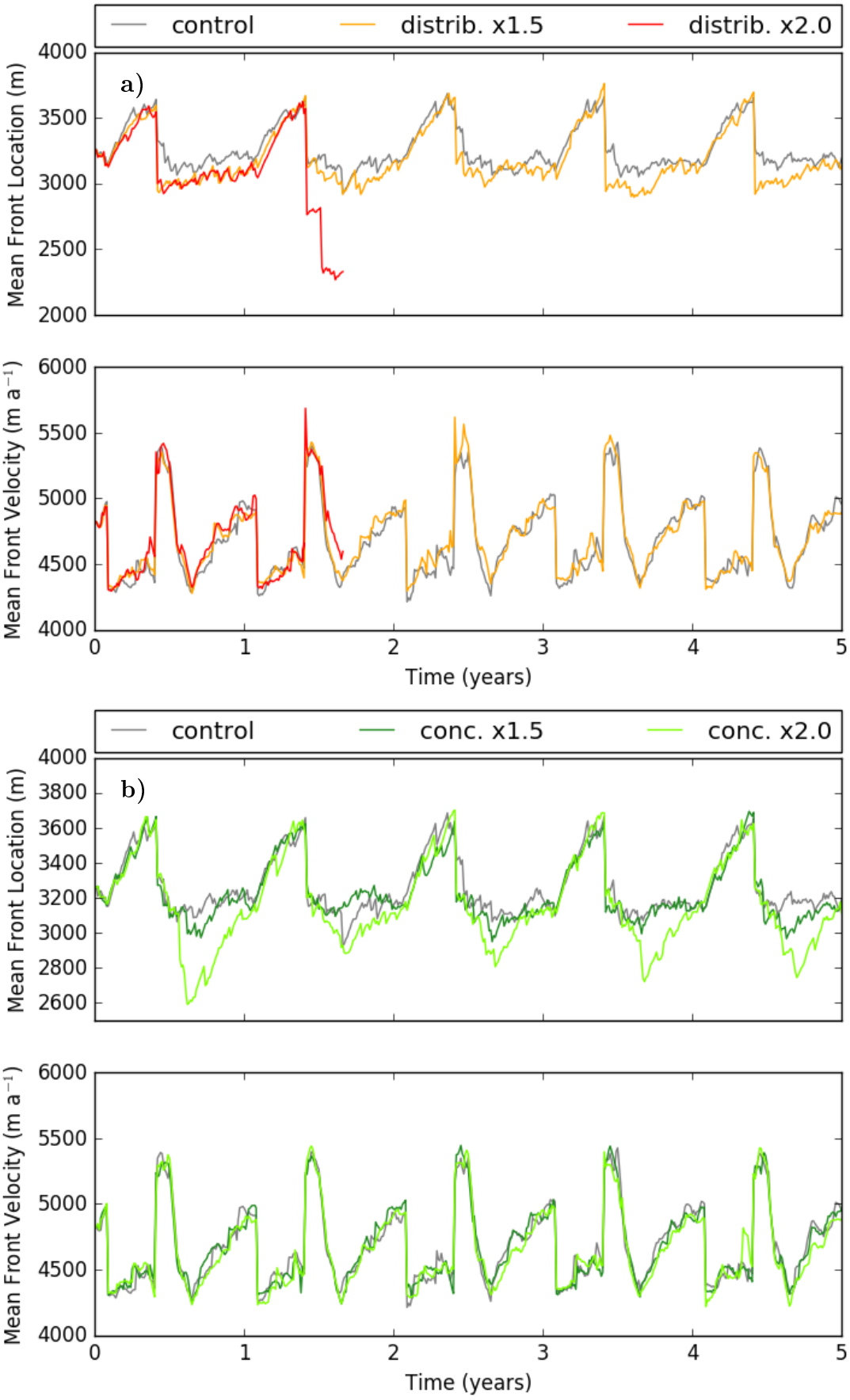

Figure 6.10: Mean terminus position (top panel) and velocity (bottom panel) over 5 years for step changes in a) distributed melt rate (Runs MD1, MD2), b) concentrated melt rate (Runs MC1, MC2), c) mélange thickness (Runs MM1, MM2), and d) all of the above (Runs MA1, MA2).

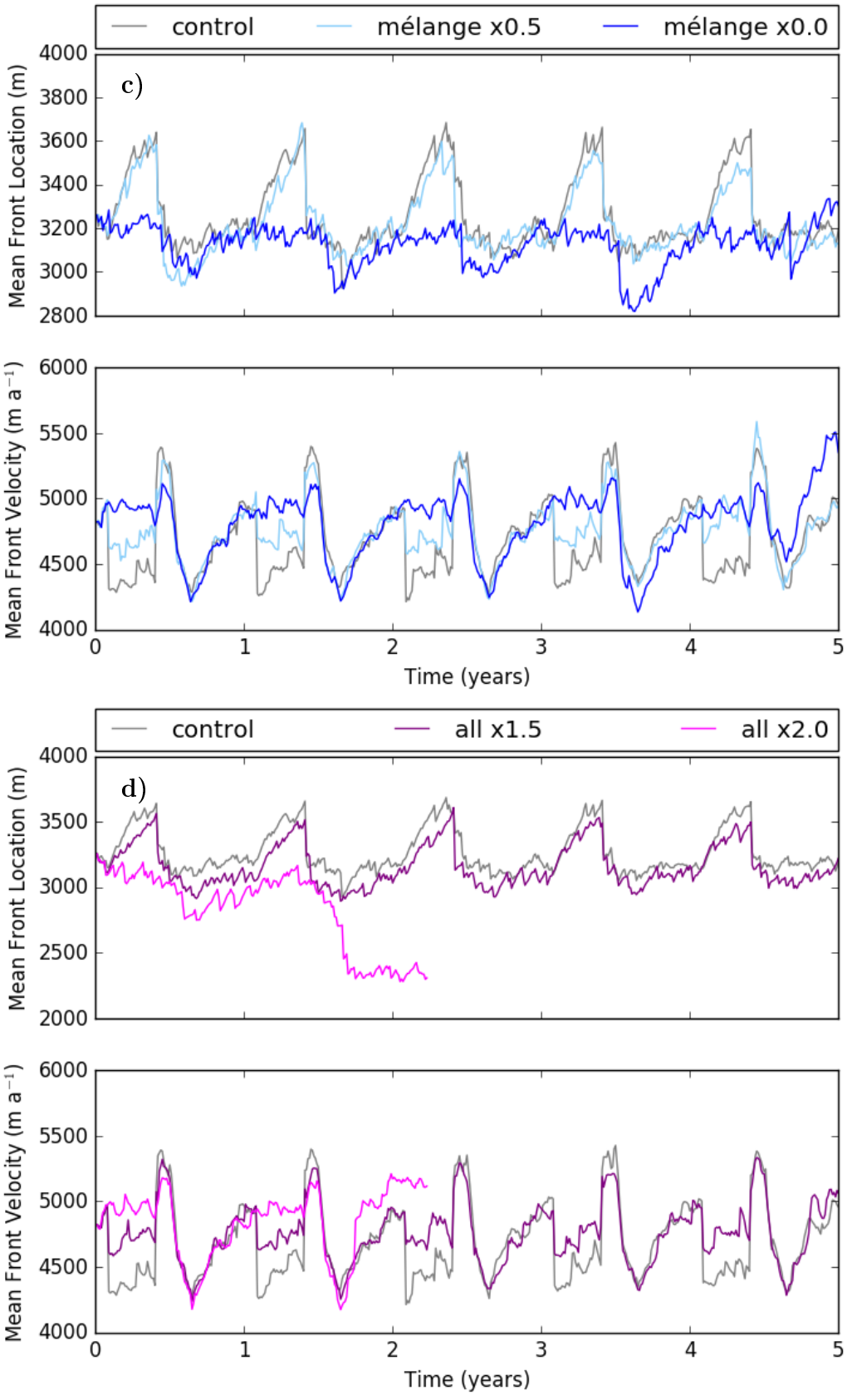

Figure 6.10 (Continued): Continued from previous page.

Run Code	Influx	Submarine Melt			Surface Melt	Toe Calving	Calving
		Distributed	Plume	Basal			
control	9.4	1.81	0.11	0.3	$2.4e{-2}$	0.14	7.19
distrib. x1.5	9.43	2.5	$9.28e{-2}$	0.38	$2.38e{-2}$	0.18	6.66
distrib. x2.0	9.57	3.38	$8.98e{-2}$	0.44	$2.39e{-2}$	0.27	7.07
conc. x1.5	9.41	1.79	0.17	0.29	$2.39e{-2}$	0.17	7.08
conc. x2.0	9.4	1.84	0.23	0.28	$2.36e{-2}$	0.2	6.87
melange x0.5	9.51	1.81	0.11	0.29	$2.38e{-2}$	0.14	7.56
melange x0.0	9.62	1.73	0.1	0.27	$2.33e{-2}$	0.14	7.77
all x1.5	9.55	2.43	0.15	0.39	$2.37e{-2}$	0.2	6.59
all x2.0	9.84	3.07	0.19	0.37	$2.19e{-2}$	0.28	7.07

Table 6.4: Annual mean mass gain and loss (Gt) for Exp2 Magnitude Simulations, for the region beyond the flux gate shown in Figure 6.2.

discernible effect, and in year 2 the terminus retreats *less* than the control.

Doubling the concentrated melt rate (Run MC2) has a significant effect on the retreat of the terminus in summer (Fig. 6.10b). In every year, the terminus retreats further than the control simulation; in year 1 the minimum mean terminus position is almost 600 m less than the control. Figure 6.9b shows that, as with distributed melting, this extra retreat occurs exclusively in the floating region to the southern half of the terminus. In fact, the region of the terminus which retreats further than the control is constrained on either side by the two concentrated plumes.

Halving the ice mélange thickness (Run MM1) has a significant effect on the velocity of the terminus during the mélange season (Fig. 6.10c), due to the reduced buttressing force which directly opposes the driving stress near the terminus. In the control simulation, the formation of the mélange results in an instantaneous deceleration of $650\,\mathrm{m\,a^{-1}}$. When ice mélange thickness is halved, the terminus decelerates by roughly half this amount, confirming the direct role played by mélange buttressing on force balance at the terminus.

When the ice mélange is absent year round (Run MM2), the deceleration does not occur, as is to be expected. Furthermore, the summer peak in velocity, which is coincident with the collapse of the mélange, is reduced from $5400\,\mathrm{m\,a^{-1}}$ to $5100\,\mathrm{m\,a^{-1}}$ when mélange is absent. This indicates that the col-

lapse of the mélange triggers a temporary acceleration beyond the direct response to the change in force balance.

Despite the significant effect on terminus velocity, halving the mélange thickness does not significantly change the seasonal range in terminus position over the 5 years simulated. In year 1 (Fig. 6.10c), the terminus retreats a further 200 m beyond the control, but in other years the seasonal pattern of mean terminus position is largely unaffected. Figure 6.9c shows that the maximum, minimum and mean terminus position is not greatly affected by the halving of mélange thickness.

Removing the mélange entirely does, however, significantly affect the seasonal range in terminus position. The characteristic spring advance of the floating tongue is absent (Fig. 6.10c), and in year 4 the terminus retreats 350 m further than the control simulation, implying that the mélange has an important stabilising effect on timescales longer than a year. Again, this retreat occurs in the floating southern region of the terminus.

The final stage of the magnitude sensitivity experiments is to apply stepped changes to all 3 forcings: distributed melt rate, concentrated melt rate, and ice mélange thickness. Run MA1 scales melt rates by 1.5 and mélange thickness by 0.5, while Run MA2 doubles the melt rates and removes mélange entirely.

In Run MA1, the mean terminus position remains quite consistently around 150 m upstream of the control simulation. The advance due to ice mélange occurs more slowly, and increased melting keeps the terminus in a slightly retreated position compared to the control. As with previous magnitude perturbation experiments, the retreat is mostly confined to the southern side of the terminus (Fig. 6.9d). The velocity time series (Fig. 6.10) displays a pattern similar to the mélange x0.5 experiment (Run MM1); this is unsurprising, as only the mélange perturbation was observed to significantly affect the terminus velocity.

In Run MA2, when melting is doubled and mélange is entirely absent, the behaviour of the terminus is drastically different compared to the control. The mean terminus position never advances beyond the seasonal minimum for the control simulation. During the melt season of year 1, the terminus retreats 450 m before re-advancing, and in year 2, the terminus retreats irrecoverably by almost 1 km, on average (Fig. 6.10d). The terminus remains in this retreated position for 0.66 a, after which the simulation breaks down due to rapid changes in the upper free surface. Figure 6.9d shows that this retreat is confined to the southern,

floating portion of the terminus, the same region as was observed to retreat in all the other magnitude forcing simulations. In this case, the entire southern side of the terminus has retreated more than 1 km beyond the minimum position observed in the control simulation. The velocity of the terminus in Run MA2 is fairly consistent with the control, with two exceptions. Firstly, the lack of mélange means there is no terminus slow down in spring, as is to be expected. Secondly, for half a year following the start of the dramatic retreat, the terminus velocity was at least $300\,\mathrm{m\,a^{-1}}$ faster than the control, after which the simulation breaks down.

6.2.2 Duration Sensitivity

Having investigated the effect of increasing melt magnitude and decreasing mélange thickness, I next investigate the effect of changing the duration of each forcing. During the summer melt season, which runs from 1st June to 31st August (3 months) in Experiment 1, distributed melting occurs at the prescribed summer rate, and concentrated melting is imposed on top of this. In the remaining 9 months of the year (1st September to 31st May), distributed melting occurs at the prescribed winter rate and the concentrated plumes are absent. Ice mélange in Experiment 1 was present from 1st February to 29th May (4 months).

Presently, to investigate the sensitivity of the model to these season lengths, I modify both in tandem by extending the summer melt season and shortening the winter ice mélange season, first by 1 month (Run D1) and then by 2 months (Run D2). Finally, I change *both* the season length and the magnitude of all forcings together, by combining the 1 month duration forcing with the x1.5 melt and x0.5 mélange magnitude forcings (Run DM1), and then the 2 month duration forcing with the x2 melt and x0.0 mélange magnitude forcings (Run DM2).

Modifying the season lengths by 1 month (Run D1) has very little effect on the calving behaviour and terminus stability during the five years of the simulation (Figs. 6.11a and 6.12a). Despite the shorter mélange season length, the advance of the terminus in spring is similar to the control, though it retreats sooner due to the earlier collapse of the mélange. The characteristic deceleration which accompanies the formation of the mélange was delayed, as is to be expected. Aside from these effects from the reduced mélange season, there are no significant differences between Run D1 and the control, until the end of year 5, when the

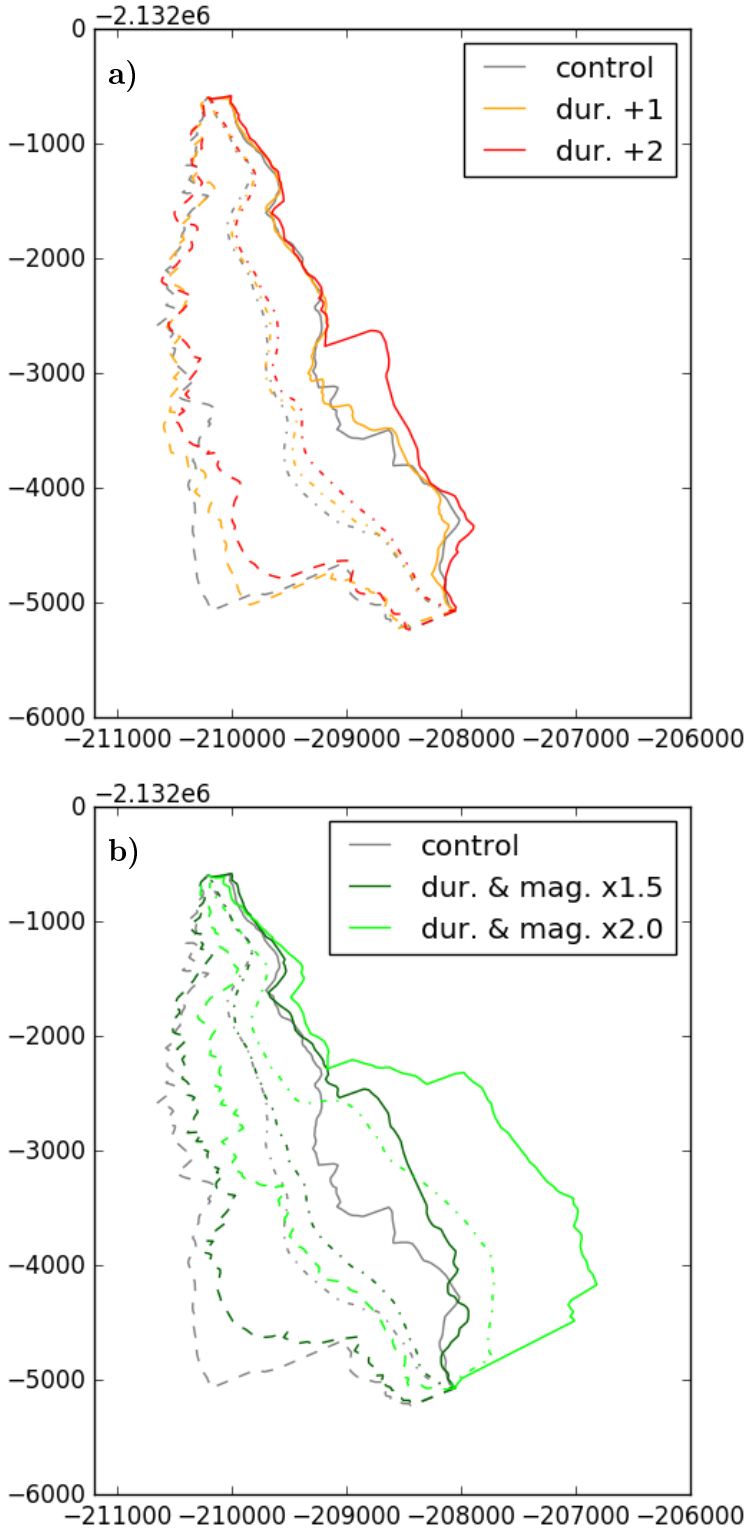

Figure 6.11: Maximum (dashed), mean (dash-dotted) and minimum (solid) terminus positions for step changes in a) melt and mélange season length only (Runs D1, D2), and b) both season length and forcing magnitude (Runs DM1, DM2). Grey lines indicate the control simulation, and increasingly bright colour indicates more severe environmental forcing.

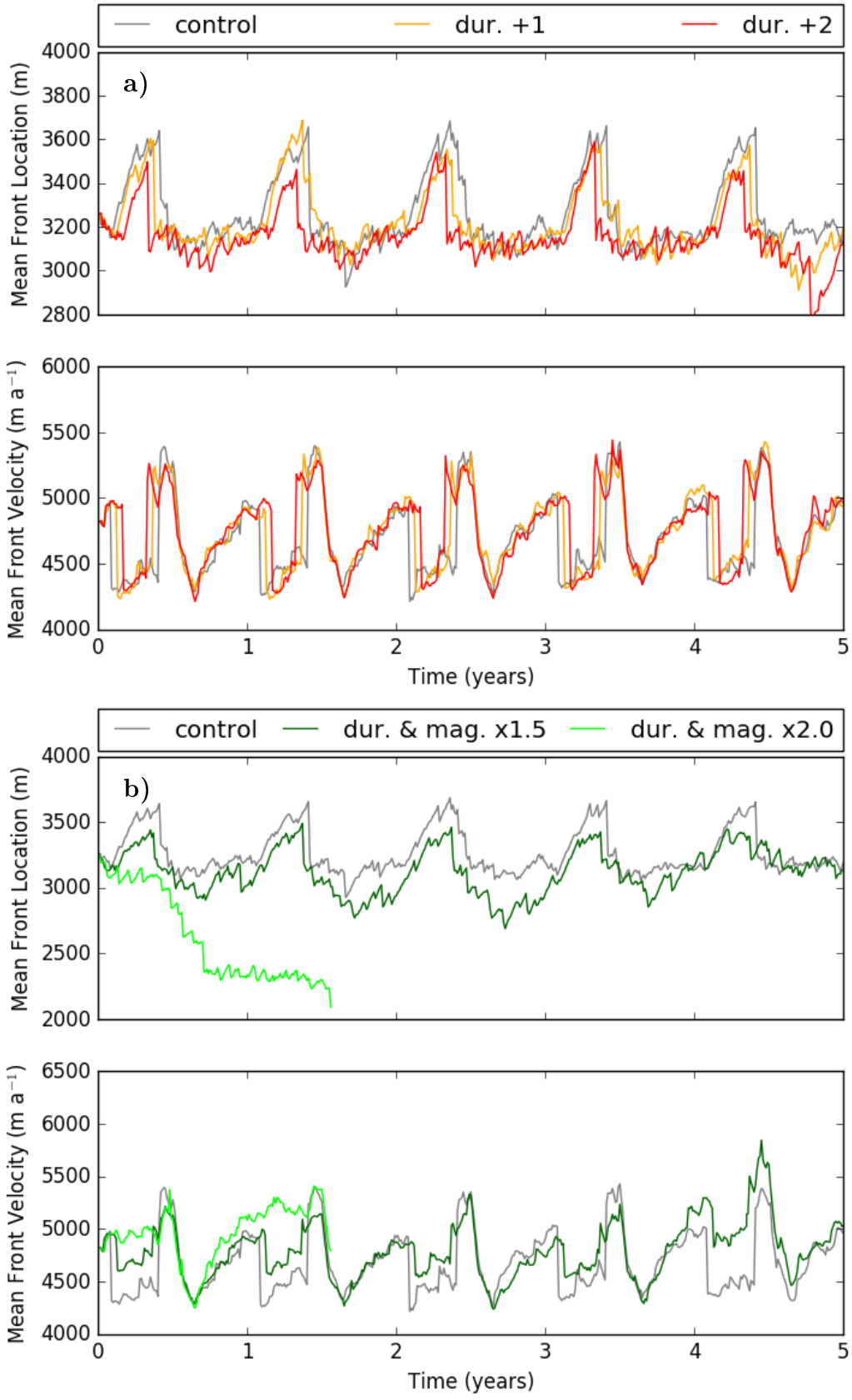

Figure 6.12: Mean terminus position (top panel) and velocity (bottom panel) over 5 years for step changes in a) forcing duration (Runs D1, D2), and b) both forcing duration and magnitude (Runs DM1, DM2). Note different y-scales between simulations.

terminus undergoes a greater (400 m) melt-driven retreat in summer. Note that this retreat is similar to that observed in the control simulation in the summer of year 2, and so it is not certain that this retreat in year 5 is the beginning of a destabilisation of the terminus.

When season lengths are modified by 2 months (Run D2), the glacier exhibits similar behaviour to Run D1, with the exception that the spring advance of the terminus consistently fails to reach the advance of the control simulation, typically advancing only 400 m on average. As with Run D1, the velocity changes mainly to reflect the shorter mélange buttressing season, and is otherwise consistent with the control. In year 5, the terminus undergoes significant retreat of up to 750 m (Fig. 6.11a).

Combining both magnitude and duration perturbations significantly changes the terminus behaviour. In Run DM1, mean terminus position remains fairly consistently around 200 m further upstream than the control (Fig. 6.12b). In the summer melt seasons of years 2 and 3, the difference between Run DM1 and the control increases to almost 500 m. As with previous perturbation experiments, this extra retreat is confined to the southern floating portion of the terminus (Fig. 6.11b). The velocity time series remains fairly consistent with the control for the first 4 years, apart from the reduced deceleration due to the thinner mélange and shorter mélange season. However, around the beginning of year 5, the terminus accelerates 250 m a^{-1} on average, and remains slightly faster than the control for the remainder of the simulation.

Run DM2 represents the most 'aggressive' perturbation experiment performed. Melt rates are doubled and the summer melt season is increased by 2 months, while mélange is completely absent throughout. Unsurprisingly, the modelled terminus rapidly retreats in the first melt season, retreating on average 750 m to a position which is then maintained for almost 1 year, before retreating another 100 m, at which point the simulation broke down. Again, this retreat is constrained to the southern portion of the terminus, most of which retreated over 1 km compared with the control (Fig. 6.11b).

6.2.3 Basal Slip Sensitivity

A final pair of sensitivity experiments are carried out to investigate the model's sensitivity to changing basal slip. In these experiments, I simply scale the slip

Run Code	Influx	Submarine Melt			Surface Melt	Toe Calving	Calving
		Distributed	Plume	Basal			
control	9.4	1.81	0.11	0.3	$2.4e{-2}$	0.14	7.19
dur. +1	9.47	1.88	0.14	0.31	$2.38e{-2}$	0.15	7.12
dur. +2	9.53	1.92	0.17	0.31	$2.35e{-2}$	0.17	7.36
dur.+mag. x1.5	9.56	2.56	0.21	0.37	$2.35e{-2}$	0.23	6.76
dur.+mag. x2.0	10.16	3.72	0.31	0.32	$2.07e{-2}$	0.39	7.8

Table 6.5: Total mass gain and loss (Gt) for Exp2 Duration Simulations, for the region beyond the flux gate shown in Figure 6.2.

coefficient by 0.9 (Run B09) and then 0.8 (Run B08), under the entire glacier. Figure 6.14 shows time series of mean terminus position and velocity for these sensitivity experiments, while Figure 6.13 shows the maximum, mean and minimum terminus positions. Table 6.6 shows the mean annual mass balance of the near-terminus region for the basal slip experiments.

Aside from the stepped increase in velocity at the terminus (Fig. 6.14), which is a direct consequence of decreasing basal slip, there are no significant effects at all on the terminus position over the 5 year simulation: mean terminus position through time does not differ from the control, and the maximum and minimum terminus extents are only very slightly advanced compared to the control, for both Run B09 and Run B08.

The good agreement in terminus position between the control and the basal slip experiments suggests that calving rate scales with the delivery of ice to the terminus, which is confirmed by the concurrent increase in influx and calving loss shown in Table 6.6.

Run Code	Influx	Submarine Melt			Surface Melt	Toe Calving	Calving
		Distributed	Plume	Basal			
control	9.4	1.81	0.11	0.3	$2.4e{-2}$	0.14	7.19
beta x0.9	10.11	1.83	0.11	0.3	$2.4e{-2}$	0.14	7.88
beta x0.8	10.97	1.97	0.11	0.29	$2.4e{-2}$	0.15	8.67

Table 6.6: Total mass gain and loss (Gt) for Exp2 Beta Simulations, for the region beyond the flux gate shown in Figure 6.2.

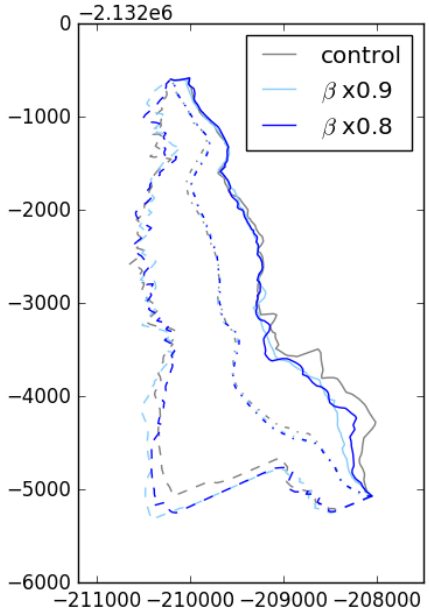

Figure 6.13: Maximum (dashed), mean (dash-dotted) and minimum (solid) terminus positions for step changes in basal slip. Grey lines indicate the control simulation, light blue indicates βx0.9 (Run B09) and dark blue indicates βx0.8 (Run B08).

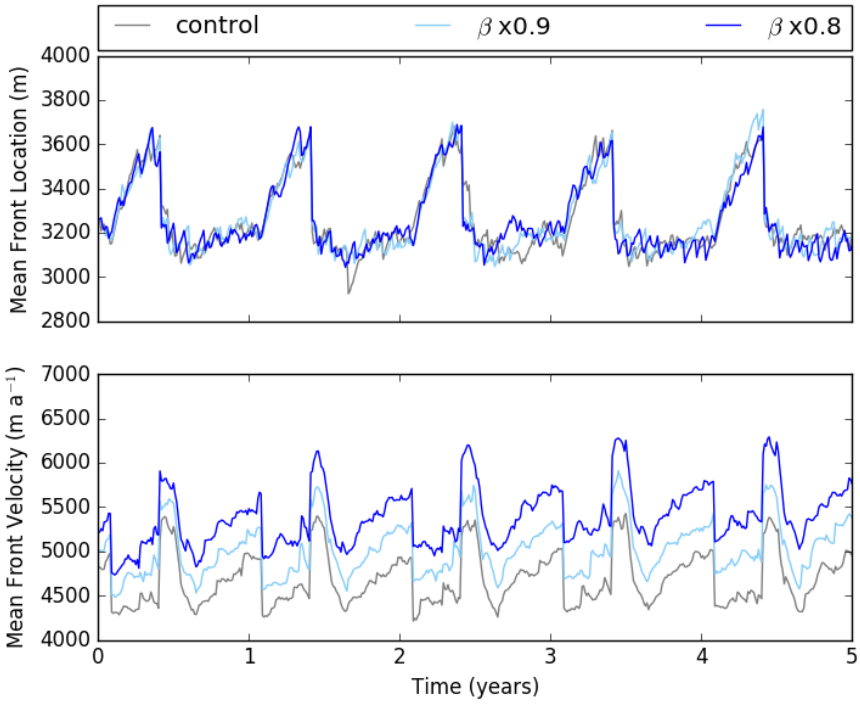

z

Figure 6.14: Mean terminus position (top panel) and velocity (bottom panel) over 5 years for step changes in basal slip (Runs B09, B08).

6.3 Discussion

The 3D calving model applied to Store Glacier demonstrated sensitivity to both ice mélange buttressing and submarine melting (Section 6.1). Ice mélange buttressing resulted in an advance of the terminus, primarily in the southern floating side of the margin. Both distributed and concentrated submarine melting were found to result in retreat of the terminus in summer. The sensitivity of the model to concentrated melting from conical plumes is especially significant, given the small contribution these plumes make to direct mass loss via melting. This section compares the 3D model results with observations (Section 6.3.1), and discusses the observed patterns in crevasse penetration (Section 6.3.2), the importance of topography and glacier geometry (Section 6.3.3), the various environmental forcings (Sections 6.3.4-6.3.5) and the significance of buoyant forces (Section 6.3.6). Finally, some limitations of the 3D model are discussed in Section 6.3.7.

6.3.1 Model vs. Observations

To validate the 3D model, I extract terminus geometries from 24 TerraSAR-X images collected from April 2014 to April 2015 and compare the observed terminus evolution with that of the model. Figure 6.15 shows the maximum, minimum and mean position of the terminus from the model and from TerraSAR-X data from 2014. Figure 6.15a shows terminus position changes from Run 011, where both distributed and concentrated melting are active, but ice mélange is not present, while Figure 6.15b shows Run 111, where ice mélange, as well as distributed and concentrated submarine melting, are active. The best fit between model and observations is found for Run 011, where the maximum and mean terminus positions correspond very closely with the observed changes in margin position. For Run 111, there is a good fit between modelled and observed minimum front position, but the mean and maximum positions obtained with the model are greater than observed, most notably the latter.

Looking in more detail reveals that while the absolute position for the maximum extent matches better for Run 011, there are geometric features in the satellite data which are present in Run 111 (though their extent appears to be exaggerated). In particular, the sharp edge at the southern side of the terminus in Run 111 corresponds to a real feature in the data, where the terminus transitions

from having very little seasonal range to just over 1 km difference between minimum and maximum extents. This feature is greatly exaggerated in the model, but the location of the transition matches well, suggesting that a feature in the basal topography may be responsible.

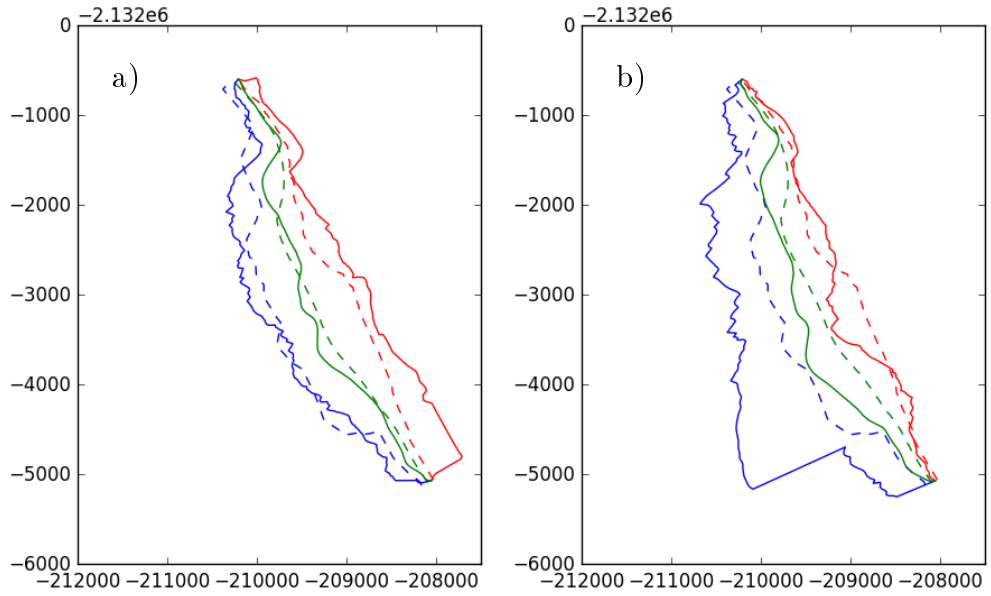

Figure 6.15: Maximum (blue), minimum (red) and mean (green) front positions from 24 TSX satellite images collected between April 2014 and April 2015 (dashed lines) and model output (solid lines) for a) Run 011 and b) Run 111 in Experiment 1. Overall there is reasonable agreement in both simulations, though the fit is significantly better in Run 011, in which ice mélange is absent.

Figure 6.16 shows the mean terminus position over time for Runs 011 and 111 and the observed position from TerraSAR-X in 2014 (as in Fig. 6.15). The observational data from 2014 is repeated for clarity. While the maximum, minimum and mean terminus positions show a better fit with observations in the absence of ice mélange (Fig. 6.15), the evolution of mean terminus position through time tells a more nuanced story. While the *magnitude* of terminus advance in Run 111 is clearly greater than observed in 2014, the pattern and timing of advance and retreat shows good agreement to reality, while Run 011 does not (Fig. 6.16).

In both Run 111 and the satellite data, terminus advance begins in February and continues until May, followed by subsequent rapid retreat to a minimum terminus position in late summer (Fig. 6.16). This is followed by a slow and punctuated advance. In the satellite data, there appears to be significant retreat

before the February to May advance (Fig. 6.16); however, this 'retreat' occurs across the join between the end and the beginning of 2014, and so it is not a real feature; rather, the terminus was more advanced at the end of 2014 than the end of 2013.

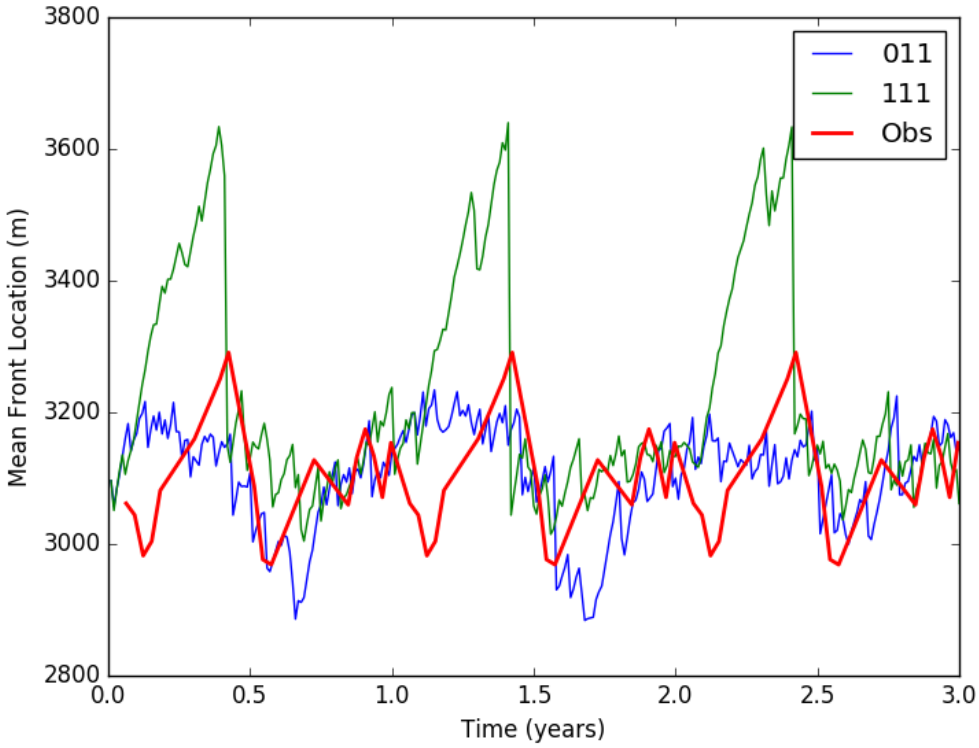

Figure 6.16: Mean front position for Run 011 (blue), Run 111 (green) and from TSX data (red). TSX data were taken from 2014, and are repeated over the time period for clarity. In the satellite data, there appears to be significant retreat before the February to May advance; however, this 'retreat' occurs across the join between the end and the beginning of 2014, and so it is not a real feature; rather, the terminus was more advanced at the end of 2014 than the end of 2013.

In terms of velocity, the model presents a qualitatively good fit to independent observations. Figure 6.17a plots Store's surface velocity from two GPS sensors, one located 8 km upstream of the terminus, and another 20 km upstream of the terminus, from Ahlstrøm et al., (2013). The modelled mean terminus velocity is shown in Figure 6.17b over an equivalent time period (August to August) for Runs 011 and 111. Because the GPS records are from some distance upstream, the velocities are of a very different magnitude to those at the modelled terminus.

However, both the GPS and Run 011 data show the same pattern of rapid acceleration beginning around October which decreases over the winter season before a distinct peak in early summer. This is followed, in both cases, by a dramatic deceleration in late summer. Run 111 shows a similar pattern for most of the year, but during the mélange season (Feb-May) there is a significant deceleration due to the buttressing effect of the ice mélange.

The good agreement between modelled and observed velocity evolution is not surprising, given that I use observed velocity to invert for the basal boundary condition (Section 5.7). As such, this is not a validation of the calving model itself, but does suggest that the seasonal inversion procedure works as expected. The discrepancy during the mélange season between Run 111 and observations has two potential explanations. First, this may suggest that the model exaggerates the effect of ice mélange buttressing on the terminus. Alternatively, it may be the case that this deceleration is a real feature, but the effect diminishes upstream, such that neither the 8 km nor the 20 km GPS capture it.

Overall, there is good agreement between modelled and observed calving behaviour, especially considering that the calving model is uncalibrated and untuned, and not specifically designed to replicate the available observations. This overall good correspondence between model and observations therefore provides strong support for the use of the crevasse depth model in predicting calving, and also for the use of the 3D model over the 2D model (Section 7.2), which did require tuning. Several features from the observational data showing lateral variability in calving behaviour also appeared in the model (Fig. 6.15). This highlights the importance of accurate basal topography, which has been a major limitation to calving models, until the recent development of mass-conservation techniques (Appendix A.2, Morlighem et al., (2011)).

The fact that the observed seasonal range in terminus position can be simulated using submarine melting alone indicates the importance of this process. In the model, submarine melting is partitioned into distributed melting from planar plumes and concentrated melting from conical plumes. The difference in seasonal range in terminus position between Run 010 (distributed melt only) and Run 011 (distributed + concentrated) (Figs. 6.4b,c) indicates that it is primarily the concentrated plume melting which is responsible for this seasonal range, especially in the southern portion of the terminus. In the 2D model, it was not possible to represent this concentrated conical plume melting, and the outputs from the 2D

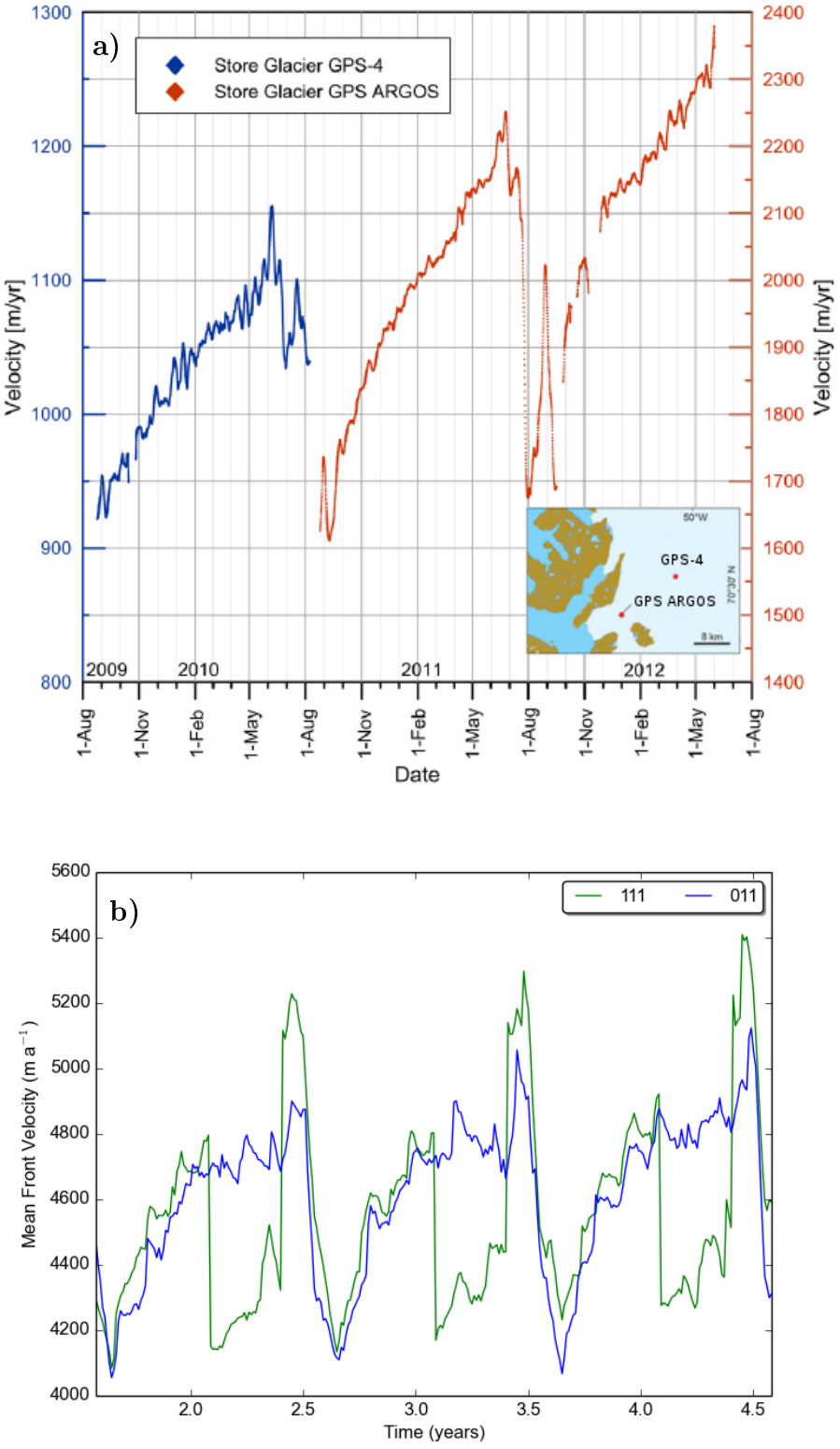

Figure 6.17: a) GPS record of surface velocity 20 km upstream (blue) and 8 km upstream (red) from the terminus of Store Glacier between Aug 2009 and Aug 2012 from Ahlstrøm et al., (2013). Inset: location of GPS sensors. b) Modelled mean terminus velocity for Experiment 1 Runs 011 (blue line) and 111 (green line), from August Year 1 to August Year 4.

model led to contradictory conclusions. This discrepancy between the 2D and 3D models is explored further in Section 7.2.

In general, the observed evolution of front position through time supports the role of ice mélange in suppressing calving, though the mélange buttressing appears to have a greater effect in the model than in reality. The discrepancy in the velocity time series, in conjunction with the overestimated advance of the terminus, strongly suggest that the model is overstating the effect of the mélange. There are a number of potential reasons for this, which are explored in Section 6.3.5, below.

6.3.2 Crevasse Depth

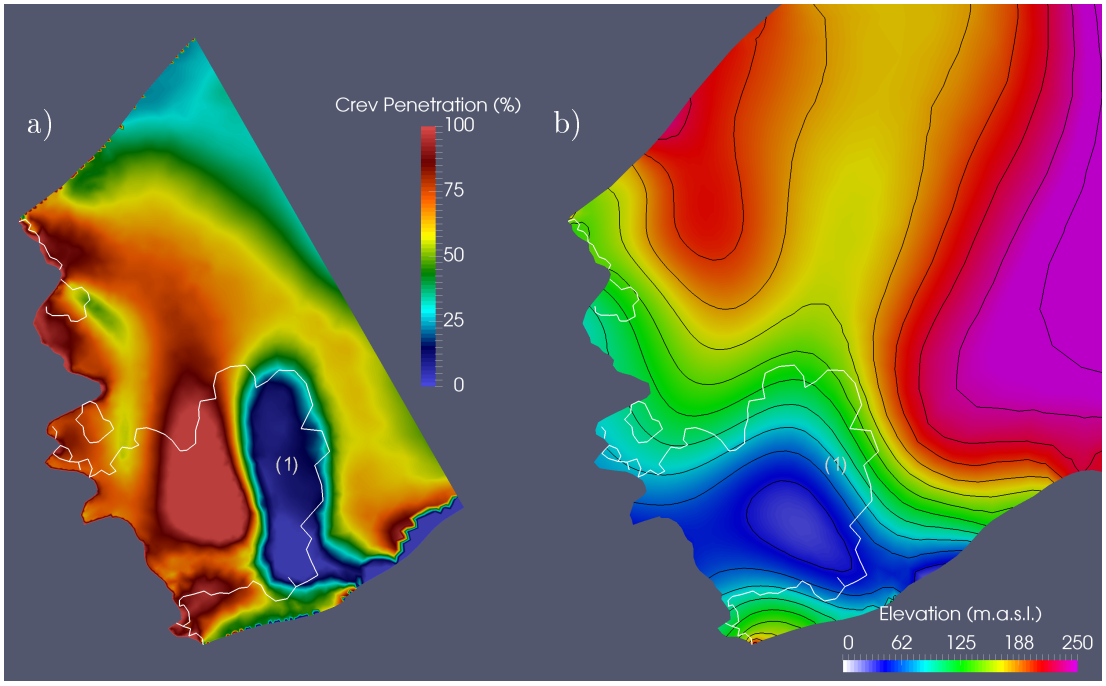

Figure 6.18: a) Crevasse penetration (%) for surface crevasse model, and b) surface elevation. White line represents the grounding line. Surface contours (black) are spaced 20m apart. The large region with suppressed surface crevassing at point (1) is coincident with the grounding line, and is the result of an upward bending moment from the buoyant force, which pivots here at the grounding line.

The surface and basal crevasse depth calving models produced very different patterns of crevasse penetration (Figs. 6.18, 6.19). The surface crevasse model, which predicts calving to occur when surface crevasses reach the waterline, produced a generally smooth crevasse depth field. However, the basal crevasse depth

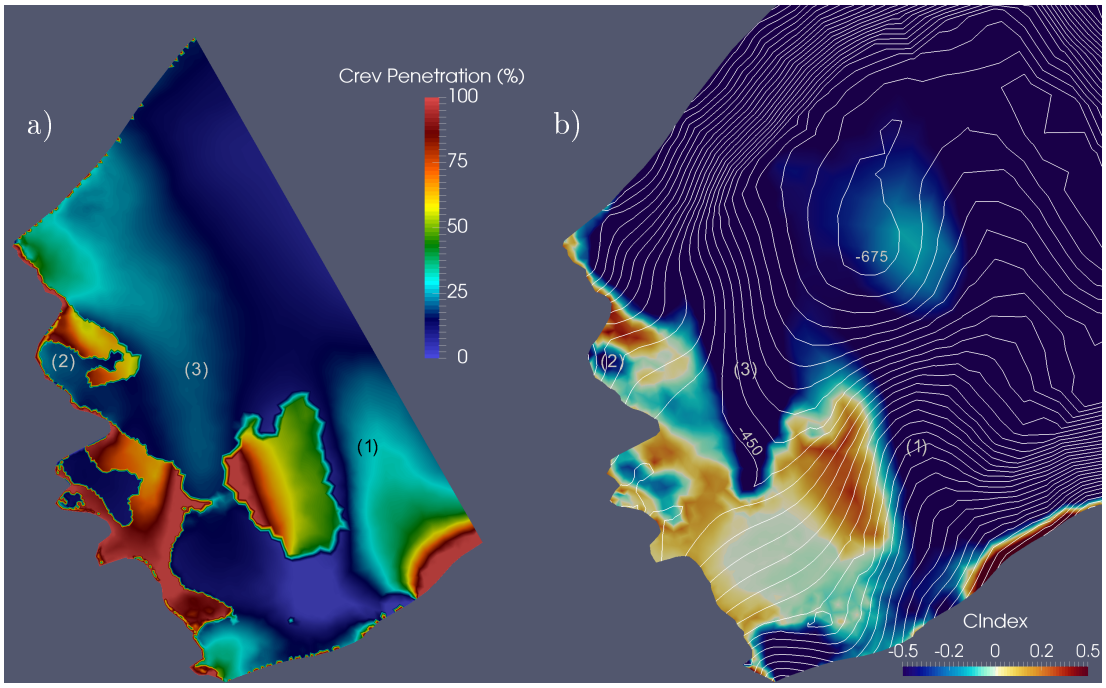

Figure 6.19: a) Crevasse penetration (%) for basal crevasse model, and b) the calving index (colour) and elevation (contours, 25m spacing) of the base of the ice. Basal topography exerts a significant influence on the penetration of basal crevasses. Point (1) is a large ridge which the ice flows over, suppressing basal crevasses in the stoss side and promoting them in the lee side. At point (2), a small pinning point influences crevasse depth. At point (3), the bed is flowing uphill from the local minimum of -675 m.a.s.l. towards the terminus, and the resulting compressive stress prevents crevasse opening.

model, which accounts for both surface and basal crevasses, displays a more complex pattern with sharp boundaries between almost no crevassing to deep crevasse fields over short distances. This section attempts to explain these differences by comparing the crevasse fields with underlying physical properties and processes.

Figure 6.18 compares the penetration of surface crevasses with the surface topography near the terminus. At the point marked (1), there is a large region of very *low* crevasse penetration at the surface, just downstream of the grounding line (indicated by the white line). This indicates that the near-surface stress regime in this region must be largely compressive, compared with the surrounding regions, causing crevasse penetration to be strongly suppressed.

Surface topography (Fig. 6.18b) indicates that the surface elevation drops steeply here, as the glacier becomes ungrounded. Just downstream of point (1) the surface elevation reaches a minimum before rising again towards the terminus.

This surface profile, in conjunction with the buoyant forces measured in this region (Fig. 6.2), is indicative of a buoyancy driven bending moment focused at the grounding line at point (1). The glacier is flowing steeply downhill as it becomes ungrounded, and Figure 6.2 indicates that the glacier becomes superbuoyant in this region (i.e. the ice here is below the level of neutral buoyancy). This is because the upstream ice and topography forces the glacier downward faster than it can adjust through creep. However, the floating ice further downstream permits a greater bending force with a pivot at the grounding line. This upward bending force results in compressive stress at the surface near the pivot, creating the large region of closed surface crevasses at point (1).

Crevasse penetration for the basal crevasse model (Fig. 6.19a) contrasts sharply with the surface crevasse model. Figure 6.19b shows the basal calving index (σ_{basal}) and elevation of the base of the glacier. The basal calving index (Eq. 5.25) combines the most extensional principal stress component (σ_1) and water pressure (P_w), and defines the stress available to open crevasses. Thus, crevasse penetration (Fig. 6.19a) measures the proportion of the thickness of the ice where $\sigma_{basal} > 0$. However, although the crevasse penetration percentage is a depth-integral, similarities in the patterns observed in Figs. 6.19a and 6.19b indicate that processes at the very base of the glacier largely control the upwards penetration of basal crevasses.

Patterns in the calving index at the base of the ice appear to be largely controlled by basal topography. The large spur at point (1) results in low calving index in the stoss side and high calving index in the lee side, and other topographic features result in similar patterns. Note, however, that the crevasse penetration to the south east of point (1) is in fact quite high; however, the similar pattern in the corresponding location in Figure 6.18a reveals that this crevasse penetration is largely driven by surface crevasses.

A minor pinning point at point (2) similarly results in low calving index at this point, and Fig. 6.19a indicates that this topographic feature creates a region of low crevasse penetration which interrupts a pattern which is otherwise quite similar to the surface crevasse penetration (Fig. 6.18a).

At point (3), the glacier is flowing uphill from the local minimum elevation at $-675\,\mathrm{m\,a\,s\,l}$, and this topographic feature also acts to close basal crevasses. Just beyond this feature, calving index at the base begins to increase and regions of high crevasse penetration begin to appear.

It is clear that basal crevasses are more acutely sensitive to changes in basal topography than surface crevasses. This is to be expected, basal topography exerts a strong control on the stress regime at the bed, and it is this stress regime which is directly responsible for the opening and closure of crevasses. The surface crevasse field, which is further removed from processes at the bed, varies more smoothly, though basal topography clearly still influences surface crevasses at wider spatial scales, as made evident by the bending moment at the grounding line.

6.3.3 Topography & Geometry

Basal topography clearly exerts a first order control on crevasse penetration in the model. Basal calving index, which defines the total stress available to open basal crevasses, tends to decrease in the stoss side and increase in the lee side of bedrock obstacles (Fig. 6.19). This is as expected: obstacles on the bed create compressional forces as ice flows over them (Benn and Evans, 2014), closing crevasses, while the subsequent loss of traction beyond the obstacle creates extension and opens crevasses.

The southern portion of Store's terminus flows over a bedrock spur at point (1) in Fig. 6.19. The upper ice surface (Fig. 6.18b) reveals the effect this spur has on ice thickness. The glacier appears to 'pile up' behind the spur before rapidly descending and thinning on the lee side, resulting in flotation. This flotation means that the southern side of the terminus lacks the strong topographic control on margin position, increasing the sensitivity of calving to external factors such as submarine melting.

In contrast, the northern side of the terminus is still flowing up over a reverse bed slope at the point where calving defines the front. The small bedrock bump at point (2) in Fig. 6.19, and a similar feature towards the middle of the terminus, collectively exert strong topographic control on calving rate. The compressive stress in the stoss side, and extensive stress in the lee side of these features makes calving almost inevitable here.

Further support for the idea of strong topographic control comes from the basal slip sensitivity simulations in Experiment 2 (Section 6.2.3). Increasing the velocity of the ice at the terminus by up to 20% did not affect the terminus position; instead, calving rate scaled with the velocity, and the terminus remained

stable. This strongly implies that calving tends to occur in certain *places* rather than at a given *rate* controlled by environmental factors. Of course, the reality is that both topographic control and environmental factors influence calving; the model's response to ice mélange and submarine melting (Section 6.1.3), as well as satellite observations of Store's seasonal evolution (Figs. 6.15, 6.16), confirm this.

The results highlight the important role basal topography and, more generally, glacier geometry play in controlling the calving regime. In the case of Store, this observation goes some way to explain the glacier's interannual stability during a period when many glaciers in Greenland experienced retreat (Seale et al., 2011). Furthermore, considering that in the model and observations (Section 6.3.1), Store Glacier appears to experience more seasonal range on the southern side of the terminus than the north, this can be explained in the context of basal topography.

Clearly, then, topography exerts a strong influence on Store Glacier's calving behaviour. Remote sensing studies (Carr et al., 2013; McFadden et al., 2011; Moon et al., 2015) suggest that the same may be true of other West Greenland calving glaciers. This suggests that establishing more accurate and precise basal topography should be a priority for the glaciological community. No calving model, however complex and however fine the resolution, would succeed in predicting the calving behaviour of Store Glacier without accurately representing the basal topography which defines the terminus position.

6.3.4 The Effect of Submarine Melt on Calving

I found that the effect of submarine melting on calving depended greatly on how the melt was applied (Section 6.1). In Experiment 1 Run 010, where *distributed* melting was the only forcing, the summer increase in melt rate was found to *reduce* calving rate (Fig. 6.8b), although the reduction in calving mass loss was less than the increase in mass loss from submarine melting, such that there was still a slight retreat in terminus position overall. This is a somewhat counter-intuitive result, which disagrees with previous studies on the subject (O'Leary and Christoffersen, 2013; Warren and Kirkbride, 2003), which suggest that undercutting by submarine melting should amplify calving. O'Leary and Christoffersen, (2013) proposed that undercutting by submarine melting should increase calving rate by promot-

ing extensional stresses at the surface above the undercut. As submarine melting progressively undermines the terminus ice cliff, the ice cliff becomes increasingly unstable and prone to calving by toppling. However, a 2D modelling study by Cook et al., (2014) found that undercutting by submarine melting had limited effect on the calving rate of Helheim Glacier, East Greenland, a result which agrees with the findings presented here. This apparent contradiction between studies is discussed in more detail below.

When concentrated submarine melting from conical plumes was also applied (Fig. 6.8c), the summer increase in melt rate *did* increase calving rate, and led to significant terminus retreat. Figures 6.4b and 6.4c illustrate this contrasting seasonal evolution of the terminus with and without concentrated melting from conical plumes. The direct contribution of conical plumes to mass loss from the terminus is almost negligible, so its ability to significantly impact calving rate is an interesting result, which is discussed in more detail below.

Distributed Melting

To explain the reduction in calving rate in response to distributed submarine melting along the calving margin, it is essential to consider Store Glacier's geometry, topographic setting and flow. The terminus of Store Glacier flows rapidly (6 km/a) over a large bedrock sill (Fig. 6.19b), though as discussed previously, it floats above this sill in the south. It also flows down through a narrowing fjord which becomes wider just beyond the terminus. Both the bedrock sill and the fjord constriction act to stabilise the terminus by increasing resistive stresses here, while the deepening and widening of the fjord beyond the terminus diminish these resistive stresses, promoting calving. These features most likely explain Store's stable terminus position over the past several decades while other glaciers in Uummannaq Fjord have undergone rapid and sustained retreat (Howat et al., 2010). Thus, Store Glacier is characterised by the rapid delivery of ice to a relatively stable terminus. This stable terminus position ensures that most of the ice remains intact until it reaches the lee side of the terminus sill, after which it calves off because the sea floor deepens and the sidewalls become further apart.

The proposed mechanism by which submarine melting promotes calving involves the enhancement of near-surface stresses by the progressive undercutting of the terminus (O'Leary and Christoffersen, 2013). However, in the case of Store,

there is a topographically well defined terminus position at which stresses quickly increase to the point of calving. Therefore, so long as ice is delivered to the terminus *more rapidly than it is melted*, there will be little, if any, enhancement of the calving rate, as the ice is bound to calve anyway. In fact, as the model suggests (Fig. 6.8b), the result of increased submarine melting is only to remove ice which would otherwise have calved, thus reducing calved volume.

Recall, however, that in fact, the total mass loss does increase slightly during the melt season, as the reduction in calving is less than the increase in distributed submarine melting (Section 6.1.5). This may be due to the fact that the terminus is less topographically constrained in the south than the north, where the ice is more firmly grounded. Therefore, in the south, the undercutting destabilisation proposed by O'Leary and Christoffersen, (2013) may indeed be occurring. Figure 6.4b lends some support to this hypothesis; the light blue (melt season) front position slightly upstream of the usual terminus position indicates melt induced retreat here.

Furthermore, although the summer increase in distributed submarine melting does not enhance calving, the results of Experiment 1 show that without *any* submarine melting, the modelled terminus advances far into the fjord (Run 000, Fig. 6.4a). Thus, while distributed submarine melting may have very little effect on the *seasonal* evolution of the front, it plays an important role in keeping the glacier from advancing beyond the bedrock sill on which it current terminates.

The model's sensitivity to increasing distributed submarine melting was tested in Experiment 2 (Section 6.2). Store's terminus was able to accommodate a 50% increase in distributed melt rate, but when melt rate was doubled from $3.1\,\mathrm{m\,d^{-1}}$ to $6.2\,\mathrm{m\,d^{-1}}$ in summer, and from $1.3\,\mathrm{m\,d^{-1}}$ to $2.6\,\mathrm{m\,d^{-1}}$ in winter, the result was a rapid retreat of the terminus by up to 1200 m in year 2. This retreat occurred predominantly in the southern region of the terminus (Fig. 6.9a), lending further support to the idea that topographic control limits the effect of submarine melting in the north more than in the south.

Concentrated Melting

Concentrated melting from conical plumes had a greater effect on calving and the shape of the terminus than distributed melting in Experiment 1, despite its very localised presence. The southern side of the terminus retreated significantly

further when concentrated submarine melting was imposed in summer (Fig. 6.4c). Furthermore, the region which underwent greater retreat is constrained on either side by the two imposed plumes, implying that the plumes are able to destabilise the region between them.

The results of Experiment 2 showed that a doubling of concentrated submarine melting from these two plumes led to an additional seasonal retreat of up to 1 km in the region between them, compared to the control run (Fig. 6.9b). Doubling distributed melting had a greater destabilising effect, as discussed above, but it should be noted that doubling the *concentrated* submarine melting from two narrow conical plumes is a significantly smaller environmental forcing than doubling the melt rate along the entire ice-ocean interface.

Concentrated submarine melting essentially forces a local retreat of the terminus where the plumes occur, regardless of calving rate. The resulting 'notches' cut into the terminus by this concentrated plume melting act to promote calving by destabilising the surrounding ice. Lateral drag from the fjord sidewalls, transmitted through the glacier by horizontal shear stress, is an important resistive component of the glacier's force balance, especially in regions where basal drag is low or absent (i.e. where the terminus is floating or almost floating). The incision of notches by concentrated submarine melting effectively isolates the surrounding ice from the resistive stress from the sidewalls, promoting longitudinal extension, crevasse growth and, thus, calving. This implies that the positioning of concentrated plumes may be critical in determining the shape and stability of the calving terminus.

It should also be noted that, although the results indicate that Store's terminus stability could be affected by a doubling of distributed melt rate, such an increase would require a significant perturbation to the local oceanographic and atmospheric climate. Previous modelling work (Xu et al., 2013) suggests that submarine melting by forced convection, such as occurs at Store and other Greenland outlet glaciers, is primarily controlled by the rate of freshwater flux into the fjord and the temperature of the proglacial water body. The results of Xu et al., (2013) suggest that, for high discharge regimes, such as would be required for high rates of submarine melting, the melt rate scales with $q^{0.54}$ and $TF^{1.17}$, where q and TF are the subglacial freshwater discharge and the temperature above pressure melting point, respectively. This implies that a doubling of the distributed submarine melt rate would require almost a doubling of TF, a

quadrupling of subglacial discharge, or some combination of the two. It is beyond the scope of this study to estimate how these parameters will change in a warming climate, but I hypothesise that a doubling of submarine melt rates in the 21st century is unlikely.

However, the model also underwent significant seasonal retreat in response to increased concentrated submarine melting from conical plumes. Thus, a *reorganisation* of the subglacial hydrological system to promote more concentrated melting at the expense of distributed melting could have a destabilising effect on the terminus without requiring a large change in total subglacial discharge. For example, if the subglacial hydrological system became more channelised near the terminus, this could promote more concentrated plumes along the terminus which could, in turn, increase calving and destabilise the ice front. Surface velocity records from Store Glacier (Fig. 6.17) (Ahlstrøm et al., 2013) show a distinctive late-summer slow down, similar to that which previous authors have attributed to a switch in the subglacial hydrological system from distributed to channelised drainage (Bartholomew et al., 2010; Sundal et al., 2011). Thus, if a warming climate were to exert an influence on the timing and characteristics of this switch, the resulting change in the subglacial hydrological system could redistribute subglacial discharge at the terminus to enhance concentrated plume melting at the expense of distributed melting. This represents a mechanism whereby changes in the *distribution* rather than the magnitude of subglacial discharge could severely affect the stability of Store's terminus.

6.3.5 Ice Mélange Buttressing

Ice mélange is the main driver of seasonal terminus position variability in the model (Section 6.1.3). In Experiment 1, mélange buttressing resulted in a mean advance of 500 m from winter to late spring. Experiment 2 revealed that halving the thickness of the mélange did not significantly alter the behaviour, suggesting that present day mélange thicknesses are more than sufficient to influence calving behaviour. It also implies that there is some upper limit on the ability of the mélange to affect the terminus position; once the mélange exerts sufficient buttressing to almost completely prevent calving, additional buttressing has no effect on terminus behaviour.

When mélange was completely removed in Experiment 2, the floating tongue

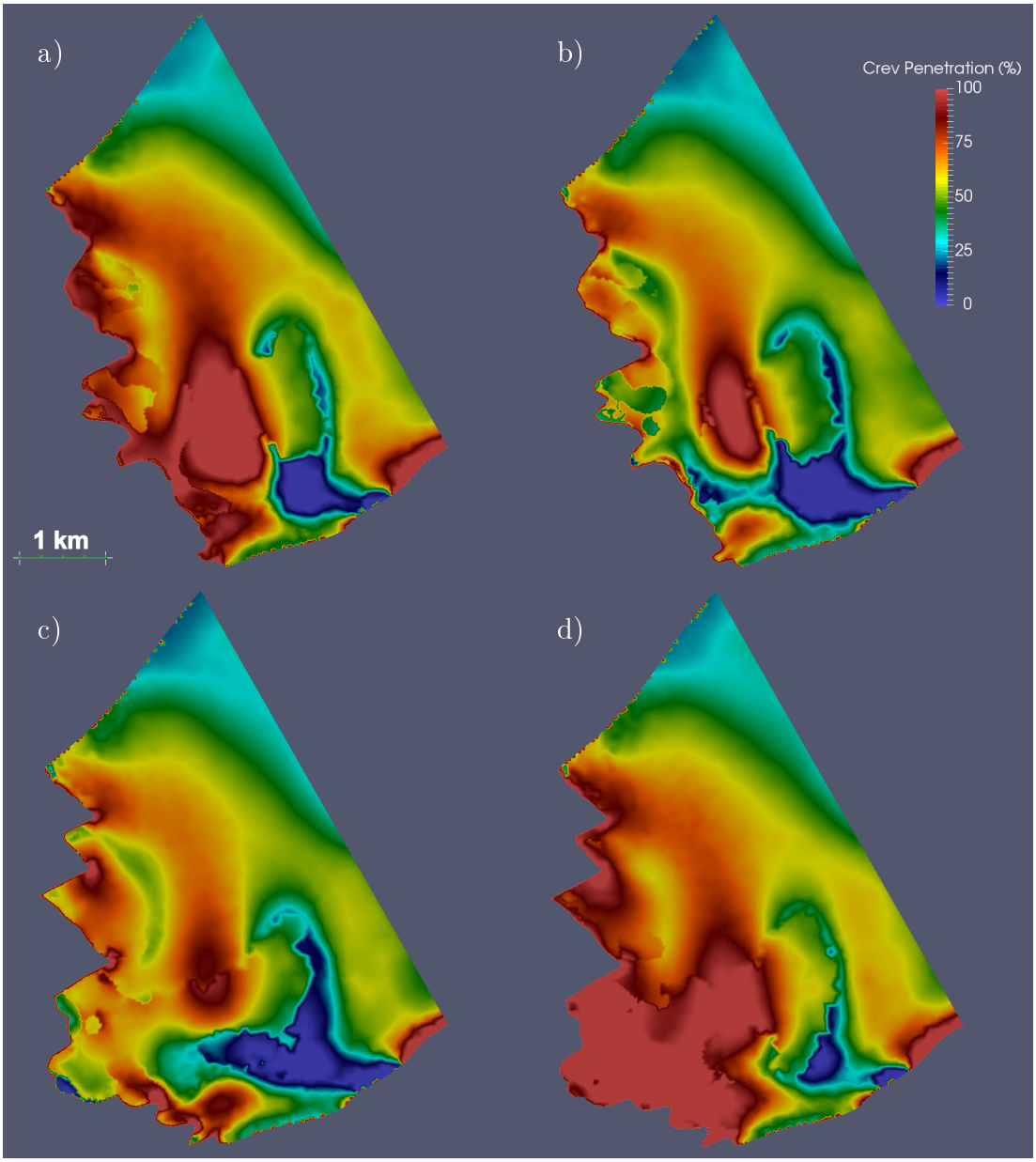

Figure 6.20: Crevasse penetration (%) a) before and b) after ice mélange formation, and c) before and d) after its collapse.

does not advance, as is to be expected. However, the model also underwent significantly greater retreat in summer compared to the control, with mean terminus position retreating 400 m further upstream than the control, despite no additional melt forcing being applied. This implies that the mélange has a role in stabilising the terminus which, importantly, extends *beyond* the period when it is present. In other words, mélange buttressing is not simply an instantaneous stabilising

force, but also promotes interannual stability. Potentially, the deceleration which accompanies the growth of the mélange allows the terminus to 'recharge' and gain stability, possibly by increasing glacier thickness in the region near the terminus, counteracting dynamic thinning in summer driven by reduced basal drag.

Reducing the length of the mélange season in Experiment 2 had some effect on the advance of the terminus in spring. When the mélange season was shortened by 1 month, the advance began later but the overall range in terminus position was unchanged, suggesting that some other process may be imposing an upper limit on spring advance. When the season length was reduced by 2 months, the spring advance was limited in a few years, suggesting that a significant shift in regional climate seasonality could alter the long term behaviour of the terminus. However, in neither case did the terminus undergo additional summer retreat, as described above, suggesting that even a short mélange season provides sufficient support to maintain the glacier's stable terminus position.

Interestingly, the mélange exerted significantly more influence on the south side of the glacier than the north. Figures 6.20a,b show the effect of the formation of ice mélange on crevasse penetration near the terminus, while Figures 6.20c,d illustrate the effect of its collapse in late spring.

The difference in terminus shape between Figs. 6.20a and 6.20c shows how the terminus evolves over the course of the mélange season, and highlights that the effect of the mélange is greatest in the southern part of the terminus, where the terminus reaches flotation and significant advance occurs. I hypothesise that this is due to the difference in buoyant forces across the front (Fig. 6.2), and this is explored further in Section 6.3.6 below.

Comparing model results to observations (Section 6.3.1) confirmed that ice mélange does indeed drive seasonal evolution of the terminus position, but the comparison also showed that the model exaggerates the effect of ice mélange somehow; both the seasonal advance of the terminus (Fig. 6.15) and the velocity time series (Fig. 6.17b) appeared overly sensitive to mélange buttressing. There are several potential reasons for this exaggerated effect. Firstly, for simplicity mélange buttressing is applied in a binary 'on/off' fashion, whereas in reality the mélange grows through the season, and does not form or collapse instantly as assumed here. Thus, applying 'full-strength' mélange from February to the end of May may be an overestimate.

It is also possible that the strength of the ice mélange is overestimated. Due

to the difficulty of studying the ice mélange directly, the strength was estimated by observing the change in glacier velocity before and after the collapse of the mélange. Force balance then allows the buttressing force to be estimated from this change in velocity. There are some implicit assumptions in this method which may not be valid, not least the assumption that the strength of the mélange just prior to collapse is representative of its rheology throughout the season. Additionally, the method assumes that mélange buttressing is the only component of the force balance which changes. If the mélange collapse is triggered by some other change, for example an increase in surface melting, then it is possible that this change also modified conditions at the base of the glacier, and thus the force balance. However, it is worth noting that two independent estimates of Store Glacier's ice mélange buttressing strength by Walter et al., (2012) and Toberg et al., (2016) produced similar values for the strength of the mélange, suggesting that this value is well founded.

Alternatively, it maybe that the estimated strength of the mélange is indeed representative, but that the buttressing force is not constant. Ice mélange is a granular mixture of icebergs and sea ice, and while it clearly has significant *compressional* strength in the direction of ice flow, due to the 'butting together' of large icebergs, it may be quite weak in the vertical direction. Therefore, large 'toe first' calving events may locally disperse the mélange, temporarily reducing or entirely removing the buttressing force. A previous study by Amundson et al., (2010) found that the flow of ice mélange at Jakobshavn Isbræ was significantly affected by calving. Between calving events, they found that the mélange moved forward at the same rate as the glacier, essentially being forced down the fjord by the advancing terminus. Calving events were found to trigger significant but transient acceleration of the mélange (up to $5 \times 10^4\,\mathrm{m\,d^{-1}}$ for around 10 minutes), suggesting significant disruption of the granular ice mélange. An ongoing investigation of Store's ice mélange by N. Toberg, from which the mélange strength estimates in this study were obtained, should be able to ascertain whether a similar process occurs at Store Glacier. If so, this would explain the observed discrepancy between model and observations.

6.3.6 Buoyant Forces

Terminus advance and retreat in the 3D model is significantly greater along the southern side of the terminus than the north (Fig. 6.4d). Furthermore, in Experiment 1 Run 011, conical plume melting causes the terminus to retreat beyond the otherwise stable position, again predominantly in the south. Overall, this suggests that calving processes in the south are more sensitive to external factors than in the north.

This difference in behaviour is due to the difference in buoyant forces: the south side is floating up to 2 km inland of the terminus, while the north remains largely grounded (Fig. 6.2). This means that any advance in the northern region requires a transition from grounded to floating ice. This transition promotes calving (Benn et al., 2007b), for two reasons. Firstly, the loss of basal traction over a relatively short distance will lead to significant longitudinal extension and, therefore, the formation of deeper crevasses. Secondly, because ice in the north is firmly grounded (Fig. 6.2), there is a significant upward bending as ice flows down over the bedrock sill into deeper water. In contrast, the southern side of the glacier is already floating for some distance before it reaches its stable terminus position. Thus, the loss of basal traction occurs *inland*, where the ice is well supported by the grounded ice on either side, stabilising this transition. Furthermore, the ice has had some distance to reach neutral buoyancy (Fig. 6.2), meaning that the buoyant forces at the terminus are diminished.

6.3.7 Model Limitations

The 3D calving model presented in this chapter has been shown to successfully capture seasonal dynamics of Store Glacier, which was the main aim of this study. However, the model has some limitations which should be addressed in future work. Firstly, due to the computational cost of solving the full-Stokes equations in 3D, the model simulations run for only 5 years; this is too short a time-frame to be able to confidently draw conclusions about the long term effect of the environmental forcings which were investigated. For example, the model terminus did not respond to a significant reduction in basal drag (Fig. 6.14), because of the stability afforded by the basal pinning point. However, in the long term, reduced basal drag would be expected to lead to dynamic thinning,

which is an important component of the feedback loops which relate long term stability of calving glaciers to environmental change. Related to this is the fact that basal slip is taken from inverse simulations (Section 5.7), and does not evolve in response to changing ice thickness. In reality, dynamic thinning will reduce effective pressure and, thus, basal drag; the inability of the current model setup to capture this effect limits the analysis herein to short term changes occurring at the terminus.

Several of the Experiment 2 sensitivity analyses (Section 6.2) showed rapid retreat of the southern side of the terminus, after which the model breaks down due to issues with the remeshing algorithm (Section 5.8.2). Therefore, it is not currently possible to say whether this initial retreat of the southern side would trigger further retreat of the terminus as a whole. This points to a need, in future work, to improve the robustness of the remeshing algorithm. Furthermore, the two points where the terminus reaches the valley sidewalls are fixed in the current implementation, which simplifies the remeshing algorithm. However, these fixed sidewall positions are partly responsible for the breakdown of the remeshing algorithm following retreat, and so this should be addressed in future work.

The remeshing algorithm currently also requires that the terminus remain projectable in some coordinate system, for purposes of interpolation. For the most part, the projectability requirement has little impact on the behaviour of the model. However, when the southern side of the terminus advances a floating tongue, the terminus shape exhibits perfectly straight lines at the sides of this tongue, which are obviously unphysical. This effect is most obvious in Figure 6.4a, the Experiment 1 no-forcing run. Only the southern margin of the floating tongue forms this unphysically straight edge; this is due to the direction of flow at the terminus, which is orientated more to the south than the shape of the terminus might suggest. Thus, in the rotated coordinate system in which projectability is imposed, the velocity field points slightly left of the z-axis. This leads to a tendency for the terminus to want to 'overlap' itself in this direction, as ice is not flowing directly outward from the terminus orientation. When the evolution of the terminus is computed by `FrontAdvance3D` (Section 5.6), the subroutine 'shaves off' this overlap to maintain projectability, resulting in the straight edge.

Generally, the limitations discussed above point to a need to improve the robustness of the remeshing algorithm (Section 5.8.2). In order for the model to represent longer term change, as well as a wider range of calving settings, such

as ice shelves, future work will aim to either improve the remeshing algorithm or replace it with a more sophisticated and robust alternative scheme. Many of the current issues revolve around the need for vertical extrusion of a 2D mesh, rather than a direct 3D meshing, due to the requirement for 'thin plate' elements. This requirement may be achievable through a more sophisticated direct 3D meshing scheme.

Aside from the robustness of the remeshing algorithm, the main challenge for future work is improving computational efficiency. Section 7.3 discusses the task of integrating calving models into full ice-sheet models, which typically solve lower-order approximations of the Stokes equations.

CHAPTER 7

Synthesis & Conclusions

This study has presented results from 2D and 3D calving models developed for the Elmer/Ice glacier modelling package, and tested on Store Glacier, West Greenland. This chapter compares and discusses the performance of these two models, discusses the wider goal of implementing calving criteria into large-scale ice sheet models, and highlights some priorities for future model development.

7.1 Model vs. Observations

Section 6.3.1 provides a comparison of the 3D model output with observed terminus evolution in 2014, obtained from TerraSAR-X data provided by A. Luckman. In terms of maximum and minimum terminus position, Experiment 1 Run 011 provided the best match to observations (Fig. 6.15a). This simulation included all submarine melt terms, but not ice mélange. Run 111, which did include ice mélange, overestimated the maximum extent of the terminus (Fig. 6.15b), but provided a better match to observed evolution of the terminus through time (Fig. 6.16).

Several conclusions can be drawn from the model's agreement (and disagreement) with observations. The good agreement, in terms of the onset of seasonal advance and retreat, between the full-forcing 3D model and the observations from 2014, confirm that ice mélange is indeed the principle driver of seasonal advance of Store's terminus. However, the model appears to overestimate the buttressing effect of ice mélange; the mean terminus position of the model advances around 500 m, whereas observations from 2014 suggest a total range of 300 m. Potential reasons for the exaggerated effect of ice mélange in the model were discussed in

Section 6.3.5.

In simulations without submarine melting, the southern side of the terminus immediately advanced far beyond the observed seasonal range, and remained in this advanced position throughout the simulation. This suggests that submarine melting is important in defining the current seasonal range; without melting, the terminus position would presumably be significantly further down the fjord.

7.2 2D vs. 3D Models

The 3D model (Chapter 5) which represents the primary outcome of this study is significantly more complex and computationally demanding than its 2D counterpart (Chapter 3). Therefore, use of the 3D model is only justified if its performance can be shown to be significantly better than 2D. This section compares the behaviour and fidelity of the two models, to determine if and when the complexity of the 3D model is justified.

7.2.1 Submarine Melting

The conclusions drawn from the 2D and 3D models differed significantly with regards to the importance of submarine melting. In 2D, the calving model showed little response to submarine melting of the terminus: melting alone had no effect at all on the terminus position, and in conjunction with ice mélange, the only effect was a brief 250 m retreat at the end of the mélange season. Sensitivity analysis suggested that even doubling maximum melt rate to $16\,\mathrm{m\,d^{-1}}$ would not destabilise the terminus.

In the 3D model, by contrast, submarine melting was responsible for preventing a sustained 800 m advance into the fjord. Concentrated submarine melting from two conical plumes was found to increase the seasonal range of the southern side of the terminus by 500 m. In the sensitivity analysis, doubling the distributed submarine melt rate led to a 900 m retreat of the mean terminus position, with the southern side of the terminus retreating more than 1 km, at which point the simulation broke down. The sensitivity analysis also showed that, despite their narrow range of effect, concentrated plumes are also capable of significantly destabilising the terminus, suggesting that a reorganisation of the subglacial drainage system near the terminus could significantly affect Store's long term stability.

This difference between the two models is most likely due to the inability of the 2D model to represent lateral variability in submarine melting. In 3D, a laterally homogeneous 'distributed melt' was overlain with concentrated melting from conical plumes at two locations on the terminus where these features are consistently observed at the surface in UAV imagery. This locally concentrated melt rate allows the conical plume to undermine the stability of the surrounding ice by creating embayments in the front, which isolates portions of the terminus from the lateral support provided by the surrounding ice. The 2D model cannot represent this effect and this is probably responsible for its insensitivity to melting.

7.2.2 Ice Mélange

The 2D and 3D models displayed very different patterns of seasonal front evolution in response to ice mélange. In 2014, Store Glacier's seasonal range in mean terminus position was around 300 m. In the 3D model, ice mélange results in a mean advance of 500 m. However, in the 2D model, the total advance in response to ice mélange was 1500 m, 5 times greater than reality. This clearly indicates that the floating tongue in the 2D model was *unrealistically stable*, which is further supported by the fact that the ice mélange in the 2D model leads to a complete cessation of calving, while in the 3D model, calving continues to occur during the mélange season, at a reduced rate.

In the 2D model, the terminus velocity was strongly inversely correlated with advance of the floating tongue (Fig. 4.2); as the front advanced, it decelerated, and vice versa. However, in the 3D model, there was no clear relationship between terminus position and velocity (Fig. 6.3); instead, the velocity appeared to be largely controlled by the seasonal change in basal slip and the buttressing effect of the mélange.

Overall, the floating tongue in the 2D model appears to be too stable: its length is significantly greater than observed, and the deceleration as it advances results in reduced stretching and a complete cessation of calving. This is due to the nature of the terminus evolution in 2D and 3D. In the 3D model, the terminus position at the northern and southern edge remains fixed. This is actually an enforced condition in the 3D model, but it agrees with observations. Thus, as the terminus advances, it does not encounter any additional lateral drag from the sidewalls, as the contact point between terminus and fjord remains fixed.

However, in the 2D model, the terminus implicitly advances as a perfectly straight line, meaning that the hypothetical northern and southern margin also advance and retreat in line with the central part of the terminus. Thus, as the 2D model advances a long, flat floating tongue, lateral drag is maintained, while driving stress diminishes due to the lack of surface slope.

7.2.3 Lateral Variability

The results of the 3D model indicate significantly different calving behaviour between the north and south sides of the glacier (Section 6.1.4). In the case of the 'full forcing' run, the largest icebergs on the south side ($1.28 \times 10^9\,\mathrm{m}^3$) were an order of magnitude larger than those on the north ($1.67 \times 10^8\,\mathrm{m}^3$), and while the northern side remained fairly fixed throughout the year, the southern side displayed a seasonal range of over 1.2 km. As discussed in Section 6.3.6, this difference in behaviour is due to the topographic setting and the resulting buoyant forces.

Furthermore, even without the effect of variable submarine melting (Section 7.2.1), differences in velocity across the terminus quickly result in a terminus which does not form a straight line from one side of the fjord to the other, instead displaying frequent headland and bay formations. These features will undoubtedly affect the stresses in the ice; a headland which advances into the fjord without lateral constraint from surrounding ice will be significantly less stable than ice which is effectively in contact with both valley sidewalls. The 2D model is, of course, completely unable to represent this lateral variability; as the terminus advances and retreats in 2D, it implicitly does so as a perfectly straight line from one side to the other, thus removing the possibility of such headland instabilities.

Finally, given the distinct behaviour of the north and south sides, it would be difficult, if not impossible, to choose a 'representative' 2D flowline which can capture the overall dynamics of the glacier. For example, the 2D model's domain is the central flowline, and the model displays features of the northern side of the terminus (insensitivity to melt rates) and the southern side (advance of the floating tongue). If, as the 3D model suggests, a climate-induced retreat of the terminus were to begin on the southern side, finally leading to overall collapse, the 2D model would likely be unable to capture this.

Recent remote sensing studies (Carr et al., 2013; McFadden et al., 2011; Moon et al., 2015) point to the importance of topography and geometry in modulating the response of West Greenland outlet glaciers to external environmental forcing. This underscores the necessity for accurate representation of glacier geometry, which is likely impossible in 2D.

7.2.4 Ice Temperature

Aside from the inherent inability of the 2D model to capture laterally variable processes, the 2D and 3D model setups are not identical. In the 2D model, I do not solve for ice temperature, instead assuming that the ice is a constant $-10\,^{\circ}\mathrm{C}$. This made the 2D model more computationally efficient, but more importantly, recent work indicates that heterogeneous temperature violates the underlying assumptions of 2D flowline models of glaciers with significant changes in width (Passalacqua et al., 2016), such as Store (Section 3.2).

In the 3D model, I solve for the temperature as part of the spin-up, and then maintain the computed temperature field throughout the calving simulations, for reasons of efficiency. The stress strain relationship of ice is highly dependent on the temperature, and this may account for the underprediction of stress in the 2D model. If this were the case, it would underline the importance of an accurate temperature field in calving models. Further, given the findings of Passalacqua et al., (2016), this would imply that 2D flowline calving models cannot be used to model outlet glaciers with significant lateral convergence, as such 2D models cannot permit variable temperature.

7.2.5 Model Tuning

An important consideration in comparing the performance of the 2D and 3D models is that, as described in Section 3.6, a tuning factor was applied to the calving criterion in the 2D model. This factor adjusted the predicted depth of crevasses by 7.5%; although this value is small, I found that without it, the 2D terminus was excessively stable, and would continue to advance into the fjord without limit. This tuning parameter is significant, given that the calving criterion is an otherwise physically based calving law. That is, aside from the tuning parameter, the calving criterion is an uncalibrated, unparameterised predictor based on a theo-

retical understanding of the relationship between crevasse formation and stress. Therefore, if one assumes that the underlying Nye crevasse criterion (Nye, 1957) is accurate, the need for the tuning parameter indicates that the 2D model *fails to properly account for the stress state at the terminus.* In contrast, the behaviour of the 3D model was found to be in good agreement with observations (Section 6.3.1), *without any applied tuning.* I conclude, therefore, that the near-terminus stress state of the 3D model is significantly more accurate than that of the 2D model.

Overall, the 3D model was found to perform significantly better than the 2D model for Store Glacier. The lack of tuning and better agreement with observations indicate that the 3D model is capturing physical processes occurring at Store's terminus which the 2D model failed to account for. I conclude that for glaciers with significant lateral variability in terms of geometry, topography and melt rates, 3D models should be employed. This raises the question of which glaciers can be reasonably simulated in 2 dimensions. There is no particular reason to assume that Store Glacier is unusual in its lateral heterogeneity, but data regarding calving front topography or lateral variability in terminus behaviour are sparse, making it difficult to generalise with confidence. In terms of submarine melting, studies on Petermann Glacier (Rignot and Steffen, 2008; Stewart et al., 2004) found that the floating tongue of Petermann Glacier has large melt channels on its underside, and significant lateral variability in submarine melt rate. Motyka et al., (2011) found a similarly variable submarine melt rate under Jakobshavn Isbræ's floating tongue. More generally, it seems likely that any glacier whose subglacial hydrological system is channelised will display laterally heterogeneous melt rates (Slater et al., 2015), and thus would not be suitable for modelling in 2D.

7.3 Calving in Ice-Sheet Models

The 3D calving model developed in this study successfully reproduces the observed seasonal evolution of Store Glacier's calving terminus. The fidelity of the model can be attributed to several factors: the ability of the crevasse depth calving criterion to capture the first-order controls on calving rate; the full-Stokes treatment of ice flow, which permits localised stresses to be resolved; the inclusion

of the third dimension, which allows lateral and vertical gradients to be properly represented; the variable mesh resolution, which makes it feasible to work with element sizes of the order of 100 m at the terminus; and the remeshing scheme which allows the model domain to precisely follow the evolution of the calving front. However, the 5-year simulations presented in Chapter 6 took around 1 week to run, distributed across 24 CPUs. While it certainly possible to reduce this time by increasing the number of processors, some aspects of the model are not currently parallelised, which limits the model's scalability such that to run the model for a full ice sheet for hundreds of years is infeasible at present. Therefore, achieving the long-term goal of predicting sea level contributions from the Greenland and Antarctic Ice Sheets will require that the calving model is incorporated into large-scale and more efficient ice sheet models.

Two different approaches to this problem could be pursued: either the findings of the 3D full-Stokes calving model could be parameterised somehow, such that they could be incorporated into lower-order models, or the full-Stokes equations must somehow be incorporated into full ice-sheet, long term models. The relative benefits and limitations of these two approaches are discussed below.

Modern ice-sheet models typically solve either SIA, SSA, hybrid combinations of these or, for example, L1L2 or first-order approximations, due to their computational efficiency compared with 3D full-Stokes (Hindmarsh, 2004). However, this computational efficiency comes at the cost of accurately representing the full stress field of the glacier. Scaling analysis shows that, for modelling the flow in the interior of large ice masses, the cost in terms of accuracy is generally significantly less than the gains made in efficiency (Hindmarsh, 2004). However, boundary effects in the region near the calving front (Hindmarsh, 2012) mean that even the first-order multi-layer model of Blatter, (1995) neglects terms which may be significant.

Fortunately, neglecting important stress terms does not mean that a reasonable representation of calving processes could not be incorporated into such a model. Just as subgrid plume dynamics have been successfully parameterised into larger scale fjord circulation models (Cowton et al., 2015), so too could near-terminus stress effects be parameterised into lower-order and lower resolution ice sheet models. If the nature of the calving front boundary layer effect is sufficiently simple to be analytically predictable from the geometry of the terminus, the depth of the proglacial water body, and other environmental parameters, then

a parameterised calving model could be implemented as a separate subroutine into a large-scale ice sheet model. For example, the ice cliff force imbalance (Section 2.2.3) cannot be properly represented by depth-integrated models, but its effect on the stress regime behind the ice-ocean interface has receive sufficient attention (Hanson and Hooke, 2000; Hanson and Hooke, 2003; O'Leary and Christoffersen, 2013) that it may be possible to draw generalised conclusions about its effect on stress near the terminus, and include this into a calving parameterisation.

However, while it may be possible to predict and account for the missing stress effects in lower order models, it is difficult to see how the interaction of the stress field and the complex, evolving geometry of calving fronts could be accounted for. This study has shown, through a comparison of a 2D and 3D calving model, the importance of small scale geometry in predicting calving. Headlands and embayments of the order of a few hundred metres significantly affect the stress regime and calving rate. Calving rate and stress, in turn, control the development of these geometric features of the terminus. Incorporating this level of detail into ice sheet models is hindered by their low resolution and/or typically inflexible discretisation schemes.

The alternative to attempting to parameterise calving into lower-order models is to incorporate full-Stokes, flexible discretisation and evolving calving fronts into ice sheet models. The main obstacle to overcome in this approach is computational efficiency. Gillet-Chaulet et al., (2012) resolved the flow of the entire Greenland Ice Sheet via full-Stokes using Elmer/Ice, demonstrating one of the key advantages of FEM, namely flexible discretisation. Their model operated on a mesh whose horizontal resolution varied from 40 km in the interior to 1 km at the fast flowing margins. However, their results presented a single snapshot of Greenland's velocity field; a long-term time-evolving model presents a significantly greater computational expense.

A recent study by Ahlkrona et al., (2016) presented a mixed model capable of solving the SIA and the full-Stokes equations in different parts of the same model domain. So far, the model is limited to a simple synthetic geometry, but the concept is a powerful one; it presents the possibility of incorporating full-Stokes into an ice-sheet model *only where needed*. Thus, the computational efficiency of lower-order approximation is largely retained, but the stress field can be accurately represented near the calving termini. Additional challenges remain, such as the complex boundary conditions required to represent the evolution of

a large number of outlet glaciers, and the computationally demanding remeshing of the entire ice sheet domain. However, given the significant challenges of the parameterisation approach discussed previously, this approach seems like the most promising.

7.4 Summary

This study has developed 2D and 3D calving models for outlet glaciers, tested against a dataset from Store Glacier. The model implements the crevasse depth calving criterion (Benn et al., 2007a,b; Nick et al., 2010), which uses the modelled stress regime to compute the penetration of surface and basal crevasses, and thereby predict calving. A remeshing scheme was developed to allow the 3D model geometry to evolve through time 'unsupervised', and the model was forced with realistic present-day submarine melt rates and ice mélange buttressing.

The 3D model successfully captures the seasonal evolution and calving dynamics of Store Glacier, *without calibration*, suggesting that the calving model is capable of capturing the physical processes responsible for calving. This represents a significant step towards predicting the long-term evolution of calving outlet glaciers in response to climate change, one of the greatest remaining uncertainties currently faced by the climate modelling community.

A wide range of calving behaviours arose as emergent properties from the model, from frequent, laminar events associated with ice cliff toppling and undercutting, to the massive tabular bergs associated with the annual collapse of the ice mélange. This demonstrates the comprehensive scope of the crevasse depth criterion; rather than attempting to link an overall 'calving rate' to environmental factors, the model realistically captures the shape and size of individual calving events in response to changes in the stress regime.

The ability of the model to capture individual calving events allowed the underlying physical processes to be examined in detail. One of the main outcomes of this analysis was the importance of glacier geometry, topography and buoyant forces. I found a significant difference in calving behaviour between the southern and northern regions of the terminus. The northern side, which is well grounded on a large pinning point, remained relatively fixed in position, and typically calved via small, laminar events, associated with the sudden loss of basal resistance on

the lee side of the pinning point. On the southern side, the terminus reached flotation, largely due to the upstream bedrock spur which diverts and thins the ice flowing over it. Flotation profoundly affected calving behaviour; icebergs produced here were wider and longer (i.e. 'more tabular'), and the terminus position showed much greater seasonal variability, due to the lack of strong topographic control. Significant bending forces arose near the grounding line here, due to the local hydrostatic imbalance associated with the transition from grounded to floating ice, and this bending moment greatly affected the crevasse field.

I was able to reproduce the observed seasonal evolution of Store Glacier by forcing the model with submarine melting and ice mélange buttressing alone. Previous studies have suggested that hydrofracturing from water in surface crevasses is an important control on calving rate (Cook et al., 2012; Nick et al., 2010). I opted not to investigate this process, due to the inability to estimate crevasse water depth. Although the possibility of a hydrofracturing effect at Store cannot be ruled out, the good agreement between the model results and observations suggest that it is not necessary to invoke this process to explain seasonal advance and retreat of the terminus.

The results of this study highlight the role of ice mélange in forcing the observed seasonal advance and retreat of the calving terminus, and suggests that the mélange season may allow the glacier terminus to 'recharge', helping to prevent retreat in response to increased submarine melting in summer. The importance of submarine melt *distribution* was emphasised by the model's increased seasonal range in response to concentrated melting from conical plumes. Sensitivity analysis suggests that either a complete loss of winter ice mélange, or a doubling of distributed *or* concentrated melt rates could drive retreat of the terminus which, over longer timescales, could destabilise the current terminus position entirely. The importance of subglacial topography, highlighted by this model, as well as previous studies (Benn et al., 2007b; Brown et al., 1982; Vieli et al., 2001), suggests that, were Store to retreat from its current pinning point into the deep trough upstream, this retreat may continue for up to 30 km. This is supported by the findings of a recent study by Morlighem et al., (2016) which investigated the potential effects of increased submarine melting on Store.

The performance of the 3D model was found to be significantly better than the 2D model (Section 7.2). I found that the 2D model required tuning in order to generate calving behaviour which corresponded to observations, while the 3D

model did not. I propose that calving is fundamentally a 3D process and that lateral variability in geometry and environmental processes are significant in controlling calving behaviour. It is suggested, therefore, that 3D models for calving should be preferred over 1D or 2D flowline models.

The crevasse depth model is physically-based and uncalibrated, so the ability of the 3D model to reproduce the seasonal evolution of Store Glacier in response to realistic present-day environmental forcing is a major step forward in terms of understanding the calving process and its links to climate. Future work will attempt to generalise the calving and remeshing algorithms in order to make them more broadly applicable, and investigate approaches to incorporating the calving criterion into large scale ice sheet models.

Appendix

A.1 2D Calving Criterion

The 2D calving criterion, as presented in Chapter 3 and the publication associated with the 2D model (Todd and Christoffersen, 2014), is:

$$\sigma_{net} = 2\tau_E \mathrm{sgn}(\tau_{xx}) - \rho_i g d + P_w \tag{1}$$

This can be restated to show that the 2D calving criterion compares the largest principal deviatoric with the rate of creep closure due to ice overburden:

$$\sigma_{net} = 2|\boldsymbol{\tau_1}| \mathrm{sgn}(\tau_{xx}) - \rho_i g d + P_w \tag{2}$$

To demonstrate that these are equivalent, the definition of effective deviatoric stress is (Cuffey and Paterson, 2010):

$$\tau_E^2 \equiv \frac{1}{2}\left(\tau_{xx}^2 + \tau_{yy}^2 + \tau_{zz}^2\right) + \tau_{xy}^2 + \tau_{yz}^2 + \tau_{zx}^2 \tag{3}$$

However, in 2D, this reduces to the only non-zero terms:

$$\tau_E^2 \equiv \frac{1}{2}\left(\tau_{xx}^2 + \tau_{yy}^2\right) + \tau_{xy}^2 \tag{4}$$

Considering that the quantity τ_E is an *invariant* of the deviatoric stress tensor, its value must remain unchanged in any coordinate system. Thus, in the coordinate system aligned with the eigenvectors of $\boldsymbol{\tau}$ (i.e. the principal stress directions), the shear term disappears, and so:

$$\tau_E^2 \equiv \frac{1}{2}\left(|\boldsymbol{\tau_1}|^2 + |\boldsymbol{\tau_2}|^2\right) \tag{5}$$

Furthermore, due to the symmetry of the 2D deviatoric stress tensor, $|\boldsymbol{\tau_1}| = |\boldsymbol{\tau_2}|$, and so:

$$\tau_E = |\boldsymbol{\tau_1}| \tag{6}$$

A.2 Basal Topography from Mass Conservation

Basal topography is an important and yet often poorly constrained prerequisite for accurate modelling of glacier dynamics. Radar survey is able to accurately constrain glacier thickness and bed elevation, but such radar surveys are sparse in nature; there is no constraint on bed topography between radar flight lines. While interpolation methods such as kriging have previously been employed to estimate the large regions between flight lines (Bamber et al., 2001), their capability is limited. In this study, I use a mass conservation technique similar to that presented by (Morlighem et al., 2011) to better constrain basal topography.

Mass conservation takes advantage of the incompressibility of ice to determine changes in glacier geometry from observed surface velocity. Incompressibility implies that for any given region in the glacier, the flow into and out of the region must be equal. Mathematically, this implies that the divergence of the velocity field is zero:

$$\nabla \cdot \boldsymbol{u} = 0 \tag{7}$$

where $\boldsymbol{u}$ is the velocity vector.

Surface velocity fields from satellite or airborne survey measure displacement in the horizontal plane, and from this horizontal velocity field, a 2D 'apparent' divergence can be computed. Combining the apparent divergence of the horizontal velocity field with Eq. 7 allows the missing *vertical* component of the divergence to be ascertained. This vertical divergence component represents changes in the thickness of the ice column as it flows through the domain, which is otherwise unknown. This is analogous to the observation that rivers flow more slowly through deeper sections of their channel, and accelerate through shallow sections.

This mass conservation technique is used to infer basal topography from IceBridge radar flight lines and satellite surface velocity, using the open-source GIS software QGIS. I begin with a single IceBridge flight line which provides pre-

cise glacier thickness and bed elevation along a profile which laterally transects Store's catchment, essentially defining a flux gate. From this flux gate, I use QGIS to compute flowlines in the surface velocity field. Each pair of adjacent flowlines defines a hypothetical 'flow tube', and changes in the width of these flow tubes must be balanced by changes in the flow tube's thickness and any mass loss through surface and basal accumulation and melting. Thus, by accounting for surface mass balance from RACMO 2.3 data (Noël et al., 2015), and assuming that basal mass balance is negligible compared to other components, I compute changes in flow tube thickness in the direction of flow, allowing basal topography downstream of the radar flight line to be constrained. Of course, it would also be possible to carry out this computation in the upstream direction, but for the reasons outlined below, I only attempt to constrain the basal topography in the region between the radar flight line and the terminus.

This technique has two main underlying assumptions. Firstly, it makes the assumption that ice is indeed incompressible. Changes in the bulk density of ice are small outside the firn compaction zone which composes the upper part of the ice column in the accumulation area, but an additional source of apparent divergence comes from the opening and closure of crevasses. Therefore, I assume that changes in crevasse depth occur sufficiently slowly so as to have only a negligible effect on the assumption of incompressibility.

Secondly, the technique assumes that there are no changes in the vertical velocity profile along the length of each flow tube. Over the entire length of the domain, from the upstream inflow boundary to the terminus, this assumption is unlikely to be valid. However, in the fast flowing region near the terminus where basal slip is low and basal velocity high, this assumption is probably reasonable. So long as most of the velocity comprises basal slip as opposed to internal deformation, changes in vertical velocity profile should be negligible.

The validity of the assumptions made above are difficult to test directly. Fortunately, independent verification of the method as a whole is provided by bathymetric data from just beyond Store's terminus. This data, obtained and kindly provided by A. Hubbard and N. Chauché, should match the mass conservation dataset at the terminus. I found that this was indeed the case for most of the terminus, but at the northern and southern edges, there was a significant discrepancy (Fig. 1). Therefore, in order to make best use of the available data, the bathmetric data was smoothed into the mass conservation product. At the

upstream and lateral limits of the region where mass conservation is applied, I smooth the mass conservation product into a wider, lower resolution bed DEM product produced by S. Palmer by kriging interpolation between IceBridge flight lines.

The reason for the poor performance of the mass conservation method near the lateral margins at the terminus may be that lateral shear stresses from the valley sidewalls invalidate the assumption of only negligible changes in vertical velocity profile. By contrast, the interior of Store's fast flowing trunk is less susceptible to these lateral stresses, and here the mass conservation method seems to perform well.

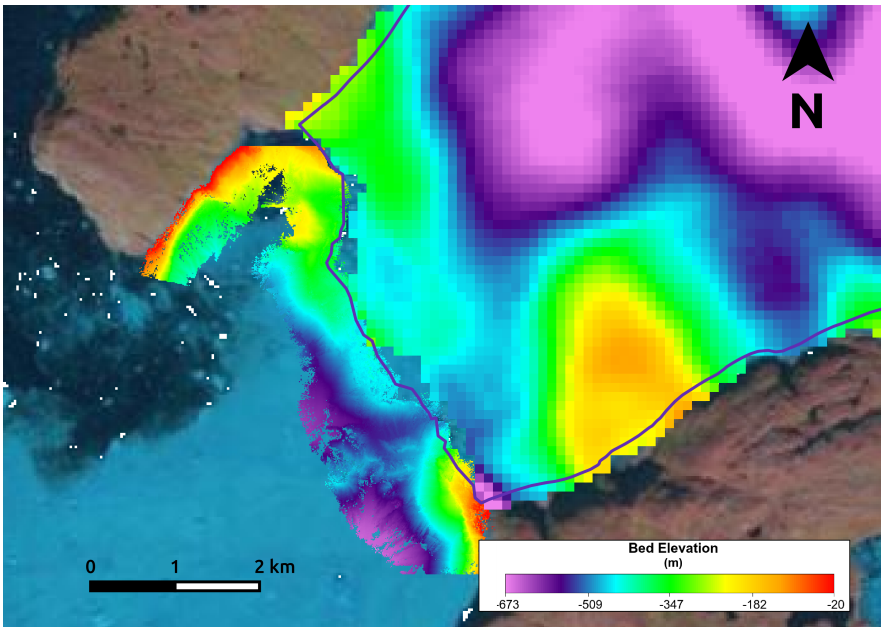

Figure 1: Comparison of basal topography from mass conservation and bathymetric data from marine survey. The blue line represents the terminus position. The lower resolution data to the north-east of the terminus is mass conservation derived, while the high resolution data to the south west is bathymetric data.

Bibliography

Ahlkrona, J., P. Lötstedt, N. Kirchner and T. Zwinger (2016). Dynamically coupling the non-linear Stokes equations with the shallow ice approximation in glaciology: Description and first applications of the ISCAL method. *Journal of Computational Physics* 308, 1–19. arXiv: 1503.07743.

Ahlstrøm, A. P., S. B. Andersen, M. L. Andersen, H Machguth, F. M. Nick, I Joughin, C. H. Reijmer, R. S. W. Van De Wal, J. P. Merryman Boncori, J. E. Box, M Citterio, D Van As, R. S. Fausto and A Hubbard (2013). Seasonal velocities of eight major marine-terminating outlet glaciers of the Greenland ice sheet from continuous in situ GPS instruments. *Earth Syst. Sci. Data* 5, 277–287.

Alley, R. B., H. J. Horgan, I. Joughin, K. M. Cuffey, T. K. Dupont, B. R. Parizek, S. Anandakrishnan and J. Bassis (2008). A Simple Law for Ice-Shelf Calving. *Science* 322, 1344–1344.

Amundson, J. M., M. Fahnestock, M. Truffer, J. Brown, M. P. Lüthi and R. J. Motyka (2010). Ice mélange dynamics and implications for terminus stability, Jakobshavn Isbræ, Greenland. *Journal of Geophysical Research* 115, F01005.

Arthern, R. J. and G. H. Gudmundsson (2010). Initialization of ice-sheet forecasts viewed as an inverse Robin problem. *Journal of Glaciology* 56, 527–533.

Bamber, J. L., R. L. Layberry and S. P. Gogineni (2001). A new ice thickness and bed data set for the Greenland ice sheet: 1. Measurement, data reduction, and errors. *Journal of Geophysical Research* 106, 33773–33780.

Bamber, J. L., M. J. Siegert, J. A. Griggs, S. J. Marshall and G. Spada (2013). Paleofluvial Mega-Canyon Beneath the Central Greenland Ice Sheet. *Science* 341, 997–999.

Bartholomew, I., P. Nienow, D. Mair, A. Hubbard, M. A. King and A. Sole (2010). Seasonal evolution of subglacial drainage and acceleration in a Greenland outlet glacier. *Nature Geoscience* 3, 408–411.

Bassis, J. N., H. A. Fricker, R. Coleman and J. B. Minster (2008). An investigation into the forces that drive ice-shelf rift propagation on the amery ice shelf, East Antarctica. *Journal of Glaciology* 54, 17–27.

Benn, D. and D. J. A. Evans (2014). *Glaciers and Glaciation*. Routledge.

Benn, D. I., N. R. J. Hulton and R. H. Mottram (2007a). 'Calving laws','sliding laws' and the stability of tidewater glaciers. *Annals of Glaciology* 46, 123–130.

Benn, D. I., C. R. Warren and R. H. Mottram (2007b). Calving processes and the dynamics of calving glaciers. *Earth-Science Reviews* 82, 143–179.

Blatter, H. (1995). Velocity and stress fields in grounded glaciers: a simple algorithm for including deviatoric stress gradients. *Journal of Glaciology* 41, 333–344.

Boyce, E. S., R. J. Motyka and M. Truffer (2007). Flotation and retreat of a lake-calving terminus, Mendenhall Glacier, southeast Alaska, USA. *Journal of Glaciology* 53, 211–224.

Brown, C. S., M. F. Meier, A Post and G. Survey (1982). *Calving speed of Alaska tidewater glaciers, with application to Columbia Glacier*. US Dept. of the Interior, Geological Survey.

Carr, J. R., A. Vieli and C. Stokes (2013). Influence of sea ice decline, atmospheric warming, and glacier width on marine-terminating outlet glacier behavior in northwest Greenland at seasonal to interannual timescales. *Journal of Geophysical Research: Earth Surface* 118, 1210–1226.

Chauché, N. (2016). Glacier-Ocean interaction at Store Glacier (West Greenland). PhD thesis. Aberystwyth University.

Chauché, N., A. Hubbard, J.-C. Gascard, J. E. Box, R. Bates, M. Koppes, A. Sole, P. Christoffersen and H. Patton (2014). Ice–ocean interaction and calving front morphology at two west Greenland tidewater outlet glaciers. *The Cryosphere* 8, 1457–1468.

Christoffersen, P., J. A. Piotrowski and N. K. Larsen (2005). Basal processes beneath an Arctic glacier and their geomorphic imprint after a surge, Elisebreen, Svalbard. *Quaternary Research* 64, 125–137.

Christoffersen, P., M. O'Leary, J. H. Van Angelen and M. Van Den Broeke (2012). Partitioning effects from ocean and atmosphere on the calving stability of Kangerdlugssuaq Glacier, East Greenland. *Annals of Glaciology* 53, 249–256.

Cook, S., T. Zwinger, I. Rutt, S. O'Neel and T. Murray (2012). Testing the effect of water in crevasses on a physically based calving model. *Annals of Glaciology* 53, 90–96.

Cook, S., I. C. Rutt, T. Murray, A. Luckman, T. Zwinger, N. Selmes, A. Goldsack and T. D. James (2014). Modelling environmental influences on calving at Helheim Glacier in eastern Greenland. English. *The Cryosphere* 8, 827–841.

Cowton, T., D. Slater, A. Sole, D. Goldberg and P. Nienow (2015). Modeling the impact of glacial runoff on fjord circulation and submarine melt rate using a new subgrid-scale parameterization for glacial plumes. *Journal of Geophysical Research: Oceans* 120, 796–812.

Cuffey, K. and W. Paterson (2010). *The physics of glaciers*. 4th. Academic Press.

Depoorter, M. A., J. L. Bamber, J. A. Griggs, J. T. M. Lenaerts, S. R. M. Ligtenberg, M. R. van den Broeke and G. Moholdt (2013). Calving fluxes and basal melt rates of Antarctic ice shelves. *Nature* 502, 89–92.

Enderlin, E. M., I. M. Howat, S. Jeong, M.-J. Noh, J. H. van Angelen and M. R. van den Broeke (2014). An Improved Mass Budget for the Greenland Ice Sheet. *Geophysical Research Letters* 41, 866–872.

Favier, L, G Durand, S. L. Cornford, G. H. Gudmundsson, O Gagliardini, F. Gillet-Chaulet, T Zwinger, A. J. Payne and a. M. Le Brocq (2014). Retreat of Pine Island Glacier controlled by marine ice-sheet instability. *Nature Climate Change* 5, 117–121.

Gagliardini, O., G. Durand, T. Zwinger, R. C. A. Hindmarsh and E. Le Meur (2010). Coupling of ice-shelf melting and buttressing is a key process in ice-sheets dynamics. *Geophysical Research Letters* 37, L14501.

Gagliardini, O., T. Zwinger, F. Gillet-Chaulet, G. Durand, L. Favier, B. de Fleurian, R. Greve, M. Malinen, C. Martín, P. Råback, J. Ruokolainen, M. Sacchettini, M. Schäfer, H. Seddik and J. Thies (2013). Capabilities and performance of Elmer/Ice, a new-generation ice sheet model. English. *Geoscientific Model Development* 6, 1299–1318.

Gillet-Chaulet, F., O. Gagliardini, H. Seddik, M. Nodet, G. Durand, C. Ritz, T. Zwinger, R. Greve and D. G. Vaughan (2012). Greenland ice sheet contribution to sea-level rise from a new-generation ice-sheet model. English. *The Cryosphere* 6, 1561–1576.

Gladstone, R. M., V. Lee, J. Rougier, A. J. Payne, H. Hellmer, A. Le Brocq, A. Shepherd, T. L. Edwards, J. Gregory and S. L. Cornford (2012). Calibrated

prediction of Pine Island Glacier retreat during the 21st and 22nd centuries with a coupled flowline model. *Earth and Planetary Science Letters* 333-334, 191–199.

Greve, R. (2005). Relation of measured basal temperatures and the spatial distribution of the geothermal heat flux for the Greenland ice sheet. *Annals of Glaciology* 42, 424–432.

Gudmundsson, G. H., J. Krug, G. Durand, L. Favier and O. Gagliardini (2012). The stability of grounding lines on retrograde slopes. *Cryosphere* 6, 1497–1505.

Gudmundsson, G. H. (2003). Transmission of basal variability to a glacier surface. *Journal of Geophysical Research* 108, 1–19.

Hall, D. K., J. C. Comiso, N. E. Digirolamo, C. A. Shuman, J. R. Key and L. S. Koenig (2012). A Satellite-Derived Climate-Quality Data Record of the Clear-Sky Surface Temperature of the Greenland Ice Sheet. *Journal of Climate* 25, 4785–4798.

Hanson, B. and R. L. Hooke (2000). Glacier calving: A numerical model of forces in the calving-speed/water-depth relation. *Journal of Glaciology* 46, 188–196.

Hanson, B. and R. L. Hooke (2003). Buckling rate and overhang development at a calving face. *Journal of Glaciology* 49, 577–586.

Haresign, E. C. (2004). Glacio-limnological interactions at lake-calving glaciers. en. PhD thesis. University of St Andrews.

Harper, J. T., J. H. Bradford, N. F. Humphrey and T. W. Meierbachtol (2010). Vertical extension of the subglacial drainage system into basal crevasses. *Nature* 467, 579–582.

Hindmarsh, R. C. A. (2004). A numerical comparison of approximations to the Stokes equations used in ice sheet and glacier modeling. *Journal of Geophysical Research* 109, 1012.

Hindmarsh, R. C. A. (2012). An observationally validated theory of viscous flow dynamics at the ice-shelf calving front. *Journal of Glaciology* 58, 375–387.

Hock, R. (2003). Temperature index melt modelling in mountain areas. *Journal of Hydrology* 282, 104–115.

Holland, D. M., R. H. Thomas, B. de Young, M. H. Ribergaard and B. Lyberth (2008). Acceleration of Jakobshavn Isbræ triggered by warm subsurface ocean waters. *Nature Geoscience* 1, 659–664.

Howat, I. M., J. E. Box, Y Ahn, A Herrington and E. M. McFadden (2010). Seasonal variability in the dynamics of marine-terminating outlet glaciers in Greenland. *Journal of Glaciology* 56, 601–613.

Hutter, K. (1983). *Theoretical glaciology: material science of ice and the mechanics of glaciers and ice sheets*. Springer.

Intergovernmental Panel on Climate Change (2014). *Impacts, Adaptations, and Vulnerability*. Tech. rep. arXiv: `arXiv:1011.1669v3`.

James, T. D., T. Murray, N. Selmes, K. Scharrer and M. O'Leary (2014). Buoyant flexure and basal crevassing in dynamic mass loss at Helheim Glacier. *Nature Geoscience* 7, 593–596.

Jenkins, A. (2011). Convection-Driven Melting near the Grounding Lines of Ice Shelves and Tidewater Glaciers. *Journal of Physical Oceanography* 41, 2279–2294.

Jezek, K. C., C. R. Bentley and J. W. Clough (1979). Electromagnetic sounding of bottom crevasses on the Ross Ice Shelf, Antarctica. *Journal of Glaciology* 24, 321–330.

Johnson, C (1987). *Numerical solution of partial differential equations by the finite element method*. Courier Corporation.

Joughin, I., B. Smith, I. Howat and T. Scambos (2011). *MEaSUREs Greenland Ice Velocity: Selected Glacier Site Velocity Maps from InSAR. Boulder, Colorado, USA: NASA DAAC at the National Snow and Ice Data Center*.

Joughin, I, B. Smith, D. Shean and D Floricioiu (2014). Brief Communication: Further summer speedup of Jakobshavn Isbræ. *The Cryosphere* 8, 209–214.

Joughin, I., I. M. Howat, M. Fahnestock, B. Smith, W. Krabill, R. B. Alley, H. Stern and M. Truffer (2008). Continued evolution of Jakobshavn Isbrae following its rapid speedup. *Journal of Geophysical Research* 113, F04006.

Khan, S. A., J Wahr, M Bevis, I Velicogna and E Kendrick (2010). Spread of ice mass loss into northwest Greenland observed by GRACE and GPS. *Geophysical Research Letters* 37, L06501.

Lenderink, G., B. J. J. M. van den Hurk, E. van Meijgaard, A. van Ulden and H. Cuijpers (2003). *Simulation of present-day climate in RACMO2: first results and model developments*. Koninklijk Nederlands Meteorologisch Instituut.

Luckman, A and T Murray (2005). Seasonal variation in velocity before retreat of Jakobshavn Isbræ, Greenland. *Geophysical Research Letters* 32, L022519.

MacAyeal, D. R., E. A. Okal, R. C. Aster, J. N. Bassis, K. M. Brunt, L. M. Cathles, R. Drucker, H. A. Flicker, Y. J. Kim, S. Martin, M. H. Okal, O. V. Sergienko, M. P. Sponsler and J. E. Thom (2006). Transoceanic wave propagation links iceberg calving margins of Antarctica with storms in tropics and Northern Hemisphere. *Geophysical Research Letters* 33, L027235.

MacAyeal, D. (1993). A tutorial on the use of control methods in ice-sheet modeling. *Journal of Glaciology* 39, 91–98.

McFadden, E. M., I. M. Howat, I. Joughin, B. E. Smith and Y. Ahn (2011). Changes in the dynamics of marine terminating outlet glaciers in west Greenland (2000–2009). *Journal of Geophysical Research* 116, F02022.

McGranahan, G, D Balk and B Anderson (2007). The rising tide: assessing the risks of climate change and human settlements in low elevation coastal zones. *Environment and Urbanization* 19, 17–37.

Moon, T., I. Joughin and B. Smith (2015). Seasonal to multiyear variability of glacier surface velocity, terminus position, and sea ice/ice mélange in northwest Greenland. *Journal of Geophysical Research: Earth Surface* 120, 818–833.

Morland, L. W. (1987). Unconfined ice-shelf flow. *Dynamics of the West Antarctic Ice Sheet*, 99–116.

Morlighem, M., E. Rignot, H. Seroussi, E. Larour, H. Ben Dhia and D. Aubry (2010). Spatial patterns of basal drag inferred using control methods from a full-Stokes and simpler models for Pine Island Glacier, West Antarctica. *Geophysical Research Letters* 37, L14502.

Morlighem, M., E. Rignot, H. Seroussi, E. Larour, H. Ben Dhia and D. Aubry (2011). A mass conservation approach for mapping glacier ice thickness. *Geophysical Research Letters* 38, L19503.

Morlighem, M, E Rignot, J Mouginot, H Seroussi and E Larour (2014). Deeply incised submarine glacial valleys beneath the Greenland ice sheet. *Nature Geoscience* 7, 18–22.

Morlighem, M., J. Bondzio, H. Seroussi, E. Rignot, E. Larour, A. Humbert and S. Rebuffi (2016). Modeling of Store Gletscher's calving dynamics, West Greenland, in response to ocean thermal forcing. *Geophysical Research Letters* 43, 2659–2666.

Motyka, R. J. (1997). Deep-water calving at Le Conte Glacier, Southeast Alaska. *Calving glaciers: report of a workshop*, 115–118.

Motyka, R. J., M. Truffer, M. Fahnestock, J. Mortensen, S. Rysgaard and I. Howat (2011). Submarine melting of the 1985 Jakobshavn Isbrae floating tongue and the triggering of the current retreat. *Journal of Geophysical Research: Earth Surface* 116, F01007.

Nick, F. M., A Vieli, I. M. Howat and I Joughin (2009). Large-scale changes in Greenland outlet glacier dynamics triggered at the terminus. *Nature Geoscience* 2, 110–114.

Nick, F. M., C. J. Van der Veen, A Vieli and D. I. Benn (2010). A physically based calving model applied to marine outlet glaciers and implications for the glacier dynamics. *Journal of Glaciology* 56, 781–794.

Noël, B., W. J. van de Berg, E. van Meijgaard, P. Kuipers Munneke, R. S. W. van de Wal and M. R. van den Broeke (2015). Evaluation of the updated regional climate model RACMO2.3: summer snowfall impact on the Greenland Ice Sheet. English. *The Cryosphere* 9, 1831–1844.

Nye, J. F. (1957). The Distribution of Stress and Velocity in Glaciers and Ice-Sheets. *Proceedings of the Royal Society A: Mathematical, Physical and Engineering Sciences* 239, 113–133.

O'Leary, M. and P. Christoffersen (2013). Calving on tidewater glaciers amplified by submarine frontal melting. English. *The Cryosphere* 7, 119–128.

O'Leary, M. (2011). Frontal Processes on Tidewater Glaciers. PhD thesis. University of Cambridge.

Otero, J., F. J. Navarro, C. Martin, M. L. Cuadrado and M. I. Corcuera (2010). A three-dimensional calving model: numerical experiments on Johnsons Glacier, Livingston Island, Antarctica. *Journal of Glaciology* 56, 200–214.

Paasche, Ø. and E. W. N. Støren (2014). How does climate impact floods? Closing the knowledge gap. *Eos* 95, 253–254.

Passalacqua, O., O. Gagliardini, F. Parrenin, J. Todd, F. Gillet-Chaulet and C. Ritz (2016). Performance and applicability of a 2.5-D ice-flow model in the vicinity of a dome. *Geoscience Model Development* 9, 2301–2313.

Price, S. F., A. J. Payne, I. M. Howat and B. E. Smith (2011). Committed sea-level rise for the next century from Greenland ice sheet dynamics during the past decade. *Proceedings of the National Academy of Sciences of the United States of America* 108, 8978–8983.

Reeh, N. (1968). On the calving of ice from floating glaciers. *Journal of Glaciology* 7, 215–232.

Reeh, N., E. L. Christensen, C. Mayer and O. B. Olesen (2003). Tidal bending of glaciers: A linear viscoelastic approach. *Annals of Glaciology* 37, 83–89.

Rignot, E and P Kanagaratnam (2006). Changes in the velocity structure of the Greenland Ice Sheet. *Science* 311, 986–990.

Rignot, E. and K. Steffen (2008). Channelized bottom melting and stability of floating ice shelves. *Geophysical Research Letters* 35, L02503.

Rignot, E, M Koppes and I Velicogna (2010). Rapid submarine melting of the calving faces of West Greenland glaciers. *Nature Geoscience* 3, 187–191.

Rignot, E., Y. Xu, D. Menemenlis, J. Mouginot, B. Scheuchl, X. Li, M. Morlighem, H. Seroussi, M. van den Broeke, I. Fenty, C. Cai, L. An and B. de Fleurian (2016). Modeling of ocean-induced ice melt rates of five west Greenland glaciers over the past two decades. *Geophysical Research Letters* 43, 6374–6382.

Ryan, J. C., A. L. Hubbard, J. E. Box, J Todd, P Christoffersen, J. R. Carr, T. O. Holt and N Snooke (2015). UAV photogrammetry and structure from motion to assess calving dynamics at Store Glacier, a large outlet draining the Greenland ice sheet. *The Cryosphere* 9, 1–11.

Sassolas, C., T. Pfeffer and B. Amadei (1996). Stress interaction between multiple crevasses in glacier ice. *Cold Regions Science and Technology* 24, 107–116.

Scambos, T, C Hulbe and M Fahnestock (2003). Climate-induced ice shelf disintegration in the Antarctic Peninsula. *Antarctic Research Series* 79, 79–92.

Scambos, T. A., J. A. Bohlander, C. A. Shuman and P. Skvarca (2004). Glacier acceleration and thinning after ice shelf collapse in the Larsen B embayment, Antarctica. *Geophysical Research Letters* 31, L18402.

Scambos, T., H. A. Fricker, C.-C. Liu, J. Bohlander, J. Fastook, A. Sargent, R. Massom and A.-M. Wu (2009). Ice shelf disintegration by plate bending and hydro-fracture: Satellite observations and model results of the 2008 Wilkins ice shelf break-ups. *Earth and Planetary Science Letters* 280, 51–60.

Schoof, C (2007). Ice sheet grounding line dynamics: Steady states, stability, and hysteresis. *J. Geophys. Res* 112, F03S28.

Seale, A., P. Christoffersen, R. I. Mugford and M. O'Leary (2011). Ocean forcing of the Greenland Ice Sheet: Calving fronts and patterns of retreat identified by automatic satellite monitoring of eastern outlet glaciers. *Journal of Geophysical Research* 116, F03013.

Seddik, H., R. Greve, T. Zwinger, F. Gillet-Chaulet and O. Gagliardini (2012). Simulations of the Greenland ice sheet 100 years into the future with the full Stokes model Elmer/Ice. *Journal of Glaciology* 58, 427–440.

Slater, D. A., P. W. Nienow, T. R. Cowton, D. N. Goldberg and A. J. Sole (2015). Effect of near-terminus subglacial hydrology on tidewater glacier submarine melt rates. *Geophysical Research Letters* 42, 2861–2868.

Sohn, H.-G., K. C. Jezek and C. J. Van der Veen (1998). Jakobshavn Glacier, west Greenland: 30 years of spaceborne observations. *Geophysical Research Letters* 25, 2699–2702.

Stewart, C., E. Rignot, K. Steffen, N. Cullen and R. Huff (2004). *Basal topography and thinning rates of Petermann Gletscher, northern Greenland, measured by ground- based phase-sensitive radar.* Tech. rep. FRISP report no 15.

Straneo, F., G. S. Hamilton, D. A. Sutherland, L. A. Stearns, F. Davidson, M. O. Hammill, G. B. Stenson and A. Rosing-Asvid (2010). Rapid circulation of warm subtropical waters in a major glacial fjord in East Greenland. *Nature Geoscience* 3, 182–186.

Straneo, F., R. G. Curry, D. A. Sutherland, G. S. Hamilton, C. Cenedese, K. Våge and L. A. Stearns (2011). Impact of fjord dynamics and glacial runoff on the circulation near Helheim Glacier. *Nature Geoscience* 4, 322–327.

Straneo, F., D. A. Sutherland, D. Holland, C. Gladish, G. S. Hamilton, H. L. Johnson, E. Rignot, Y. Xu and M. Koppes (2012). Characteristics of ocean waters reaching greenland's glaciers. *Annals of Glaciology* 53, 202–210.

Sundal, A. V., A. Shepherd, P. Nienow, E. Hanna, S. Palmer and P. Huybrechts (2011). Melt-induced speed-up of Greenland ice sheet offset by efficient subglacial drainage. *Nature* 469, 521–524.

Sutherland, D. A. and F. Straneo (2012). Estimating ocean heat transports and submarine melt rates in sermilik fjord, greenland, using lowered acoustic doppler current profiler (LADCP) velocity profiles. *Annals of Glaciology* 53, 50–58.

Swithinbank, C (1977). Glaciological research in the Antarctic Peninsula. *Philosophical Transactions of the Royal Society of London. Series B, Biological Sciences A Discussion on Scientific Research in Antarctica Phil. Trans. R. Soc. Lond. B* 279, 161–183.

Thomas, R., E. Frederick, W. Krabill, S. Manizade and C. Martin (2009). Recent changes on greenland outlet glaciers. *Journal of Glaciology* 55, 147–162.

Toberg, N., J. Ryan, P. Christoffersen, N. Snooke, J. Todd and A. Hubbard (2016). Estimating ice-melange properties with repeat UAV surveys over Store Glacier, West Greenland. *EGU General Assembly 2016, held 17-22 April, 2016 in Vienna Austria*, 16354.

Todd, J. and P. Christoffersen (2014). Are seasonal calving dynamics forced by buttressing from ice mélange or undercutting by melting? Outcomes from full-Stokes simulations of Store Glacier, West Greenland. English. *The Cryosphere* 8, 2353–2365.

Turner, J. S. (1973). *Buoyancy effects in fluids*. Cambridge University Press., London.

Van der Veen, C. J. (1998a). Fracture mechanics approach to penetration of bottom crevasses on glaciers. *Cold regions science and technology* 27, 213–223.

Van der Veen, C. J. (1998b). Fracture mechanics approach to penetration of surface crevasses on glaciers. *Cold Regions Science and Technology* 27, 31–47.

Van der Veen, C. J. (1996). Tidewater calving. *Journal of Glaciology* 42, 375–385.

Vaughan, D. and R Arthern (2007). Why is it hard to predict the future of ice sheets? *Science* 315, 1503–1504.

Vieli, A and F. Nick (2011). Understanding and modelling rapid dynamic changes of tidewater outlet glaciers: issues and implications. *Surveys in geophysics* 32, 437–458.

Vieli, A., M. Funk and H. Blatter (2001). Flow dynamics of tidewater glaciers: A numerical modelling approach. *Journal of Glaciology* 47, 595–606.

Vieli, A., J. Jania and L. Kolondra (2002). The retreat of a tidewater glacier: Observations and model calculations on Hansbreen, Spitsbergen. *Journal of Glaciology* 48, 592–600.

Walter, J. I., E Jason, S Tulaczyk, E. E. Brodsky, I. M. Howat, A. H. N. Yushin and A Brown (2012). Oceanic mechanical forcing of a marine-terminating Greenland glacier. *Annals of Glaciology* 53, 181–192.

Warren, C., D. Benn, V. Winchester and S. Harrison (2001). Buoyancy-driven lacustrine calving, Glaciar Nef, Chilean Patagonia. *Journal of Glaciology* 47, 135–146.

Warren, C. R., N. F. Glasser, S. Harrison, V. Winchester, A. R. Kerr and A. Rivera (1995). Characteristics of Tide-Water Calving at Glaciar San-Rafael, Chile. *Journal of Glaciology* 41, 273–289.

Warren, C. R. (1991). Terminal environment, topographic control and fluctuations of West Greenalnd glaciers. *Boreas* 20, 1–15.

Warren, C. R. and M. P. Kirkbride (2003). Calving speed and climatic sensitivity of New Zealand lake-calving glaciers. *Annals of Glaciology* 36, 173–178.

Weidick, A and O Bennike (2007). Quaternary glaciation history and glaciology of Jakobshavn Isbræ and the Disko Bugt region, West Greenland: a review. *Geological Survey of Denmark and Greenland* 14.

Weidick, A, R. Williams and J. Ferrigno (1995). *Satellite Image Atlas of Glaciers of the World: Greenland*. USGS.

Xu, Y., E. Rignot, D. Menemenlis and M. Koppes (2012). Numerical experiments on subaqueous melting of Greenland tidewater glaciers in response to ocean warming and enhanced subglacial discharge. *Annals of Glaciology* 53, 229–234.

Xu, Y., E. Rignot, I. Fenty, D. Menemenlis and M. M. Flexas (2013). Subaqueous melting of Store Glacier, west Greenland from three-dimensional, high-resolution numerical modeling and ocean observations. *Geophysical Research Letters* 40, 4648–4653.

Zwally, H. J., W. Abdalati, T. Herring, K. Larson, J. Saba and K. Steffen (2002). Surface melt-induced acceleration of Greenland ice-sheet flow. *Science* 297, 218–22.